UNIVERSITY OF CALIFORNIA SAN DIEGO

Robot locomotion in granular environments via passive compliance and underactuation

A dissertation submitted in partial satisfaction of the
requirements for the degree
Doctor of Philosophy

in

Engineering Sciences (Mechanical Engineering)

by

Shivam Chopra

Committee in charge:

        Professor Nick Gravish, Chair
        Professor Falko Kuester
        Professor Tania Morimoto
        Professor Michael T Tolley
        Professor Michael Yip

2022

The dissertation of Shivam Chopra is approved, and it is acceptable in quality and form for publication on microfilm and electronically.

University of California San Diego

2022

I would like to dedicate this dissertation to my family,

for constant support and love through these years.

TABLE OF CONTENTS

LIST OF FIGURES

Everyday (from where turtle inspired digging idea came), for always being ready to do hand calculations and simulations even when you were busy, for all the meals we cooked and shared, and for all the deep conversations we had. Thank you for being there for me day and night and being always ready to help. To Dylan, for being a great mentor, friend, surf instructor, and for all the teachings and feedback I got from you. Thank you Ishida for always being ready to have meals together and for your support during the past few years.

To my family, my Mumma and Papa for always believing in me and letting me do this. It was very hard to be away from family for all these years but you always encouraged me to keep pushing. To my brother, Raghav, thank you for being one call away and always ready to learn what was going on with my life. Thank you for supporting my decision to pursue a doctorate and look we did it together!

Thank you Abhijith, for being the perfect roommate and the best supporting friend anyone can ever hope for. Thank you for always encouraging me to cook and have fun even when we had a bad day at work. Thank you Nirjhar, Priyank, Nitin, and Chetan for all the good times and for being always ready to hang out. To Rose, thank you for being there and supporting me through these last few years. To Rahaf, thank you for being a great friend and for all the insightful discussions.

If you're reading this and I haven't named you, thank you. If we have met, my life has been better with it and if we have yet to meet, I am excited.

Chapter 3, in part, has been published and presented in Adaptive Motion of Animals and Machines, 2021. Chopra, Shivam; Jadhav, Saurabh; Tolley, Michael T.; Gravish, Nick, AMAM 2021. The dissertation author was the primary investigator and author of this paper.

Chapter 4, in part, is currently being prepared for submission for publication of the material. Chopra, Shivam; Drago Vasile; Jadhav, Saurabh; Tolley, Michael T.; Gravish, Nick. The dissertation author will be the primary investigator and author of this paper.

Chapter 5, in part, is currently being prepared for submission for publication of the material. Chopra, Shivam; Drago Vasile; Jadhav, Saurabh; Tolley, Michael T.; Gravish, Nick. The dissertation author will be the primary investigator and author of this paper.

2016	B. E. in Mechanical Engineering *summa cum laude*, Punjab Engineering College, Chandigarh, India
2018	M. S. in Engineering Sciences (Mechanical Engineering), University of California San Diego
2022	Ph. D. in Engineering Sciences (Mechanical Engineering), University of California San Diego

PUBLICATIONS

Chopra S. and Gravish N. (2019) *Piezoelectric actuators with on-board sensing for micro-robotic applications*, Smart Materials and Structures. IOP Publishing, 28(11), p. 115036.

Chopra S., Tolley M. T., and Gravish N. (2020) *Granular jamming feet enable improved foot-ground interactions for robot mobility on the deformable ground.* IEEE Robotics and Automation Letters, 5(3), 3975-3981.

Chopra S., Vasile D., Jadhav S., Tolley M. T. and Gravish N.(2021) *Optimal design of underactuated appendages enable sensing and swimming in granular environments*. 2021 (In Review).

Drotman D., Chopra S., Gravish N. and Tolley M. T. (2021) *Bioinspired Soft Digging Robot*, IEEE RoboSoft 2022.

Jadhav S., Chopra S., Gravish N., and Tolley M. T. *Terrain-Structure Interaction- A multi-physics simulation framework for studying the response of soft body interaction with granular media.* (In Preparation)

ABSTRACT OF THE DISSERTATION

Robot locomotion in granular environments via passive compliance and underactuation

by

Shivam Chopra

Doctor of Philosophy in Engineering Sciences (Mechanical Engineering)

University of California San Diego, 2022

Professor Nick Gravish, Chair

Robots have shown prowess in demonstrating navigation in many extreme environments, except in granular media (GM), which remains relatively unexplored. GM such as sand, dry snow, and gravel are some of the most common substrates on Earth as well as other terrestrial planets, yet GM is one of the most challenging environments to traverse. Robots have to overcome large depth-dependent forces to navigate through granular media. Furthermore in GM, robots experience non-zero yield stress that may cause unpredictable fluid/solid resistance forces, all with extremely limited capabilities for sensing. This thesis addresses the problems of navigating GM by designing bioinspired, underactuated, and passively compliant robot limbs.

Depending on the external forces and local stresses, GM can exist as a solid and can flow

like a liquid, causing robots moving on GM to sink and slip. Thus, robot locomotion on GM poses high demands on foot placement and joint control. Taking inspiration from passive compliance in camel hooves, I designed a robot foot for improved locomotion on GM. The foot changed shape passively when in contact with the ground to reduce sinking, and actively changed stiffness for the ability to apply sufficient propulsion forces, which led to improved locomotion parameters. For locomotion within GM, I proposed a novel autonomous, untethered robot that swims with underactuated appendages, which enable both large propulsion forces through limb motion and obstacle sensing over a wide range around the robot. To optimize the design of appendages, I experimentally identified the optimum morphological and actuation parameters for generating thrust. I also investigated how the presence of an obstacle buried in GM influenced the granular flow around a moving appendage, enabling the ability to sense obstacles in grains. The results from sensing and propulsion experiments were integrated into an untethered robot capable of subsurface locomotion with a speed of ≈ 1.2 mm/s at a depth of 127 mm. Obstacle detection was demonstrated through experiments with embedded force sensors on the appendages of the robot. Overall, this thesis sheds light on how passively deforming and underactuated structures can enable movement on and within GM with minimal limb control while still enabling sensing capabilities.

Chapter 1

Introduction

Numerous robots have been successful in demonstrating locomotion on land, through the air, and in water. However, one substrate which remains relatively unexplored is granular media. GM exists as one of the most common substrates in nature in the form of sand, soil, dry snow, and extraterrestrial regolith. Recently, the study of robots capable of burrowing and moving on GM has been of growing interest due to their wide range of potential applications in search and rescue operations, mining, studying biological organisms, monitoring the seabed, underground and extraterrestrial exploration, ground resiliency, and contaminant monitoring [1].

1.1 Granular media

Granular media (GM) are a collection of discrete solid macroscopic particles that interact primarily through dissipative frictional forces [2]. GM is one of the most common substrates on Earth as well as other extraterrestrial planets. It occurs in the form of desert sand, soil, gravel, dry snow, etc. Although the interactions between granular particles are relatively simple, the physics of GM and predicting the stresses and flow response of GM is quite complex [3, 4]. Constituent particles in a GM can be spherical, oblong, rod-like, or many other shapes which can change the properties of the granular medium as a whole. [5]. When granular materials are either fully dry

Designing to minimize sink and slip	Designing to counter high resistive forces	Creating navigation opportunities
1. Soft foot with stiffness and shape control improves locomotion on GM	**2. Underactuated appendages enable robot locomotion in GM**	**3. Haptic detection of obstacles by measuring the differential grain resistance**
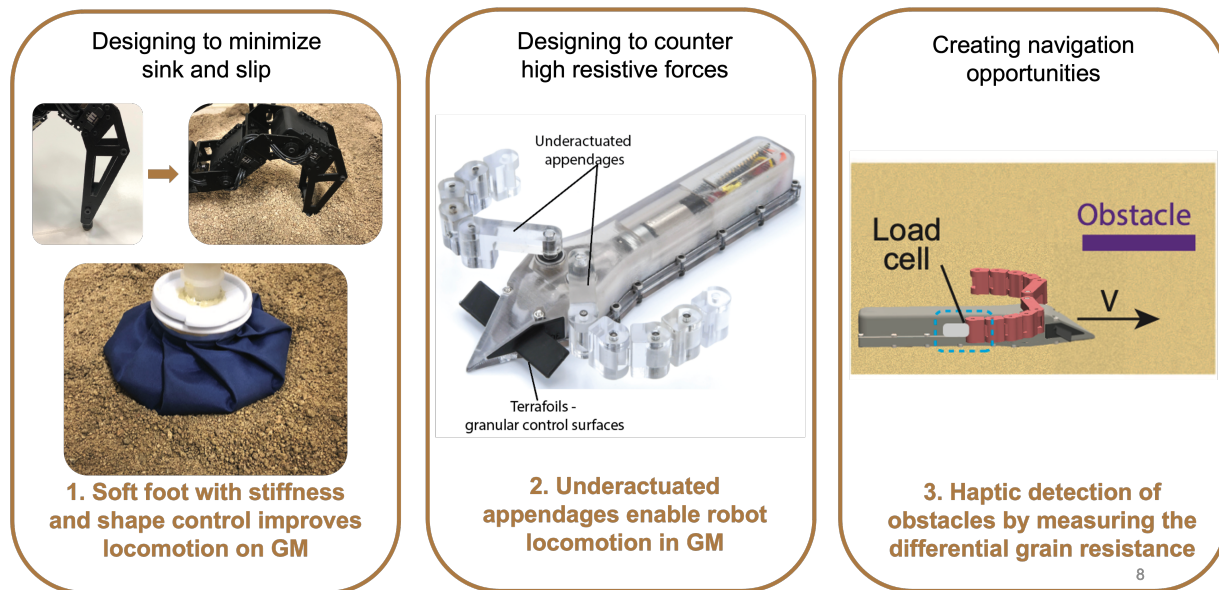
Figure 1.1: **Thesis overview.** In this thesis I addressed the three major challenges for locomotion in granular media a) sinking and slipping for robots navigating on GM, b) high resistive forces and unpredictable fluid-solid interaction c) no navigation capabilities because of opaque and damping nature of GM

or fully submerged in a fluid, many of the physical forces they experience are similar and studies of the physics of slow flows in dry granular material can be extended to the submerged case [6].

Since the physical interactions between granular particles are dominated by friction, the granular materials have been described as a "frictional fluid". Granular materials exhibit non-zero yield stress. Loading below this stress results in a stable, solid-like response of the granular material while loading above this yield stress results in a failure and flow of the granular material [7, 8]. Thus, granular material can exist in a solid-like state in which stationary particles support chains of force that propagate through the granular material. When forces are applied to the granular material that overcomes the yield condition the GM can exist in a fluid-like state in which the material flows and resettles. The yielding of granular material is necessary for digging and penetration of objects into the grains [9, 7]. The frictional nature of granular materials means that intruders dragged through granular material experience a force that does not depend on velocity [10]. In addition to a drag resistance, objects moving within granular material also experience a

2

lift force which depends on the shape of the intruder. Both drag and lift forces depend linearly on the depth and the projected cross-section of the intruder [5].

1.2   Modeling granular-intruder interaction

Unlike swimming locomotion where the interaction of a body and the surrounding fluid is governed by the Navier-Stokes equation, there aren't analytical models for locomotion in granular media. While working with the Navier-Stokes equations in the context of a soft, undulating, swimming robot is not a simple matter, many experimental and computational approaches have been developed (Fig.1.2). On the contrary, there is no single closed-form equation that can be used to describe the behavior of sand and soil in the study of robot locomotion. Instead, progress has been made through the development of empirical force laws for interaction between robots and GM through the development of resistive force theory (RFT) [5].

An intuitive approach to simulate granular media is by using the Discrete Element Method (DEM) where each particle is represented as a separate grain, and the collision interactions between the grains are solved in an explicit dynamic simulation [11]. However, the discrete element method can be computationally intensive and is not easily scalable to simulate particles on a large scale (e.g., millions of particles). An alternative approach is to average the physical response for the bulk of particles, thus representing granular media as a homogeneous continuum [12]. Continuum models for granular media have been widely used in soil mechanics using either finite element or finite volume methods. Continuum models are scalable to represent a large number of grains since they are represented as bulk material instead of individual grains. However, obtaining the homogeneous response for the bulk grains requires specialized material testing equipment such as a triaxial testing machine. Additionally, continuum modeling is limited in its applicability due to the built-in assumptions and is not suitable for simulating large deformations in granular media as encountered in the case of a robot swimming in granular material [13].

3

However, both discrete and continuum approaches focus heavily on the modeling of the flow and distribution of granular media as compared to their effect at the interface of the physical body and granular media. Hence, both discrete and continuum simulations are useful when the flow and distribution of granular media in response to the external body is of interest. For applications such as a soft body deforming in response to drag experienced in the granular media, discrete and continuum simulations are unnecessary since the simulations serve just as the means to obtain boundary forces at the interface of soft body and granular media. Additionally, non-linear response as encountered during soft robots interacting with the granular media requires simulating the deformation of the soft body inside granular media for each small load step, which can significantly increase the total computation cost.

Roboticists have developed an empirical approach, called Resistive Force Theory (RFT) to calculate the drag forces at the interface between the intruder and granular media [5]. Previous work by Chen Li et al., has presented Resistive Force Theory (RFT) which states that the drag force experienced by a plate of a unit cross-section in granular media is a function of three parameters (i) depth of the plate, (ii) the angle of the plate with the horizontal, and (iii) the direction of intrusion for the plate. Chen Li et al. also reported the empirical results for the drag forces experienced by the plate intruding in granular media as a function of the above three parameters using Resistive Force Theory. This theory has led to the design of many successful robots [14, 15] as well as understand of how animals move on and within deformable ground [16, 17, 18].

1.3   Robot locomotion in granular media

Robot locomotion in GM is a challenging task because intruders moving through GM experience very large resistive forces along with non-zero yield stress that causes unpredictable solid/fluid transitions [2], and opportunities for sensing are extremely limited. These conditions
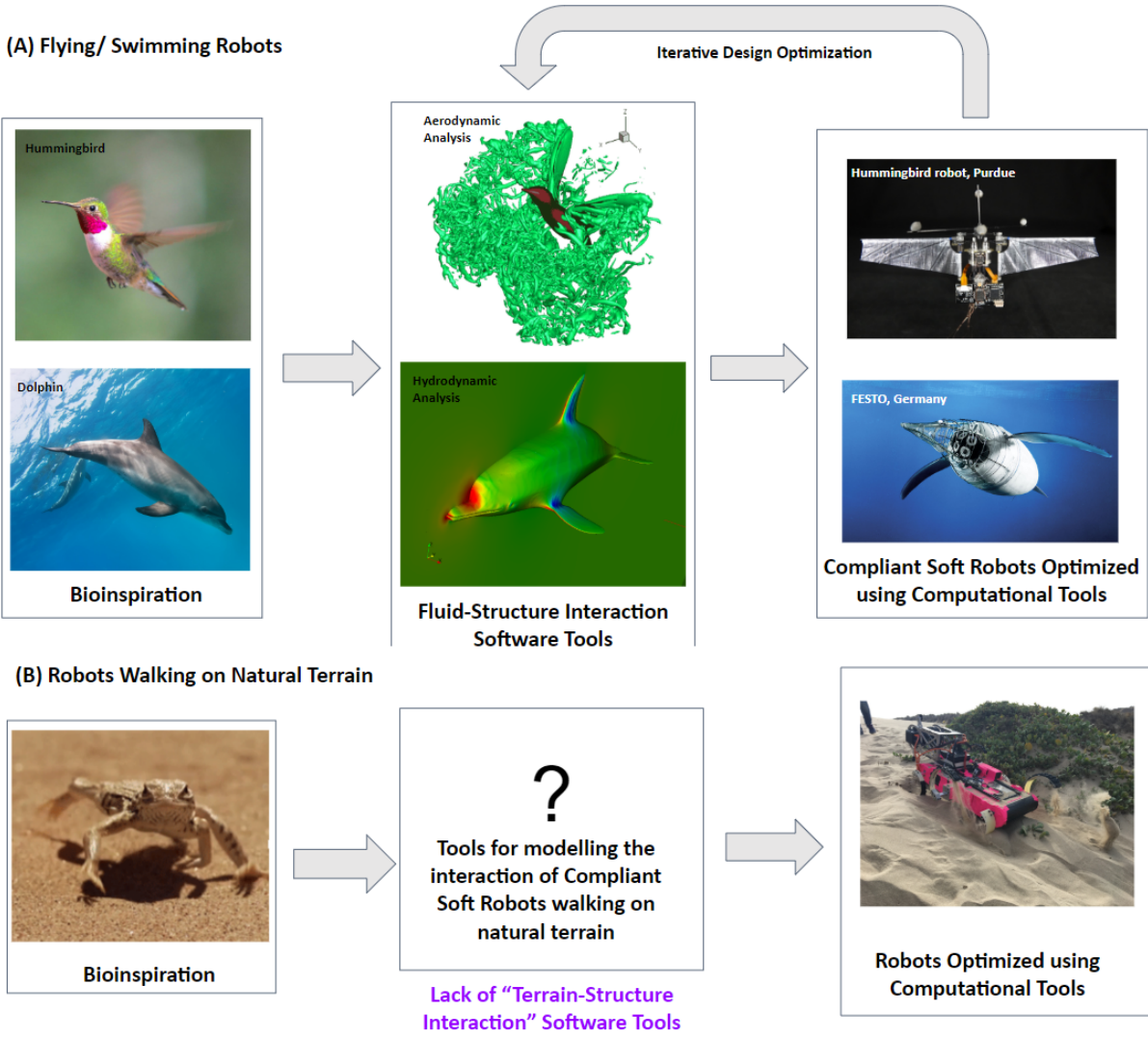
Figure 1.2: **Lack of modeling tools for granular interaction with intruders.** **(A)** Design iterations that are usually done for bioinspired flying and swimming robots. It involves an iterative design and optimization strategy using software tools. **(B)** Schematic showing the lack of quick computation tools to model the interaction of soft robots with granular media.

impose challenging requirements for design of an autonomous robot capable of locomotion within GM. For example, a robot at just 10 cm below the surface experiences resistive stress on the order of 10^4 Pa, requiring high-force actuation while minimizing overall robot size [5]. Robots designed to work in a particular kind of sand might not work in all kinds of sand as demonstrated by the failure of NASA's mole digger. According to the statement from NASA, the wet cohesive soil deprived the spike-like mole of the friction it needs to hammer itself to a sufficient depth. Thus, the properties of GM depend on moisture content, packing fraction of the grains, size, and shape of the grains. Furthermore, the high pressures and abrasive environment require the use of strong, robust materials. All moving components and the robot body must be tightly sealed so that sand grains cannot penetrate interfaces which results in rapid degradation of mechanical components and failure.

Locomotion on GM like sand in a desert is also very challenging because the medium behaves like a fluid-like flowing medium above a yield stress limit [9]. Many previous robots particularly NASA's Curiosity rover, have been stuck or performed poorly trying to move on deformable terrain. In granular environments, off-the-shelf legged robots can display poor performance because rigid, pointed feet may sink into the grains. However, with appropriate modifications to mechanical design or control [19] robots can perform well on GM but the performance is highly sensitive to the packing fraction [14] and the limb kinematics of the robot as the yield strength of GM increases with the increase in packing fraction [20].

Robot locomotion within the soil and subsurface environment has many applications such as inspection and exploration [21]. Early burrowing robots focused on drilling and scooping type mechanisms to excavate and loosen the soil [22]. These robots would create a tube through excavation within which the robot would travel. In this way, the early burrowing robots had much in common with pipe inspection robots. A major challenge of these early burrowing robots was their inability to maneuver when digging. Once a tube was established locomotion outside of this was challenging and thus these robots were relatively limited in their ability to explore wide

subsurface regions.

In recent years researchers have turned to animals and the principles surrounding their locomotion to solve many problems of robot mobility in a wide range of environments [23, 24]. There are many successful burrowing and digging animals from which roboticists have taken inspiration. In the context of locomotion on and within granular substrates, this bioinspired approach has proven successful in producing novel robot designs, gaits, and control methods. For example, the sidewinder rattlesnake *(Crotalus cerastes)* inspired a robot capable of traversing sloped granular media [16]. Other work has studied strategies for legged locomotion and for walking on deformable substrates inspired by a variety of lizards and crabs [25, 26]. In the context of digging, the sandfish lizard *(S. Scincus)* is one of the most capable subsurface travelers and has served as inspiration for numerous robot studies of swimming through granular material [18, 15]. Another burrowing robot inspired by the razor clam (E. directus) has been demonstrated to reduce drag force by sequential fluidization of the sea-floor soil through body expansion and contraction [27, 28]. One of the most emblematic digging animals that have inspired roboticists is the worm. The soft-bodied morphology, and a multitude of digging capabilities including through peristaltic actuation of lateral undulation, have led to several digging worm-inspired robots. Early worm-like robots were fabricated from rigid materials and actuators broken up into rotary segments [29]. More recent soft-robot-based fabrication methods have been used to generate worm robots capable of peristaltic actuation [30, 31, 32], lateral undulations, and combinations of body movements [31, 30]. Worm robots share many common features with snake robots (that focus on above surface locomotion), one common discovery is that anisotropic body friction in snake and worm robots can enable effective locomotion through simple actuation. Roboticists have used angled artificial scales and kirigami skins with angled flaps to generate anisotropic friction [33]. In primarily longitudinal locomotion modes, such anisotropic friction may be necessary for successful locomotion.

1.4   Underactuation in robotics

Underactuation is a technical term used in robotics and control theory to describe robotic systems that cannot be commanded to follow arbitrary trajectories in configuration space. This condition mostly occurs when the robot has a lower number of actuators than degrees of freedom. Roboticists have developed many underactuated robotic systems for locomotion in air, water, and on land to reduce the complexity of adding more actuators for complex trajectories.

Soft robots in particular have been at the forefront of underactuated robots because of their ability to deform due to the inherent elasticity or " material intelligence" [34, 35]. In contrast to the traditional rigid robots with limited degrees of freedom, soft robots have continuum deformation of the flexible body resulting in high DOFs. Variable-length tendons in the form of tension cables or SMA actuators have been introduced in the soft structure of the robot to have a controlled trajectory in locomotion and gripping [36, 37]. Recently flexoskeleton printing has shown how soft appendages can be made by 3d printing rigid structures on a flexible sheet and can be mechanically programmed to achieve a specific trajectory [38]. Many grippers have also been designed to grab different types of objects using clever actuation techniques like granular jamming and tendon enabled actuation [39, 40].

Intruders moving in granular media have to encounter very high penetration and resistive forces. An intuitive way to solve this problem is to have bulky high toque actuators at each joint of the robot to move it in the desired path. However, since these forces are dependent on the area of the cross-section of the intruder, adding multiple motors will make a robot system very bulky defeating the purpose of small-scale exploration. Particularly in appendage-enabled locomotion, it is beneficial to have embodied material intelligence rather than multiple motors at each joint. In this thesis, I describe in detail how I used underactuation and passive shape change to enable locomotion on and within granular environments.

1.5   Thesis Outline and Contributions

My dissertation focuses on addressing the following problems related to robot locomotion on and within granular media: a) GM changing the phase on the application of external force causing robots moving on grains to sink and slip, b) high resistive drag and lift forces causing challenging requirements on burrowing robot designs, and c) no navigation capabilities for intruders moving inside GM. My dissertation addresses these challenges by answering the following three research questions in the next four chapters: a) how can we design robot feet for improved mobility on GM to overcome sink and slip?, b) what are the design choices one should make for designing underactuated appendage-enabled untethered burrowing robots?, and c) is it possible to detect obstacles around a robot by measuring the resistance in the granular flow?

Granular jamming feet enable improved foot-ground interactions for robot mobility on deformable ground

Recent studies on dynamic legged locomotion have focused on incorporating passive compliant elements into robot legs which can help with energy efficiency and stability, enabling them to work in a wide range of environments. In this work, we present the design and testing of a soft robotic foot capable of active stiffness control using granular jamming. This foot is designed and tested to be used on soft, flowable ground such as sand. Granular jamming feet enable passive foot shape change when in contact with the ground for adaptability to uneven surfaces, and can also actively change stiffness for the ability to apply sufficient propulsion forces. We seek to study the role of shape change and stiffness change in foot-ground interactions during foot-fall impact and shear. We have measured the acceleration during impact, surface traction force, and the force to pull the foot out of the medium for different states of the foot. We have demonstrated that the control of foot stiffness and shape using the proposed foot design leads to improved locomotion, specifically a $\approx 52\%$ reduced foot deceleration at the joints after impact,

$\approx 63\%$ reduced depth of penetration in the sand on impact, higher shear force capabilities for a constant depth above the ground, and $\approx 98\%$ reduced pullout force compared to a rigid foot.

Initial investigation of asymmetric soft appendages for propulsion in granular media

Many animals use asymmetry in either body compliance or motion trajectories to generate propulsion in granular media. We study how an appendage with anisotropic stiffness can be used to generate propulsion in a granular environment. Firstly we perform experiments to understand how a soft appendage that's bent gets stuck in a deformed shape in granular media because of its yield stress. This motivated us to see how these appendages can get stuck in oscillation. We show how the advance (net forward motion) in sand depends on different parameters such as torque amplitude, frequency of the control signal, and stiffness of the appendage. We use two different control schemes and find optimal parameters in each. Finally, we model the behavior of thrust generation by the appendage using Resistive Force Theory for compliant structures in granular media. Our results show that there exists an optimum value of stiffness of the appendage for maximizing forward propulsion.

Underactuated appendages enable swimming in granular environments

Granular environments such as sand and soil are one of the most prevalent substrates on Earth, and yet one of the most difficult environments for robots to move within. Locomotion within granular media requires robots to overcome large depth-dependent forces, contend with non-zero yield stress that may cause unpredictable fluid/solid resistance forces, and all with extremely limited capabilities for sensing. In this work, we propose a novel method for an autonomous, untethered robot capable of locomotion within granular environments. A key advance in this robot is the use of underactuated appendages which enable both large propulsion

10

forces through limb motion, and obstacle sensing over a wide range around the robot. To optimize the design of granular appendages we performed experiments on an underactuated test appendage and identified the optimum morphological and actuation parameters for generating thrust. We investigated how the presence of an obstacle influenced the granular flow around a moving appendage, which led to an increase in the appendage force enabling the ability to sense obstacles in grains. The results from sensing and propulsion experiments were integrated into an untethered robot capable of subsurface locomotion in a controlled granular bed with a speed of ≈ 1.2 mm/s at a depth of 127 mm. Obstacle detection was demonstrated through experiments with embedded forces sensors on the appendages of the robot. Overall our results shed light on how soft, or underactuated structures can enable movement in granular environments with limited limb control while still enabling sensing capabilities.

Haptic detection of obstacles by measuring differential grain resistance in granular environments

Navigation and obstacle detection within granular media (GM) is challenging because vision and acoustic localization methods are hindered by the granular material. In this work, we explore a strategy for detecting obstacles in GM by measuring the changes in reaction force experienced by intruders as they move near an obstacle. We first performed experiments with a rotating beam instrumented with a torque sensor at the base to measure the change in forces experienced by the beam as a function of object proximity. We tested this for five different configurations of the obstacle with respect to the beam rotation plane, and we systematically varied the obstacle distance from the rotation axis from 0 to 14 cm. We observed that when the object disrupts the upward flow of GM pushed by the beam a large change in force is observed. However, objects below or normal to the rotation plane did not result in a detectable force change. To understand this, we measured the quasi-2D flow fields through particle image velocimetry. We demonstrated the feasibility of obstacle detection in GM using an appendage-driven robot

instrumented with force sensors on its limbs. Our results advance the understanding of obstacle localization in GM with many applications in robotics.

Chapter 2

Granular Jamming Feet Enable Improved Foot-Ground Interactions for Robot Mobility on Deformable Ground

Shivam Chopra, Michael T. Tolley, and Nick Gravish

Department of Mechanical and Aerospace Engineering, University of California San Diego, 9500 Gilman Dr., La Jolla, CA 92093

2.1   Introduction

Modern technology has created robotic systems that have excellent locomotion performance on flat ground [41, 42, 43], open water [44, 45] and air [46, 47]. However, robust ground-based mobility in realistic environments with flowable, uneven ground, has seen limited success [16, 14]. Robot mobility requires generating reliable and stable traction forces which are complicated on complex natural terrains like sand and rubble [48].

On the contrary, many terrestrial animals inhabit incredibly complex environments with

surfaces such as rubble, leaf litter, sand, mud, snow, and grass that pose high demands on foot placement, joint control, and body control. Particularly, walking on granular media like sand in a desert ($\approx 10\%$ of the Earth's land area) is challenging because it behaves like a fluid-like flowing medium above a yield stress limit [9]. In granular environments, off-the-shelf legged robots can display poor performance when walking on granular material because rigid, pointed feet may sink into the grains (Fig. 1a). However, with appropriate modifications to mechanical design or control [19, 14] robots can perform well on granular media but the performance is highly sensitive to the packing fraction and the limb kinematics of the robot as the yield strength of granular medium increases with the increase in packing fraction [20].

Strategies to improve legged robot performance on granular substrates have included decreasing the size and weight of the robot [49] to mitigate foot penetration, alteration of legged gait cycle [14], and using limbless robots to improve contact area [16]. The use of feet that change shape passively is another potential strategy that may improve locomotion performance on sandy surfaces [50, 51]. Many works have been published on adaptable feet by increasing the number of contact points per foot [52] and biomimetic foot mechanisms [53, 54, 55]. From a bio-inspired perspective, animals like camels and elephants have thick footpads (digital cushions) allowing them to distribute forces during bearing weight and to store or absorb mechanical forces [56]. Further, in the case of camels, the footpads are filled with fat which may keep them from sinking into the soft desert sand. The efficiency of footpads for animal locomotion in deserts serves as a motivation for this work. We hypothesize that a passively shape-changing and actively stiffness-changing foot can aid in improved locomotion on granular media.

Adaptable foot designs using granular jamming have been proposed for better locomotion on rough terrain [57, 58, 59], but these have not been designed or tested on deformable ground such as granular media. Granular jamming is the phenomena in which an enclosed collection of granular material (coffee grounds, glass beads, etc.) stiffen (jam) when put under negative pressure. In previous work, it was shown that granular jamming feet, when kept in a loose state,

a)

b)

c)

d)

Robot leg

Robot
foot

Granular
media

I. Free fall

II. Ground
induced
flattening

III. Stiffness
change

e)

5 cm

Oblong state

Tubing
to pump

Airtight
chamber
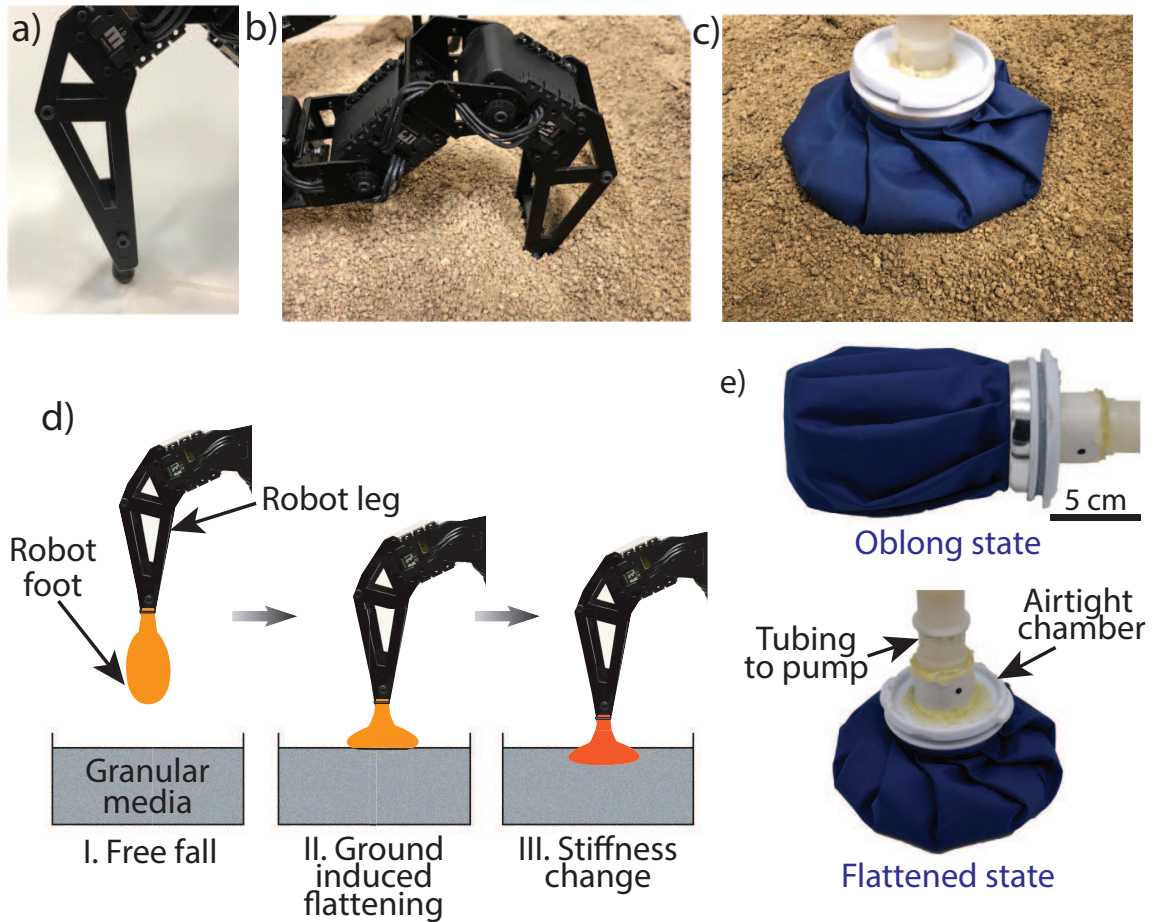
Flattened state

Figure 2.1: **Foot design overview**(a) A foot of a commercially available hexapod robot, (b) Robot foot with pointy end sinking in granular media (plastic beads of 3 mm diameter), (c) The proposed foot in flattened state on the sand, (d) Schematic showing the concept of the robot foot which after (I) free fall impacts the granular media and flattens (II) and then jamming is initiated to rigidify (III), (e) The proposed foot design in oblong and flattened state

leads to better foot ground contact, and when in an activated (rigid) state leads to better traction during walking [57, 58, 59]. Although it has been argued that damping in the foot is desirable for a non bouncy behavior [57], a purely soft foot can lead to problems as the propulsion forces from joint actuators do not push the body forward, but instead simply cause the robot leg to slip within the soft foot resulting in no forward motion [54]. Thus, for locomotion it is desirable to have a soft foot to adapt to surfaces, and a stiff foot to allow for generation of proper traction forces [59]. These traction forces are independent of the shape and surface area of contact for traversing on rigid ground but for granular terrain it is desirable for the foot to have least depth of penetration, making surface area of contact and shape of the foot important factors for maximizing the locomotion performance on granular media.

In this work, we propose a soft robot foot that flattens up after impact with the medium leading to more surface area causing less penetration, and then actively changing stiffness (Fig. 2.1d) using granular jamming. Rigid body impacts with granular media have been studied in previous works [60] but soft body interactions with granular media under free-fall impact and drag haven't been studied, which will be briefly discussed in this work. We performed a series of experiments with the proposed foot design for measuring the efficiency of the robot foot for locomotion in the sand by analyzing parameters like peak acceleration at drop, depth of penetration, shear force, and pullout force after drop and drag.

2.2   Foot design

A granular material enclosed by a flexible air-tight sheath can exhibit unique stiffness and shape-changing behaviors when positive or negative air pressure is applied. When the granular volume is at ambient pressure the grains within can behave like a fluid and thus the volume can change shape easily. However, when negative pressure is applied to the volume the enclosing sheath applies a pressure inward on the granular material which jam and the high friction between

16

the grains makes the volume behaves like a solid. This phenomenon is familiar to anyone who has handled a vacuum-sealed coffee bag, in the vacuum state the bag is rigid but when the vacuum is released it becomes soft and deformable. This phenomenon has recently been exploited to make adaptable robot grippers [39].

Our proposed foot design was focused on locomotion on granular media (sandy ground). The design was based on a granular jamming foot [59] but in addition to stiffness change, this foot was designed to exhibit shape change on impact. It consisted of an air-tight enclosing membrane and filling material for granular jamming. For the enclosing membrane, we used a commercially available ice pack. The membrane was made of inelastic textile material with pleats (Fig. 2.1e) such that on impact with the ground, the membrane would flatten and thus generate a larger surface area in contact, thus leading to less penetration in the sand for a given mass of the robot. The foot was about 8 cm in diameter in the elongated shape (when not in contact with a surface) and approximately doubled ($13 - 15$ cm) in cross-sectional diameter when pressed and flattened against the ground (Fig. 1d-e). We initially performed experiments with a latex membrane but ultimately did not use this material for several reasons. The durability of latex for interaction with the complex and rough ground was problematic as it failed quickly. Furthermore, the latex membrane elasticity required a substantially larger fill volume of grains which led to sub-optimal foot shape change abilities when interacting with the granular media. We found that an inelastic, tough textile reminiscent of taffeta was durable yet capable of appropriate shape change.

The filling material selection was based on a quasistatic loading experiment in which the foot was placed on a rigid substrate (wood) and was only free to move vertically. Weights were added on the top sequentially (Fig. 2.2) and the height of the foot above the ground was measured using pictures from a camera and tracking was done using MATLAB (The MathWorks, Inc.). We chose to test ground coffee, 3 mm diameter plastic beads, and $210 - 300$ μm diameter glass beads (Potters Industries with density $\rho = 2.51$ g/cm^3) based on past use in granular jamming and ease of availability [20, 61, 60]. As seen in the plot (Fig. 2.2) for a given mass on the foot,
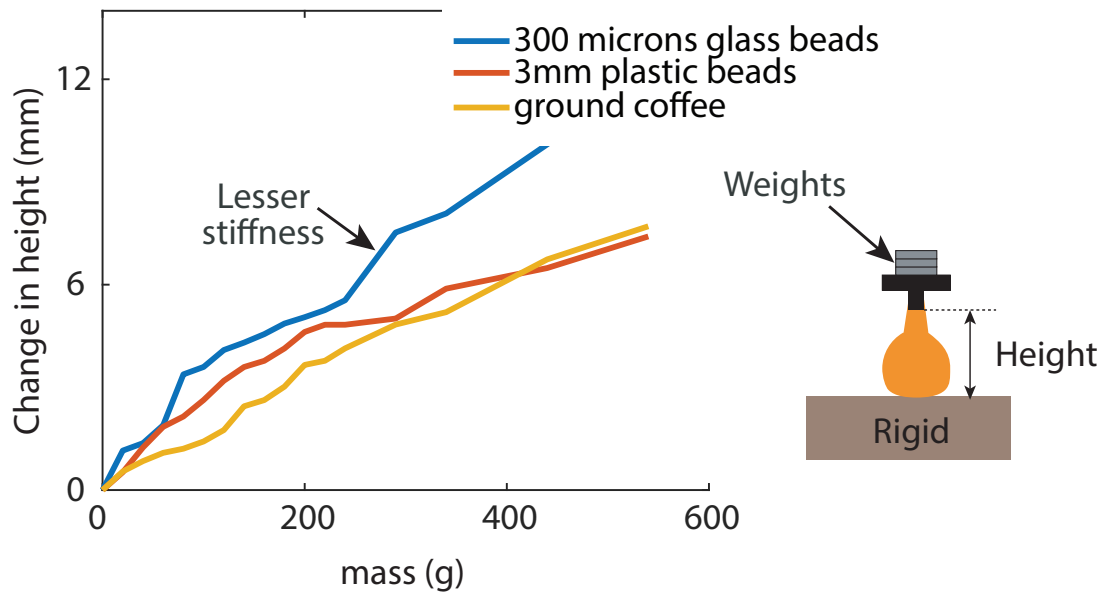
Figure 2.2: **Experiment to select the filling material for the foot**. The plot shows the mass with the change in height from the ground for three different materials and a schematic shows the experimental procedure. The mass is from the weights that are added sequentially

the change in height of the foot above the ground is highest in the case of glass beads because of lesser friction between the glass beads compared to other materials which lead to lesser stiffness of the foot. The filling material was filled up to the brim of the membrane and a tube was attached to the inlet with a sponge inside for jamming activation using the vacuum pump.

2.3 Materials and Methods

For a robot foot to walk on granular media it is desirable to have minimum peak vertical force on the joints where the foot is attached, minimum depth of penetration in the medium, a maximum shear force for forward propulsion in the foot (no slip), and minimum force required to lift the foot out of the medium. To determine how the stiffness state of the foot affected these parameters of foot-ground interaction we performed a series of experiments in two groups as follows: 1) foot drop experiments in which we allowed a foot to impact the ground at a realistic
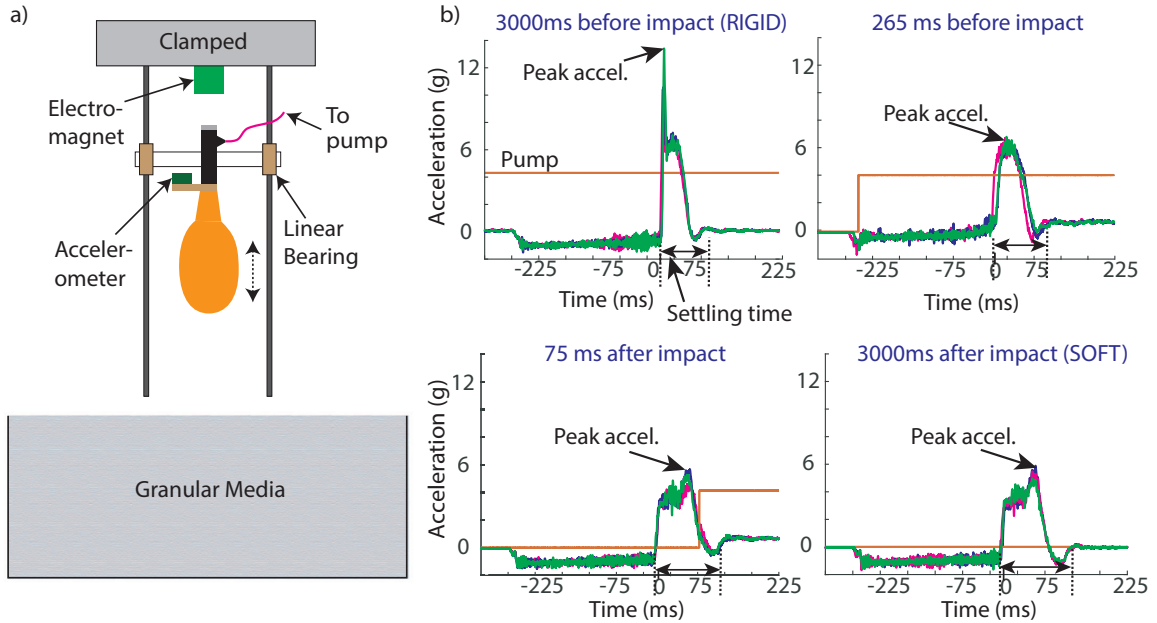
Figure 2.3: **Dynamics of the foot impacting granular media** (a) Experimental setup for the drop, (b) Plots showing the acceleration profiles in terms of acceleration due to gravity(g) as soon as the drop starts (3 trials each) for different vacuum turn on times. The time is relative to impact time of the foot (at 0 ms)

velocity, with variable foot stiffness, and 2) shear and pull out experiments in which we measure the foot's shear resistance against the granular surface and the force required to remove the foot. Below we describe these two methods in depth.

2.3.1 Granular material testing platform

An air fluidized bed of square cross-section 43 by 43 cm was filled with spherical glass beads of diameter $212 - 300$ μm (Potters Industries with density $\rho = 2.51$ g/cm^3) to a depth of 20 cm [Fig. 2.1(a)]. The floor of the granular testing platform was made of a porous plastic membrane with pore sizes smaller than the particle diameter. The porous floor was supported by an aluminum honeycomb structure with an enclosed volume below. The outflow of a shop vacuum was connected to the volume below the porous floor. The vacuum was 6.5 HP and was connected to a wall power source through a proportional relay controlled by an Arduino microcontroller.

By varying the voltage of the proportional relay we were able to control the airflow through the granular material. The volume fraction ϕ of the granular media was determined from image-based measurements of the bed height by the equation $\phi = M/\rho Ah$, where M, A and h are the total mass of the grains, area of the bed, and height of the bed respectively [20]. Before each experiment air flow through the porous membrane initially fluidized the medium [14] and then by slowly ramping down the air flow we got our desired packing fraction ϕ measured as 0.58 ± 0.03 which falls in the range of ϕ of loosely packed sand observed in desert sand dunes [62].

2.3.2   Foot drop experiments

For this set of experiments (Fig. 2.3a), an accelerometer (Analog Devices, ADXL326) was attached to the foot assembly for measuring the acceleration in the vertical direction on impact. The assembly was then fixed with a 3D printed fixture to a bearing setup consisting of two linear bearings and two 12 mm diameter steel shafts oriented vertically and clamped rigidly to the frame. The foot assembly was constrained to move only in the vertical direction and was supported at the base of the foot to inhibit tilting of the whole foot during impact. Further, the foot assembly was attached to a 9.525 mm diameter tube which was connected to a vacuum pump (Kozyvacu TA350), with 0.25 HP power and 3.5 ft^3/min flow rate, controlled by a custom Arduino program using a relay, which pressurizes the foot from 100 kPa (soft) to 30 kPa (rigid). A 12 V electromagnet was clamped to the top of the frame and an iron piece was glued to the top of the foot so that it could be held by the magnet at the start of the experiment. The signals from the electromagnet (on/off), the vacuum pump (on/off), and the accelerometer (analog) were recorded at the same sample rate of 4000 Hz through a data acquisition device (National Instruments USB-6001) using a MATLAB program. A high-speed camera (Phantom VEO410L) was used to track the trajectory of the drop carriage and the diameter of the foot after impact. For each experiment, the foot was attached to the electromagnet in the soft state (vacuum off) and the bed was fluidized. The data collection started as soon as the electromagnet turned off and the
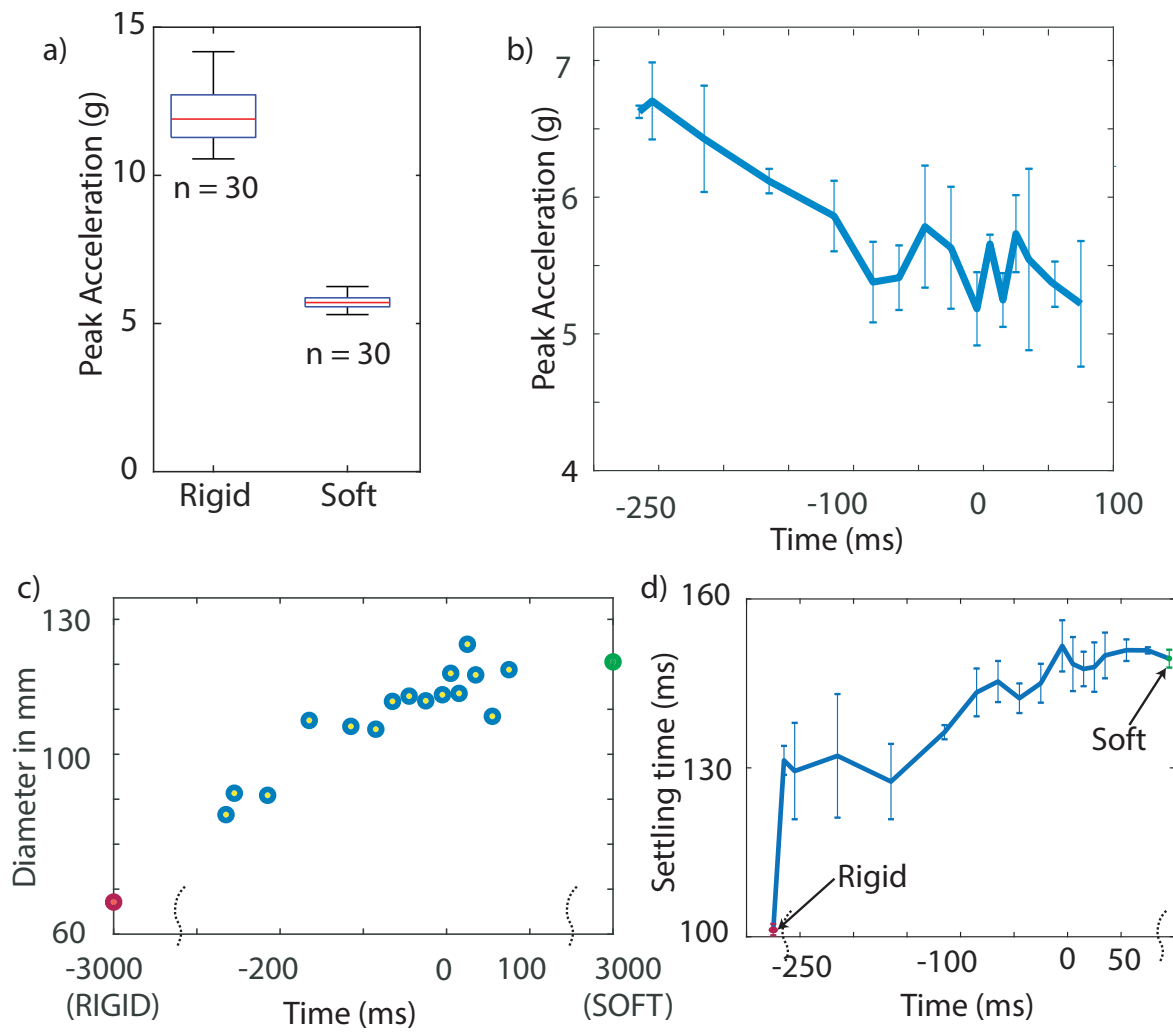
Figure 2.4: **Foot drop experimental results** (a) Bar plots for rigid and soft states of the foot for 30 trials, (b) Peak acceleration for the drop experiment at different time delays of the vacuum pump measured from Fig. 2.3b, (c) Diameter of the foot above the granular media after impact for different delay times of the pump, (d) Settling time of the foot calculated from Fig. 2.3b for different delay times.
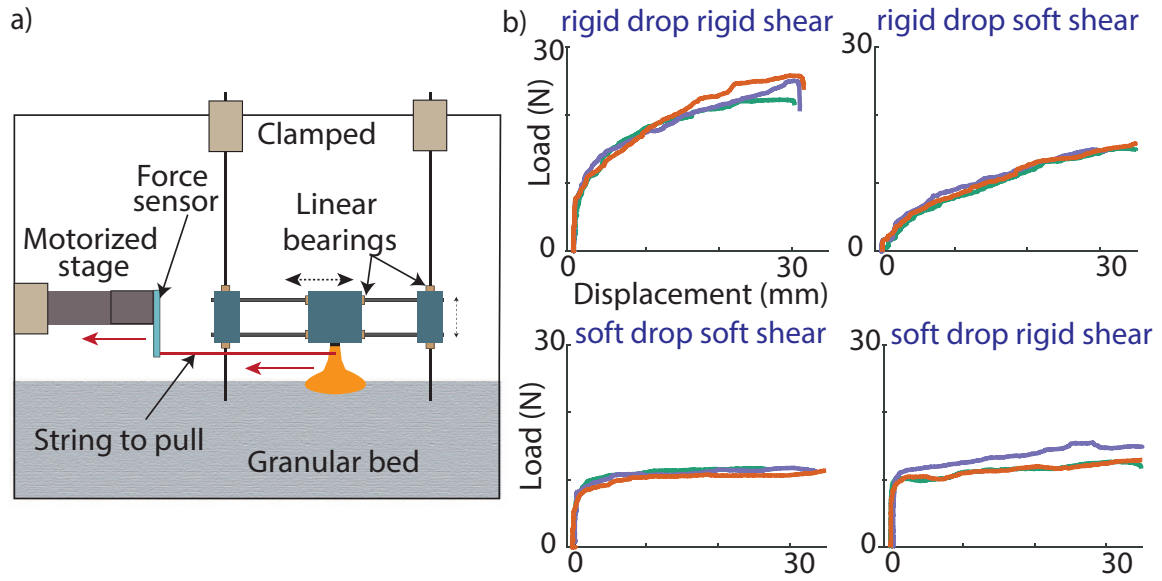
Figure 2.5: **Foot drag experiments** (a) Experimental setup for shear experiments, (b) plots showing shear force during drag with the displacement of the foot for four different states of the foot. 3 trials have been done for each foot state as shown

time to turn on the vacuum pump was calculated in reference to the time of impact from the ground for different delay times. All the measurements were taken for free fall of the foot from a height of 30 cm above the ground from the base of the foot corresponding to an impact velocity of ≈ 2.4 m/s.

2.3.3 Shear force and pullout experiments

For these sets of experiments, a similar setup as to the previous section was used with some modifications. A horizontal slider with linear bearings was added in addition to the vertical slider such that the foot was free to move horizontally and vertically, as shown in Fig. 2.5a. A motorized stage (Thorlabs MTS50-Z8) was attached to a 5 kg load cell that displaced the foot in shear through a tension wire. The load cell was connected to a load cell amplifier (FUTEK Inc.) and recorded using a data acquisition system (NI USB-6001) in MATLAB. For every trial, the assembly with the horizontal slider and foot was dropped from a height of 15 cm after fluidizing the granular bed with glass beads. The inelastic string was then affixed to one end to the
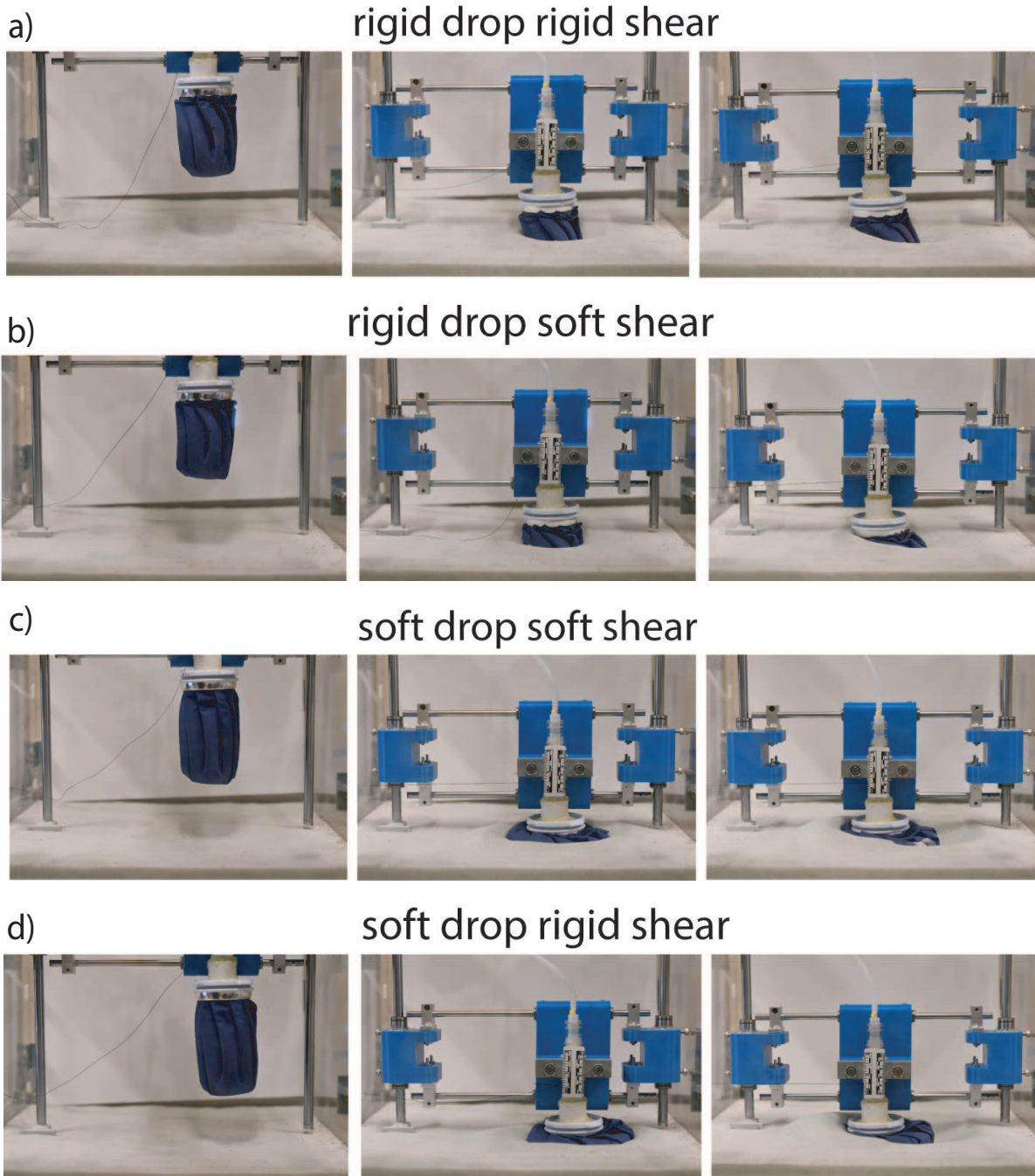
Figure 2.6: **Snapshots of drag tests** (a)-(d) Initial position, after drop and after drag snapshots for the four different conditions of the foot

load sensor and the foot on the other such that the foot could be dragged horizontally using the motorized stage with trajectory controlled using a MATLAB program with a constant velocity of 1 mm/s. The displacement of the foot was tracked using a synchronized camera and a MATLAB program. The experiment was done for four cases of foot states, (1) rigid drop and rigid shear (the vacuum was turned on before drop and remains on for the whole experiment), (2) rigid drop and soft shear (the vacuum was turned on before drop and remained on until drop but turned off for the shear experiment), (3) soft drop and soft shear (vacuum was never on), (4) soft drop and rigid shear (vacuum was turned on after drop).

Further, we directly measured the depth of penetration for all four cases after dropping from a height of 15 cm using images from the camera. For the rigid drop cases, the depth was equal to the change in the height of the foot above the ground as the foot didn't change shape. For the soft drop cases, we assumed that the flattened shape of the foot remained the same when dropped on a rigid surface and the granular bed. Using this assumption we calculated the depth of penetration (Fig. 2.7a) for these cases using images from the camera.

After the drag experiment was complete, the foot was pulled out of the granular bed by a force gauge (MARK-10), (Fig. 2.8a), and the force from the gauge was recorded using a data acquisition software (MESUR™gauge Plus). For calculating the weight of the foot assembly, the foot was placed on a rigid substrate and then lifted using the force gauge. The pullout force for all four cases was calculated by subtracting the weight of the assembly from the measured force to lift the whole assembly from the granular media after the drop-and-drag tests.

2.4   Results and Discussion

2.4.1   Dynamics of foot impacting the granular substrate

Fig. 2.3b shows the acceleration of the foot for four different delay times of the vacuum pump. We chose acceleration to be positive in the direction opposite gravity and acceleration is

normalized in terms of acceleration due to gravity (g). In all four plots, the acceleration drops from 0 g to -1 g as soon as the drop occurs. When the foot was dropped as rigid (vacuum on at 3000 ms before impact) on the granular bed there was a sudden increase in the acceleration to 12 ± 1 g and then the acceleration decreased because the foot penetrated the medium and then came back to 0 g as the foot came to rest which matches well with previous work [60]. On decreasing the vacuum delay time to 265 ms before impact, we observed a decrease in the peak acceleration to 5.5 ± 0.5 g and an increase in the settling time (time to come to rest) for the foot. Turning on the vacuum after the impact resulted in a reduced peak acceleration (Fig. 2.4a) and an increase in the settling time until the foot behaved like a completely soft foot with no prominent sudden peak and a slow penetration into the granular bed. The results show that by varying the stiffness state of the foot we can control the peak acceleration of the foot as it comes to rest. Such control may be useful to reduce the jerk on the body when the foot first comes in contact with the ground, in which case an initially soft foot would minimize this rapid change in acceleration.

Using the high-speed cameras, we also measured the diameter of the foot above the ground after drop for different pump times (Fig. 2.4b). For the rigid case, the diameter of the foot is the smallest because the foot doesn't change shape. As the vacuum onset time moves closer to the impact time the foot diameter after impact increases until it is saturated to a constant value because the foot starts behaving like a completely soft foot as an increase in the surface area of the foot leads to lesser penetration depth.

2.4.2   Shear force and pullout force measurements

We measured the shear resistance of the foot after impact experiments (Fig. 2.5). Force versus displacement plots for four different cases of foot state during drop and shear all show a shear force that increases with displacement (Fig. 2.5b). The force here was measured using the load cell and the displacement of the foot was tracked using the camera during the shear test. For the rigid drop followed by rigid shear case, the foot penetrates deeply into the granular medium

following impact as seen in Fig. 2.5c. Because the foot is so deep, and because it is maintained in a rigid state, thus the shear force rises very fast until ≈ 2 mm and then goes on increasing gradually up to 25 N for 30 mm. This continual increase in shear force with displacement is a result of the growing size of a pile of grains in front of the foot which causes an increase in drag. For the rigid drop followed by soft shear, the foot again penetrates deeply into the granular media, however when the vacuum is released and the foot turns soft before shear, the foot starts to slip within the granular medium causing the shear force to increase more slowly. Similar to the rigid-rigid case a grain pile forms in front of the foot causing a slow rise in force.

For the soft drop followed by soft shear case, the soft foot impacts the ground and thus is deformed to a flattened shape after coming to rest. Once the foot is dragged the shear force rises very quickly and then saturates at 11 N. Since the flat shape doesn't sink deep into the medium, the pile of grains is substantially smaller in this experiment which causes the shear force to remain relatively constant. Similarly, for the soft drop followed by the rigid shear case, the impact dynamics are the same as previously described with the foot adopting a flattened shape. Upon dragging laterally the shear force rose to a similar value as the soft drop then soft shear case, but in this experiment, the shear force has a gradual rise over the full displacement. As can be seen in the snapshots (Fig. 2.5c), the pile of grains that form in front of the foot is larger for the rigid dragged foot than the soft dragged foot. This is likely due to the soft foot slipping and deforming within itself. The results indicate that soft drops are optimal for achieving maximum shear force for a given height of the foot above the ground.

The pullout force is highest (Fig. 2.8b) for rigid drop cases because it goes deep in the granular bed (Fig. 2.7b) and requires about 10 times more force than the soft drop cases as the soft foot flattens up and doesn't sink in the medium. Pullout force gives us an estimate of how much force would be required to lift the leg of a robot after a step has been done. As the energy required to lift a rigid foot out of the sand is about 10 times as compared to a soft flattened foot, a soft foot while dropping is more energy efficient for locomotion on granular media.
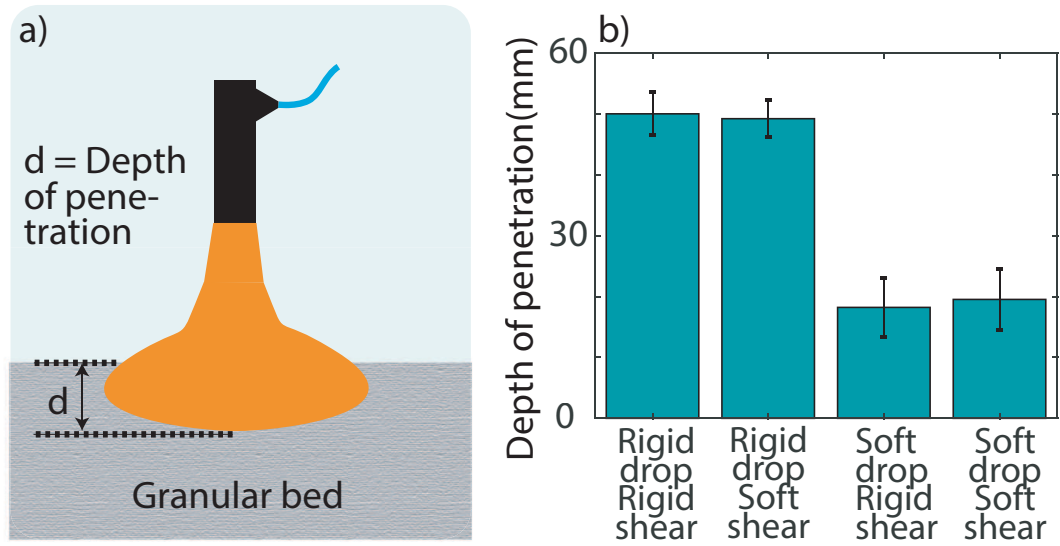
Figure 2.7: **Depth of penetration experiments** (a) Schematic showing the depth of penetration d, (b) depth of penetration measured using the camera for the four different cases for 3 trials of experiments
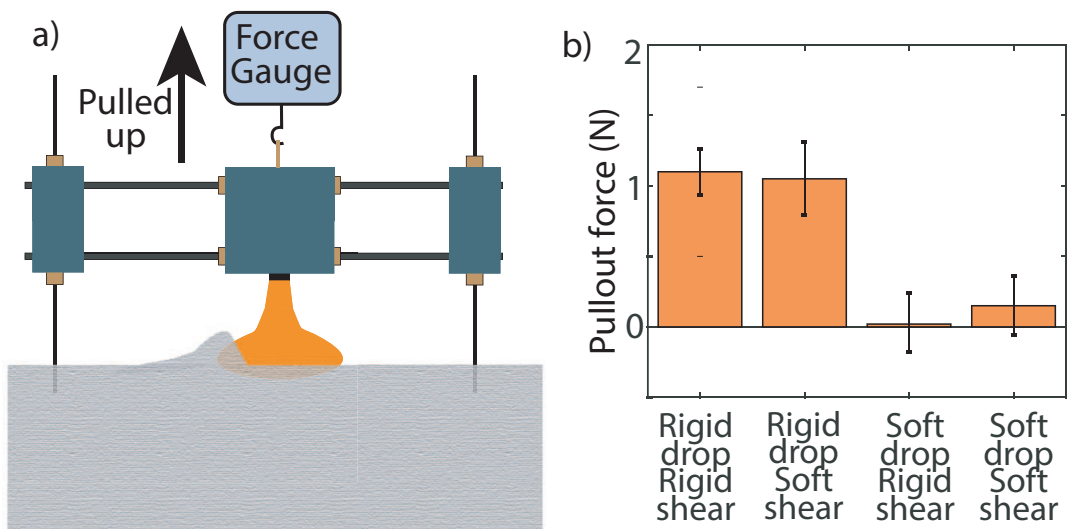
Figure 2.8: **Pull out force experiments** (a) Schematic showing the pullout force experimental setup (b) Pullout force for the four different cases for 3 trials of experiments

2.5 Foot performance comparison and selection

We summarize all our results in Fig. 2.9, where each bar plot has been scaled about the maximum value among the four cases. The shear forces in rigid drops are highest because of the maximum depth of penetration (Fig. 2.7b). The drag force F_d on a cylinder of diameter D is given by $F_d = \eta \rho g D d^2$ [10], where η characterizes the grain properties (surface friction, packing fraction, etc.), ρ is the density of the glass beads, d is the depth of penetration and g is the acceleration due to gravity. Assuming all the parameters to remain the same for these sets of experiments, $F_d = K d^2$ where K is the drag coefficient. A property of generating traction forces on granular material is that by penetrating deeper in the ground, we can generate more shear force before slipping. But this strategy comes at a significant cost as removal of the foot is much harder because of sand pile up and friction, and the effective leg length is shortened because of deeper penetration of the foot. Thus, the drag coefficient K indicates how efficient a foot is in supporting traction force for a constant depth d. We observe that the drag coefficient is highest for soft drop rigid shear along with minimum pullout force. Soft drop states come out to be the most efficient in terms of least depth of penetration and least peak deacceleration at the drop. Soft drop rigid shear and soft drop soft shear do not have much difference in performance, however, it is desired for a foot to remain rigid during transmission of propulsion forces so that no energy is lost in the deformation of the soft foot.

2.6 Conclusion

In this work, we have proposed a foot design that can passively change shape and actively change stiffness for improved locomotion on granular media. It was shown that the foot in the soft (unjammed) state damped the vertical impact forces (least peak acceleration) and flattened up for an increased contact area and when jamming was initiated the foot turned rigid to become more capable of transmitting horizontal propulsion forces. We have shown that using the foot
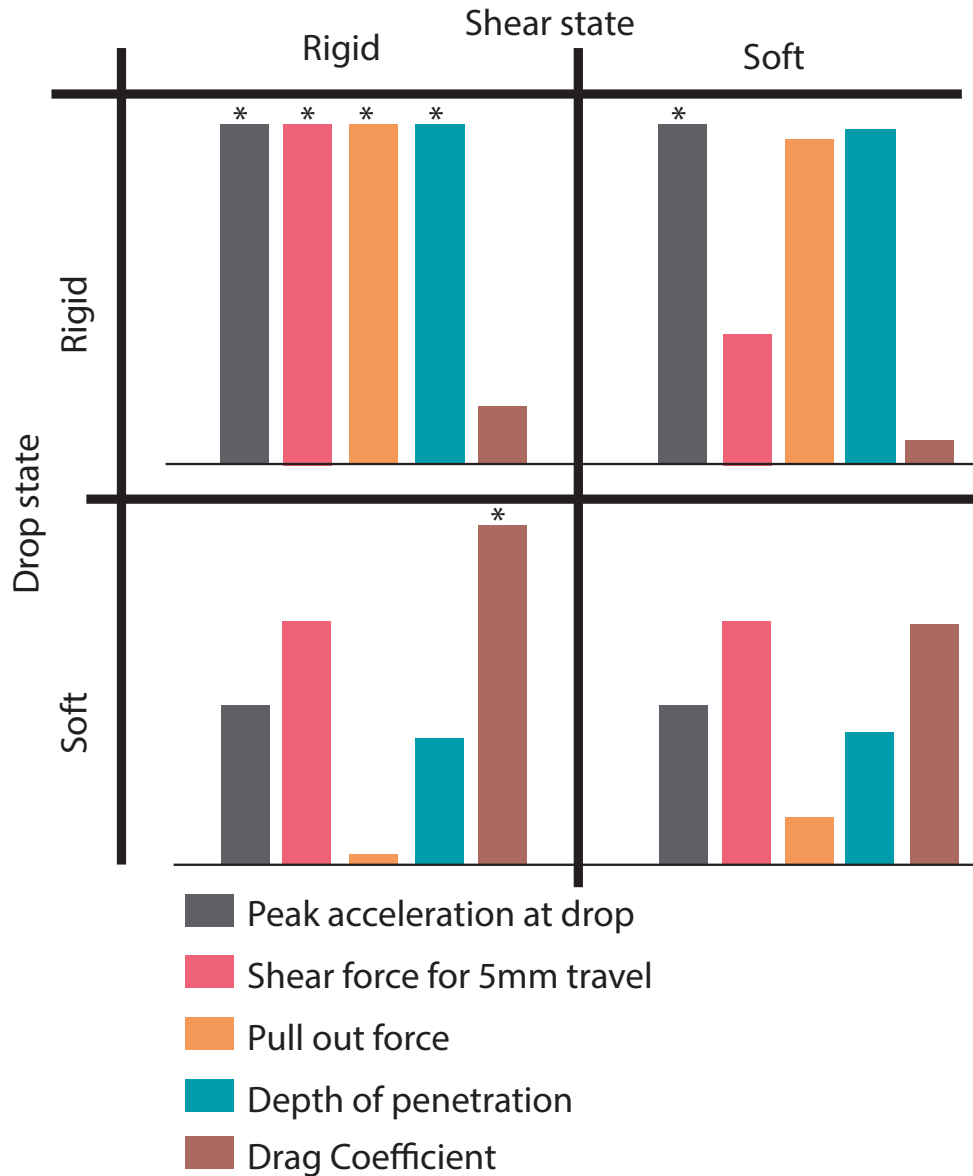
Figure 2.9: **Summary of results showing the parameters for four different cases of the foot.**
The plots are not scaled with the real units but scaled with respect to the highest value on each parameter which is shown with an asterisk(*) on top

design with pleats such that it is soft before the drop and then rigid during shear led to reduced foot deaccelerations at the joints, lower pullout force, lower depth of penetration, and greater drag coefficient at a certain displacement of the foot.

Future directions for this work may include more robophysical testing of the foot by changing the packing fraction of the granular media and by changing the slope of the bed. Future work could test the foot on the legs of the robot walking in desert or beach environment outside the lab thus size of the foot also needs to be scaled down and appropriate control schemes for the vacuum pump would need to be developed with the gait cycle of the robot

Acknowledgment

Chapter 3

Initial investigation of asymmetric soft appendages for propulsion in granular media

Shivam Chopra, Saurabh Jadhav, Michael T. Tolley, and Nick Gravish

Department of Mechanical and Aerospace Engineering, University of California San Diego, 9500 Gilman Dr., La Jolla, CA 92093

3.1   Introduction

Many animals employ asymmetry in motion to generate net thrust to move in granular media. These strategies include traveling wave actuation [18], non-reciprocating limb trajectories [63], anisotropic flexibility of the appendages [64, 65], and cyclic muscular contractions of the body [66, 67]. For soft-bodied organisms that burrow such as ocean dwelling worms a fundamental mode of granular interaction is with soft appendages [68, 64]. In this paper we perform experiments to understand how soft appendages generate propulsive thrust in granular

substrates.

Flexible appendages, fins, and body elements have been extensively studied in the context of fluid-structure interactions [69, 70, 71, 72]. However, the interaction of flexible appendages with granular media is not as well understood. There has been an increased interest in exploiting the flexibility of appendages for designing underactuated robotic systems for propulsion in granular material [73, 74, 75]. Locomotion in granular media results in much higher drag force compared to that of fluids, and thus instead of adding bulky motors at the joints, researchers have become interested in exploiting the flexibility to generate thrust for propulsion [76, 77]. In this paper, we will study how different parameters such as amplitude of input torque and stiffness of the appendage affect the forward progression of a model soft appendage in granular media. We will supplement our experiments with introduction of a Resistive Force Theory modification for soft appendages [5].

The motivation of this work also comes from our preliminary experimental studies where we bent a soft silicon appendage in air and in granular media. We observed that in air because of the elasticity of the appendage it returns to its initial state (Fig.3.1B,D). However when a soft appendage is bent in granular media, and released the appendage stays stuck in that bent configuration because of the finite yield stress of the medium (Fig.3.1A,C). This experiment instigated us to think how a soft appendage can behave in granular media when under oscillation.

3.2 Design of soft appendage

The soft appendage in this study has two components: an anisotropic skeleton and a soft sleeve. To generate asymmetry in motion, we wanted the skeleton to be very stiff in one direction to increase drag in power stroke and fully flexible in the other to reduce drag in return stroke. We used heat sealable taffeta (Seattle Fabrics) as the underlying flexible layer and adhered laser cut acrylic blocks on it. The acrylic blocks constrain the bending in one direction which

32
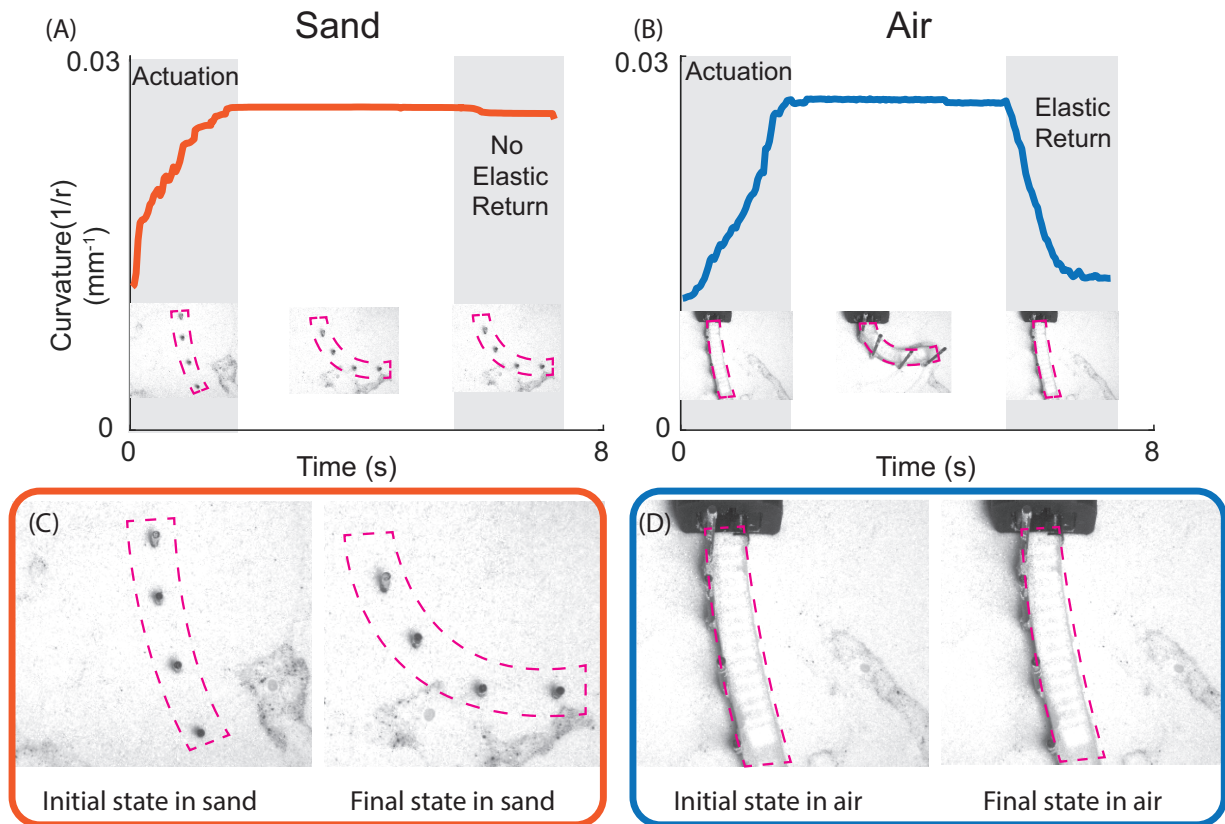
Figure 3.1: Soft appendage behaves differently in GM. (A) Curvature vs time plot when an appendage is bent in GM and released, the appendage stays stuck in that configuration and doesn't return to its original state. (B) Curvature vs time plot showing the same experiment when done in air, the appendage returns back to its original state because of its inherent elasticity. (C) and (D) are the snapshots of the initial and final states of the appendage in sand and air respectively.

leads to anisotropic stiffness [Fig.3.2c]. Similar designs have been explored in the context of fluid [75, 74] and granular locomotion [5]. In preliminary experiments we used a 3D printed laminate design [38] but we found that the polycarbonate backing layer was not strong enough in when subject to the granular media drag forces. We moved to a design which used Taffeta sheets because of its resistance to tensile failure and high flexibility after multiple oscillations under the granular reaction forces. The length of the skeleton was chosen to be 7.8 cm with six acrylic blocks $1.2 \times 1.3 \times 1$ cm. The sleeve was designed to enclose the skeleton from grains and to impart elasticity to the appendage. Two different enclosures were molded in a rectangular
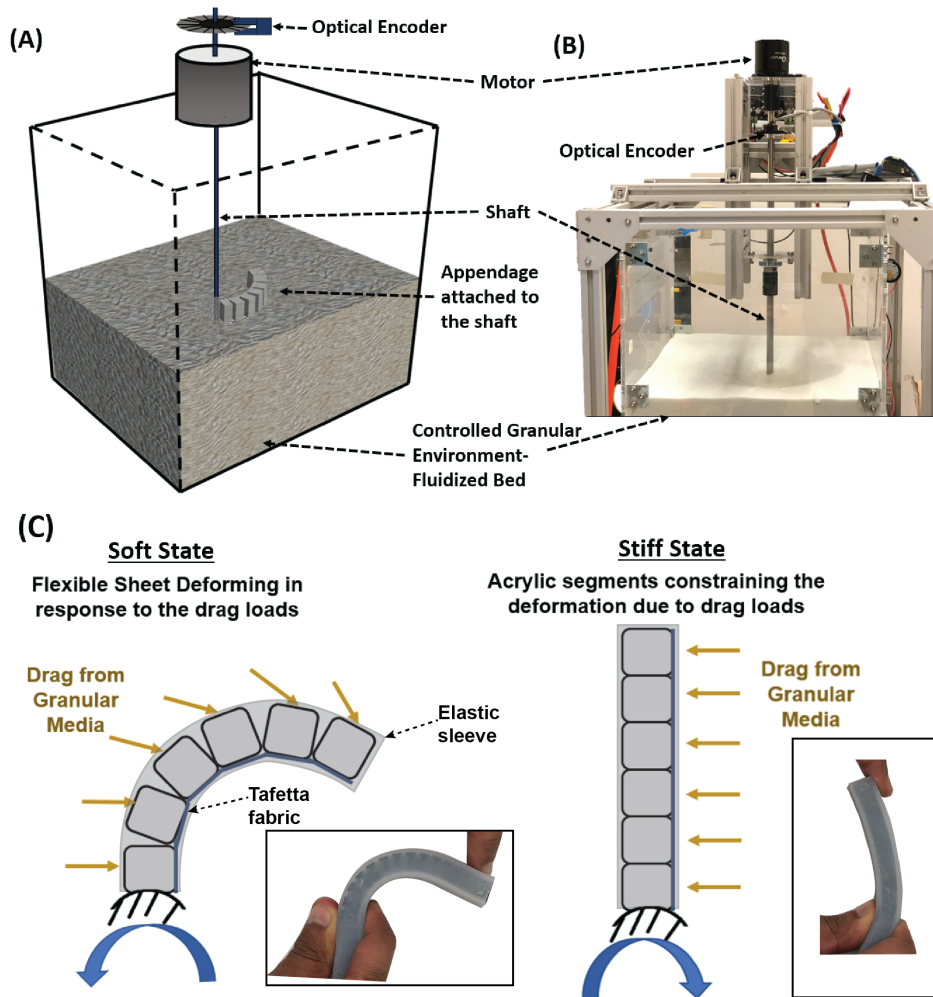
Figure 3.2: Design of the soft appendage. (a) Schematic and (b) picture of the experimental setup(c) Schematic of the appendage in (Soft State)- drag force is minimized by bending against the direction of rotation, (Stiff State)- the acrylic segments constrain the bending of the appendage during rotation in the other direction, thus maximizing the drag.

cross-section of thickness 2.5 mm using Dragonskin - 10 and Ecoflex - 10 (Smooth-On). Further,

0.127 mm thick spring-steel strips were slid in the sleeve for changing the stiffness.
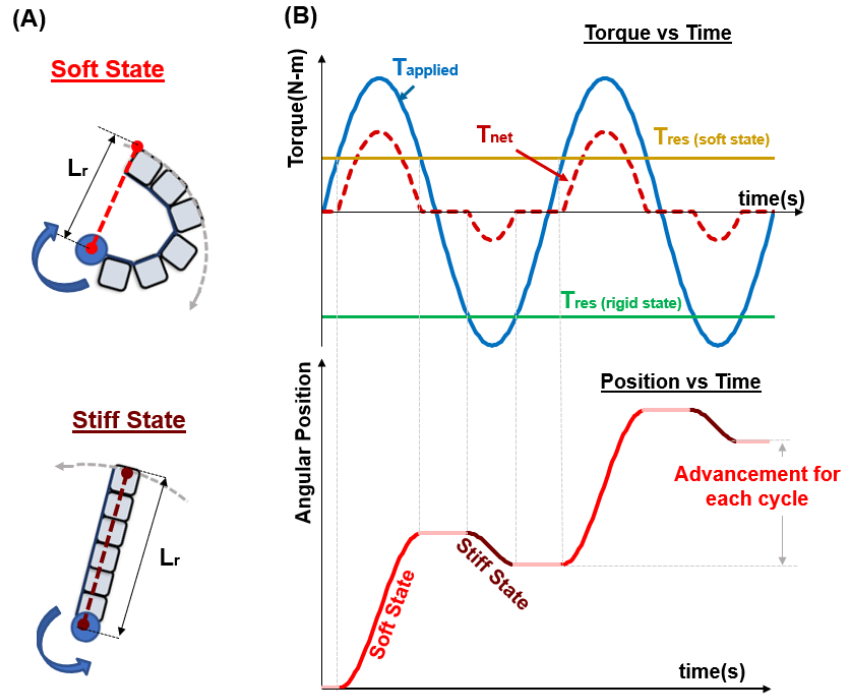
Figure 3.3: Modeling the position response of the appendage (a) Schematic showing the effective area of the appendage projected along the direction of rotation in soft and stiff state, (b) Torque and position response of the appendage as calculated from the model

3.3 Experimental Procedures

3.3.1 Setup

The soft appendage was actuated at one end through a 0.5 inch shaft connected to a brushless dc motor (Odrive 150KV) mounted above the granular surface. An optical encoder (US Digital, E6, 3600 CPR) measured the rotation of the shaft. The shaft was supported by bearings to counter any radial motion under oscillation. We used an Odrive motor controller for closed-loop current control. We interfaced the Odrive with a PC through a Labview program interfaced with Python that also recorded encoder position of the shaft.

All the experiments were performed in a controlled granular environment consisting of an air fluidized bed of cross section 43 cm by 43 cm filled with spherical glass beads (Potters Industries with density $\rho = 2.51$ g/cm^3) of diameter $212 - 300$ μm to a depth of 30 cm. The

packing fraction ϕ was calculated $\phi = M/\rho Ah$, where M, A and h are the the the total mass of the grains, area of the bed, and height of the bed respectively [20]. For each experiment we initially fluidized the medium by rapidly flowing air through the grains and then slowly ramping down the flow rate. This protocol enabled repeated preparation of a homogeneous granular material with packing fraction $\phi = 0.58 \pm 0.03$ which is in the range of loosely packed sand found in nature.

3.3.2 Procedure

We tested two different torque inputs to the motor and measured the current sent to the motor and the angular displacement from the encoder in each experiment for 10 seconds. The two control schemes used in this study were:

1) Sinusoidal actuation - An oscillatory time dependent sinusoidal torque τ was input to the motor such that $\tau = A\sin(2\pi f t)$ where A is the torque amplitude and f is the frequency of oscillation. For all these experiments we chose $f = 1$ Hz. 2) Time and displacement limited square-wave actuation: Torque input to the motor depended on maximum angle desired between two extreme positions of the appendage θ and the time taken to reach from extreme position to another T such that torque τ is

$$
\tau = \begin{cases} A, & \text{until } \theta = 180° \text{ or } T \leq \Delta t \\ -A, & \text{otherwise} \end{cases}
$$

The sinusoidal actuation method provided a simple state independent periodic torque. However, to limit the rotation angle of the appendage to a more realistic range when considering actuation on a robot ($180°$) we implemented the time and displacement dependent square wave actuation.

3.4 Modeling

We approximated the position response of the appendage by calculating the net torque acting on the appendage in its soft and stiff steady state configuration. The net torque is the
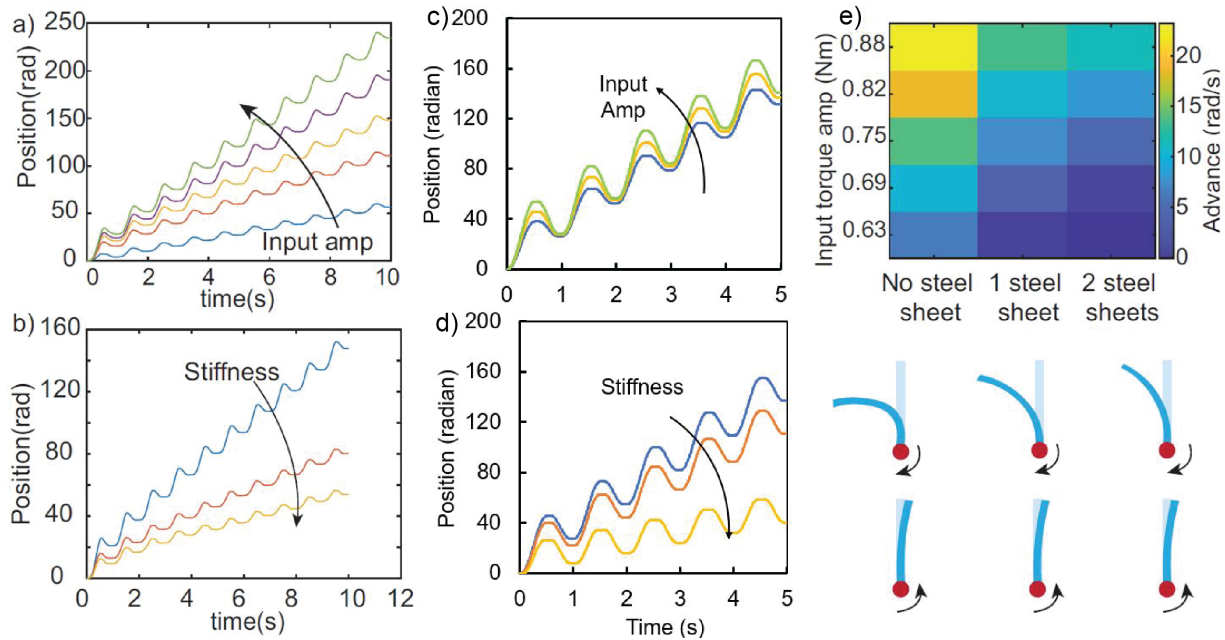
Figure 3.4: Open loop sinusoidal torque input data comparison with model (a) plot showing the variation of angular position with increasing input torque amplitude for Draginskin-10 for 1 Hz frequency (b) plot showing the angular position change with changing stiffness for torque amplitude of 0.75 Nm,(c) and(d) show the trends of increasing amplitude and stiffness from the model, (e) heat map of experimental results showing the effect of stiffness and input torque amplitude on advance of the appendage. Each box in the heat map represents mean of 5 trials.

difference between the torque applied by the D.C. motor and the resisting torque due to the drag force experienced by the appendage,(Fig 3.3 (B)- Torque). This drag force on the appendage is directly proportional to the cross-section area projected along the direction of rotation of the appendage (Fig. 3.3 (A)). The projected area of the appendage in the direction of rotation during stiff state exceeds the projected area during the soft state which causes asymmetry in the drag force. This asymmetry results in a net positive thrust during oscillation of the appendage (Fig. 3.3 (B)- Angular Position). If the resisting torque experienced by the appendage exceeds the applied torque, then the net torque acting on the appendage is zero and the position of the appendage remains unchanged. We approximate the deformed shape of the appendage during the soft state by using a commercial finite element tool (ANSYS Mechanical [78]). We model the steel plate (that is embedded in the appendage) with a uniformly distributed pressure load that acts normal
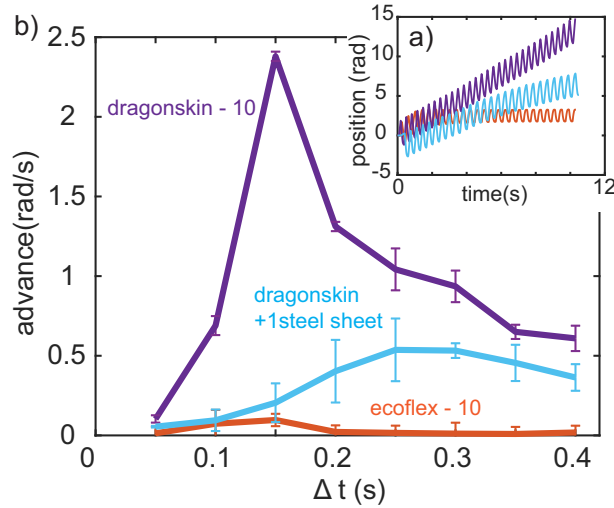
Figure 3.5: Closed loop control with maximum angle between extreme positions fixed at 180° (a) (inset) Plot of angular position vs time showing the advance of the three different appendages, (b)advance of the appendage vs Δt for 3 different appendages. Error bars show the standard deviation of 5 trials. Maximum advance was observed at $\Delta t = 0.15$ s for the appendage with Dragonskin-10 sleeve.

to the appendage. We use a scaling factor of 0.3 for the uniformly distributed load to account for the overall decrease in the drag force acting on the appendage due the decrease in projected area along the direction of rotation during deformation and the stiffening behaviour due to the acrylic segments. We assumed the drag force acting on the appendage in the soft state as a pressure with 30% magnitude of the drag force experienced by a vertical plate with the same area intruded horizontally in granular media [5]. Thus, using equations of motion, we calculated the position and velocity response [Fig.3.3] of the appendage.

3.5   Results and Discussion

3.5.1   Open loop oscillation

In time dependent sinusoidal actuation the angular position of the appendage continually advanced forward because of the lower drag torque in the return stroke. We oscillated the appendage at five different current magnitudes i.e. torque amplitudes(0.63 Nm being the minimum

torque required to move), and observed that the advance i.e. slope of the position plot, increases with the increase in the torque amplitude [Fig.3.4a]. Similar trends were calculated from the model where advance increased with an increase in torque amplitude.[Fig.3.4c]

To have a variation in stiffness, we tested 3 samples of appendages: 1) Dragonskin-10 sleeve 2) Dragonskin-10 sleeve with 1 steel sheet and 3) Dragonskin-10 sleeve with 2 steel sheets. We observed that the advance decreases with the increase in the stiffness of the appendage [Fig.3.4b]. This was because on increasing stiffness of the appendage, it didn't bend as much as its softer counterpart in return stroke and couldn't reduce as much drag to impart maximum asymmetry in motion. Our model also predicts similar behavior [Fig.3.4d].

We found that the advance goes upto 23 rad/s and the appendage swings back and forth for multiple rotations at high torque amplitudes because of no control over the maximum peak to peak oscillation angle. To limit this angle to $180°$ we devised a closed loop control scheme.

3.5.2 Closed loop oscillation

As the maximum angle of oscillation is fixed to $180°$ between the extreme positions of the appendage, we can get a more realistic insight on the advance. Further, the maximum time taken to move from one extreme to another extreme position Δt was varied from 0.05 s to 0.4 s in 0.05 s intervals.We tested 3 different samples and observed that for a constant torque amplitude $A = 0.63$ Nm and maximum peak to peak oscillation angle $180°$, Dragonskin-10 sample performs the best and has the maximum advance. Interestingly, the softest appendage, with Ecoflex-10, performs the worst and has zero advance after a few oscillations. We believe that a very soft appendage like EcoFlex-10 might not have sufficient elasticity to bend and return to its initial state, thus it generates almost zero advance [Fig.3.5a].

For these 3 samples, we measured the advance as a function of Δt and found that there exists an optimum value of Δt where the advance is highest. For the appendage with Dragonskin-10, the maximum advance was found to be at $\Delta t = 0.15$ s [Fig.3.5b]. On further observation it

was found that the input torque for $\Delta t = 0.15$s is equivalent to a square wave of frequency 3.5 Hz. In other words a time dependent (open loop) square wave of torque of frequency 3.5 Hz will give the same advance as $\Delta t = 0.15$s in this control scheme. For a low Δt the appendage oscillates at high frequency and thus there is a decrease in amplitude due to high damping in granular media. On increasing Δt, the appendage stops at the extreme position for some time and thus there is a decrease in advance.

3.6   Conclusion

Here we demonstrated how asymmetry can be exploited in soft appendages to generate thrust in granular media. We performed experiments using two different control schemes to demonstrate how different input parameters including torque amplitude, appendage stiffness, and the actuation rate influences the advance rate of moving forward. In open-loop torque control, we found that the advance increases with the increase in torque amplitude and decreases with the increase in stiffness. We model the behavior of this asymmetric motion using resistive force theory and the trends generated by the model validate the experiments. In closed-loop control, we limited the angle of oscillation to 180° and found that there exists an optimum value of stiffness for generating maximum advance. These results help increase the knowledge on the behavior of oscillating soft appendages in granular media which is of great interest to roboticists and biologists.

3.7   Acknowledgment

Chapter 3, in part, has been published and presented in Adaptive Motion of Animals and Machines, 2021. Chopra, Shivam; Jadhav, Saurabh; Tolley, Michael T.; Gravish, Nick, AMAM 2021. The dissertation author was the primary investigator and author of this paper.

Chapter 4

Underactuated appendages enable swimming in granular environments

Shivam Chopra, Drago Vasile, Saurabh Jadhav, Michael T. Tolley, and Nick Gravish

Department of Mechanical and Aerospace Engineering, University of California San Diego, 9500 Gilman Dr., La Jolla, CA 92093

4.1   Introduction

Granular media is one of the most common surface substrates occurring in many forms such as soil, sand, and extraterrestrial regolith [79]. Although a considerable amount of research has been devoted to swimming in water or flying in the air, rather less attention has been paid to digging and burrowing in granular media (GM). Recently, the study of robots capable of burrowing in GM has been of growing interest due to their wide range of potential applications in search and rescue operations, mining, studying biological organisms, seabed, underground and extraterrestrial exploration, ground resiliency, and contaminant monitoring [1].

Robot locomotion in GM is a challenging task because intruders moving through GM

42
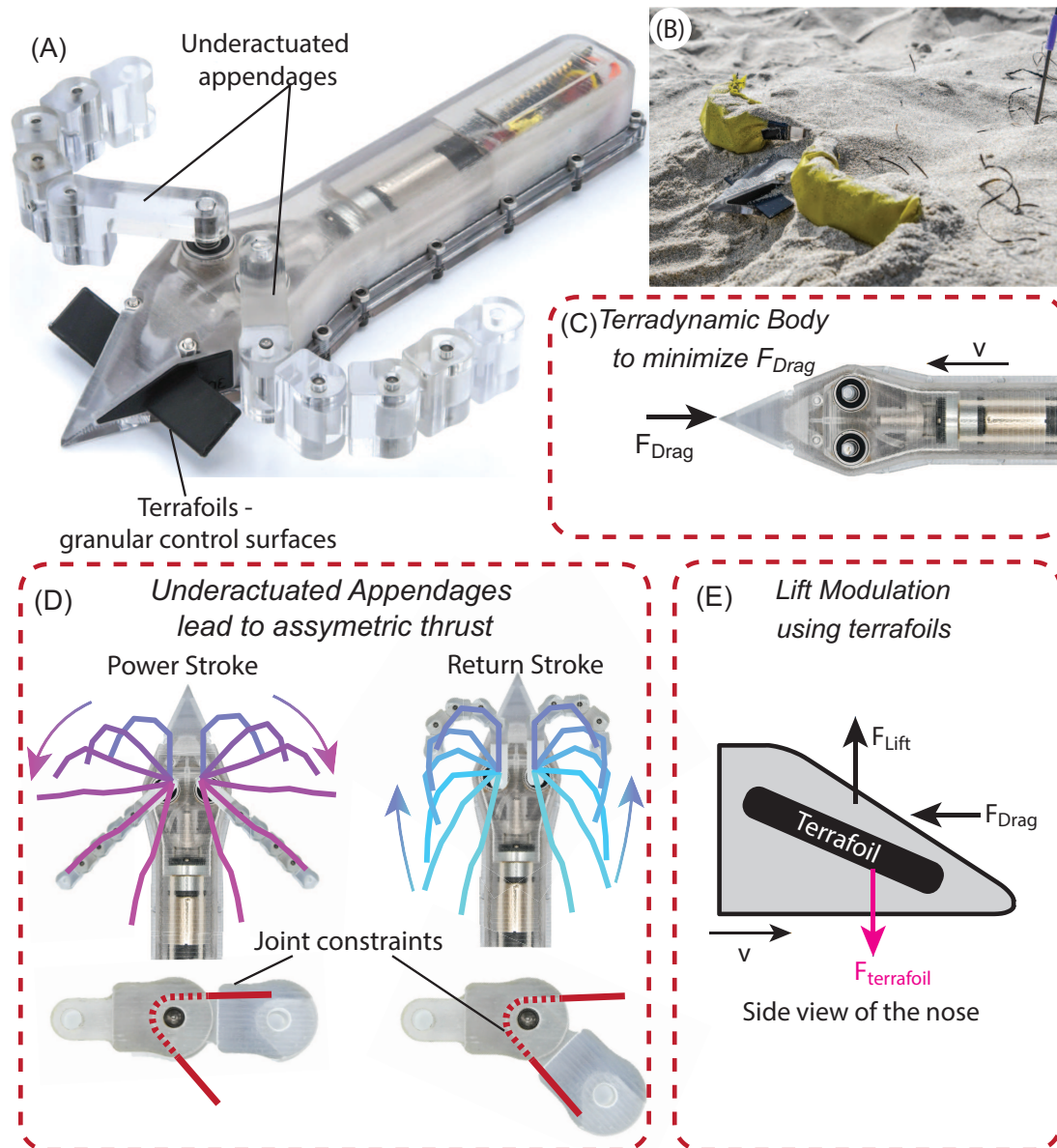
Figure 4.1: **Overview of robot** (**A**) Photograph of the robot showing the underactuated appendages and terrafoils (granular control surfaces inspired from elevators and diving planes in airplanes and submarines respectively). (**B**) Picture of the robot digging at a beach in San Diego. (**C**) Top view of the optimized terradynamic body for minimizing drag forces in granular media. (**D**) Time-series images showing the motion of underactuated appendages (created from tracked joint positions using the camera) in the power stroke and return stroke. The appendages were designed to experience minimum drag in return stroke and maximum propulsive force in power stroke for generating a net thrust to move forward. (**E**) Side view of the sandfish lizard-inspired asymmetrically tapered nose with the terrafoils added to counter the lift force so that the robot stays submerged during locomotion.

experience very large resistive forces, non-zero yield stress that causes unpredictable solid/fluid transitions, and opportunities for sensing are extremely limited. These conditions impose challenging requirements for the design of an autonomous robot capable of subsurface locomotion in GM. For example, a robot at just 10 cm below the surface experiences resistive stress on the order of 10^4 Pa, requiring high-force actuation while minimizing overall robot size. Furthermore, the high pressures and abrasive environment require the use of strong, robust materials. Lastly, all moving components and the robot body must be tightly sealed so that sand grains cannot penetrate interfaces which results in rapid degradation of mechanical components and failure.

Early efforts to create robots capable of subsurface locomotion in GM largely focused on two fundamental approaches: 1) robots that use body expansion and elongation, and 2) undulatory robots that use body bending to effectively "swim". Earthworm-like peristaltic actuation has been incorporated in many burrowing soft robots [31, 80, 81, 29]. Peristaltic actuation takes place through cyclic body expansion and elongation, which enables control of wall-friction forces for anchoring (high-friction), and extending forward (low-friction). Furthermore, this approach when tested in water-submerged GM like that of the ocean floor also enables drag reduction on the robot through fluidization of the nearby GM due to the interstitial water motion [82, 83, 84]. However, peristaltic actuation for GM locomotion presents challenges for autonomous, untethered operations. Many of these robots are made of soft, elastic bodies and use soft pneumatic actuators and thus need to be connected to a pump. While it is feasible for soft robots to operate with onboard pumps, pneumatic actuation within GM presents a further challenge as the pump must be able to pull in the surrounding air which may be challenging at higher depths in GM and impossible in submerged GM.

Undulatory, "sand-swimming", robots move through lateral body bending and propulsive swimming forces that are generated as the body sweeps through the sand. This method of locomotion was inspired by the sandfish lizard which is capable of rapidly burrowing into the sand to escape predators [18]. The early studies of undulatory locomotion in GM lead

44

to foundational developments in the modeling of GM through the application of the resistive force theory (RFT) which was originally developed for locomotion of worms in viscous fluids. Comprehensive experiments, numerical simulation, and RFT calculations enabled researchers to design and optimize a seven-link undulatory robot and to study optimal swimming gaits in the sand. Undulatory locomotion is a compelling method for movement in GM, however previous robot experiments took place in shallow, low-density plastic beads, and thus the resistive forces were comparatively small. In real GM the forces are substantially larger, and it is unclear if current actuators would be capable of generating motion in natural sand. Additionally, the tether connected to peristaltic actuation-based robots can interfere with the motion of the robot, reducing the propulsive force. Furthermore, energy is spent in moving the grains while expanding for anchoring, making these robots slow and inefficient. This strategy may work for cohesive wet sand, where these robots can make a tunnel to move in but is not that effective in submerged and dry sand.

More recent work has demonstrated several promising approaches for granular locomotion. Robots that "grow" by extending only at the tip have demonstrated impressive locomotion capabilities using either a plant-root-inspired everting skin [85, 86] or a growing 3D printing filament extruder mechanism [87]. These methods drastically reduce the friction against the body since only the tip of the robot is moving through GM. However these approaches necessarily are tethered, and their capability for maneuvering within GM can be limited. Robots that use the helical motion of an auger have also been recently developed [88, 80] to self-drill through the sand. These robots show promise however current implementations have only been tested for locomotion on the surface of GM, rather than for subsurface locomotion. Lastly, a recent appendage-driven robot was developed that used anisotropic compliance in fins to produce forward propulsion as the fins symmetrically oscillated [89]. Numerical optimization for this robot was performed using RFT calculations to determine the optimal actuation parameters.

Recently, Naclerio et al.,[90] developed a fast-everting robot, inspired by plant roots and

the sand octopus, which was able to achieve maneuverability using fluidization to modulate lift and tendons to steer. The need to be connected to a powerful pump with a high flow rate at all times makes this robot not an ideal choice for applications that require no support from the surface [91].

Appendage-driven locomotion in GM has several advantages over other approaches including 1) appendage sweep can possibly detect obstacles away from the body, 2) can generate large propulsive forces through a wide "stroke", and 3) permits easy steering through differential appendage drag. Appendage-enabled locomotion has been widely studied for transportation in air, water, and on-ground surface which has informed the design of many successful robots with exceptional dynamic locomotion [92, 93, 14, 94, 95]. However, because of the lack of physical models for the interaction of appendages having underactuated bending modes, appendage-enabled locomotion in GM is not well studied [89, 96]. Furthermore, using appendages for granular locomotion presents challenging design hurdles that must be overcome. Appendages must generate high force during the power stroke, and low force during the return stroke, requiring appendage reconfiguration through the locomotion cycle. However, it is unfeasible to fully actuate appendages for reconfiguration because of the high-force requirements in GM. One method for appendage reconfiguration that has been explored in viscous fluids is by using passive elasticity [77]. Progress has been made in understanding the role of flexibility and variable stiffness of soft appendages to generate propulsive thrust in GM [76, 77, 97]. In viscous fluids, the shape, and ultimately the resistive drag force on an appendage can be controlled by changing the rate of appendage motion (since forces are velocity dependent). However, this approach will not work in GM since the resistive forces are independent of speed (speed < 0.5 m/s) [98, 99]. An even more fundamental challenge for flexible appendages exists in GM: due to the nonzero yield stress, an elastic appendage can get "stuck" in a deformed configuration if the elastic restoring stress is below the yield stress [100, 101]. Thus, appendage-enabled locomotion requires limbs to be capable of reconfiguration throughout the locomotion cycle yet it is unclear if passive elastic

46

structures would be beneficial.

Biological locomotion in GM is often characterized by rhythmic and repetitive movements of appendages [63, 102] or soft slender bodies [18, 103] or coordinated combination of both to achieve propulsion [65, 64]. This locomotion is achieved due to the complex interaction of the forces exerted by the body and the external forces exerted by the GM [104]. Many animals move with non-reciprocating trajectories [102] or exploit the intrinsic morphology of their soft underactuated appendages [105] to generate asymmetry in motion for moving within GM. Further, animals use appendages extensively for accomplishing a variety of tasks in GM such as propulsion and steering (e.g., mole crabs, mole crickets, sea turtles, gopher tortoises [63, 102, 105, 106]), sensing of the flow to detect obstacle/prey (e.g., arthropods [107]), as well as transport of granular material (e.g., ants [108]). Sea turtles in particular have been known to dig their nest at the beach, crawl on the shore and swim in the ocean using the anisotropic stiffness of the appendages[109, 105]. They also dig in the ocean floor for foraging using the appendages in a motion similar to that of the arms while swimming the breaststroke [110, 111]. Sea turtle hatchlings have appendages much larger than their bodies to displace sand and generate propulsive forces in a synchronous effort to dig and surface out of their nest as deep as ≈ 40 cm [112]. An ideal case for propulsion while swimming in GM is to minimize the reaction torque in the return stroke and maximize it during the power stroke. For this work, we took inspiration from appendage enabled digging in animals, to design a robot with appendages moving in a sweep through and propel motion.

This work presents a terradynamic design of an easily deployable untethered robot, driven by two anisotropic underactuated appendages, which can sense obstacles in GM (Fig. 4.1A, Movie 1). The appendages move in a sweep and propel motion generating asymmetric thrust by displacing the sand to swim in grains. This work makes the following contributions in swimming and in granular environments that enable our robot design: 1) Design optimization for underactuated appendages in GM (Fig. 4.1D), 2) Design of terradynamic control surfaces

47

("terrafoils") to counter the granular lift forces for ensuring continuous horizontal locomotion (Fig. 4.1E), and 3) Haptic detection of the position of obstacles around a moving body. Ultimately we implement these designs into tethered and untethered robots capable of locomotion in GM. We demonstrated that the robot can function untethered in a challenging natural environment (at the beach) which hasn't been demonstrated by any other robot (Fig. 4.1B).

4.2 Results

This section includes details of the robot design and results from the experimental tests for appendage characterization, robot design, lift modulation, sensing objects in sand, and demonstrations of the robot in a natural environment and the lab.

4.2.1 Robot Design

The robot was driven by two appendages through a sweep and propel motion as seen in animals [102, 105]. To keep the actuation simple, the appendages were designed to be actuated by a single motor through a gearbox by using a PID controller on the motor encoder. We selected a single motor for bilateral limb actuation to reduce the cross-sectional area of the body for reduced drag forces in GM (Fig. 4.2A, B). The mechanical system used to drive the appendages converted the rotation of the motor's output shaft, placed on the central axis of the robot, to rotation at the base of both appendages, using a worm drive transmission (Fig. 4.2C).

The motor selection criteria were based on having the least cross-sectional area possible while providing enough torque to drive the appendages. A DC motor with a planetary gearbox was used, as the stages of the gearbox stack axially, increasing the length and keeping the cross-section constant. The body was designed to have an O-ring and two water-tight bearings to ensure that it is sand and water-tight.

Terradynamic body design

Forces within GM can be extremely high and thus to enable locomotion of a robot, we needed to minimize the drag on the body of the robot. Our goal was to choose the body with the least projected area perpendicular to the direction of motion. To measure the drag force, we dragged bodies with four different profiles, but with constant frontal projected cross-section areas, at a constant velocity in a controlled granular environment (Fig. 4.7A, B). We found that the body with a uniform cross-section (shown in blue in Fig. 4.7B) experienced the maximum drag force (F_D). The tapered body (green) with the same length L experienced a drag force $\approx 15\%$ lower than the constant cross-section body (blue). Reducing the length of the body by $1/4$ L, we found that the drag reduced by $\approx 7\%$, likely due to the reduced skin traction between the grains and the body. We lastly tested a body with serrated edges (orange) but did not find a considerable difference in force with the non-serrated tapered body (green) in both forward and backward directions. These experiments led us to choose the tapered body design instead of a solid body with a constant cross-section. We also incorporated a shovel-shaped nose in front of the body to counter the upward lift forces acting on the body (Fig. 4.2B).

4.2.2   Appendage design and characterization

After designing and conceptualizing the robot body, we performed a series of tests to find the optimum appendage curvature for generating maximum forward thrust on the robot. To contend with the large resistive forces in GM, we used rigid links with revolute joints constrained by joint angles. Each appendage consisted of five links actuated at the base. Each link had variable joint constraint angles at $15°$ increments enforced by pins inserted into one of 12 holes (Fig. 4.3A).
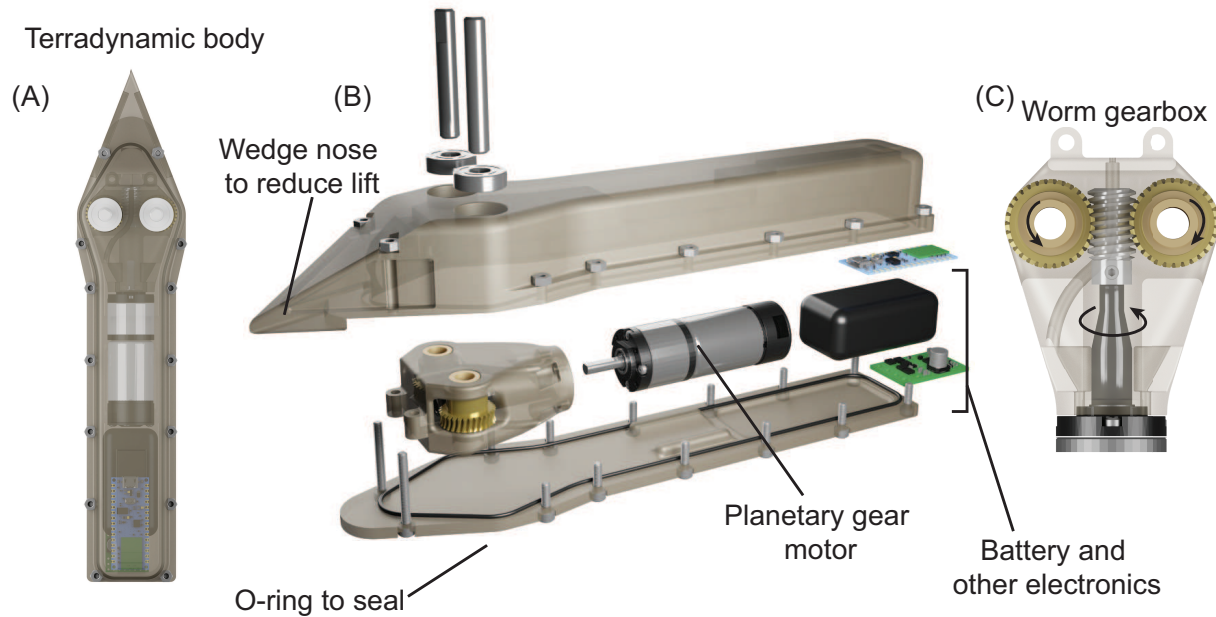
Figure 4.2: **Robot design.** (**A**) Top view of the terradynamic body for the robot. (**B**) Exploded view of the robot body assembly with different components. Planetary gear motor actuated both the appendages through a worm gear transmission. The robot was designed to be fully untethered with all the electronics encased in the body, fabricated using a resin 3D printer. An O-ring and two water-tight bearings were used to seal the body from sand and water. The appendages were driven by the motor through the two shafts attached to the gearbox. Wireless communication was done through a low-level messaging protocol (MQTT) through Wifi. (**C**) To keep the robot actuated by a single motor, a worm gear mechanism was integrated into a 3D printed gearbox.
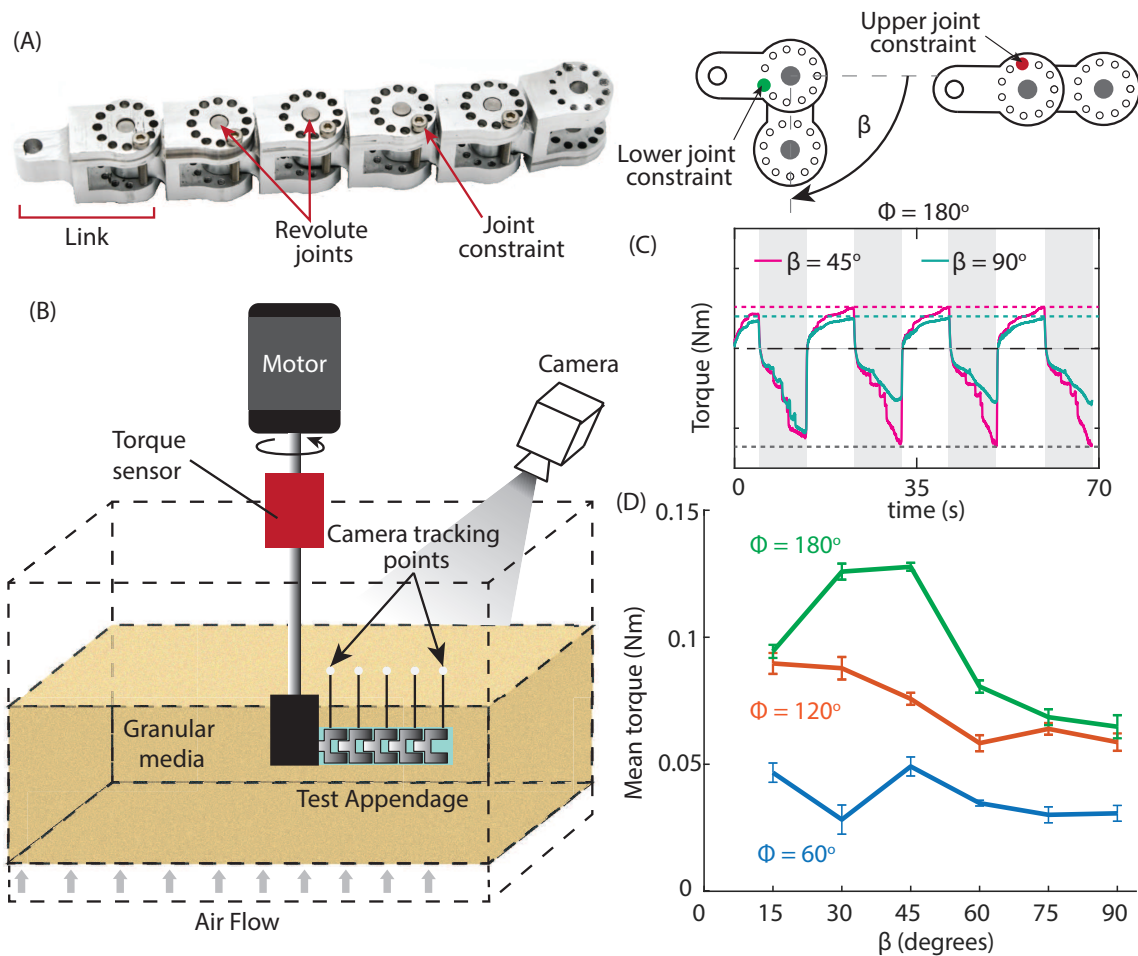
Figure 4.3: **Design and characterization of underactuated appendages.** (**A**) Photograph of the (Computerized Numerical Control) CNC machined linkage with five links and five joints with variable joint constraint angles at $15°$ increments enforced by pins inserted into one of 12 holes. The lower joint angle is denoted by β and the upper joint angle is fixed at $0°$. (**B**) Schematic of the experimental setup. ((**C**) The torque output for $\beta = 45°$ and $90°$ (mean of five trials) for amplitude of oscillation $\phi = 180°$. Asymmetry in torque was observed between power and return strokes because of the asymmetric joint constraints. ((**D**) Net mean torque (mean of five trials for last cycle, error bars show standard deviation) for the peak amplitude of $\phi = 60°, 120°,$ and $180°$ for different constraint angles β.

Appendage design for maximum forward thrust

We first measured the torque, τ, on an appendage undergoing an oscillatory motion to mimic the thrust and return strokes of our robot. We varied the angular amplitude of oscillatory motion ϕ in addition to the angular range β of the underactuated joints (Fig. 4.3B). We also
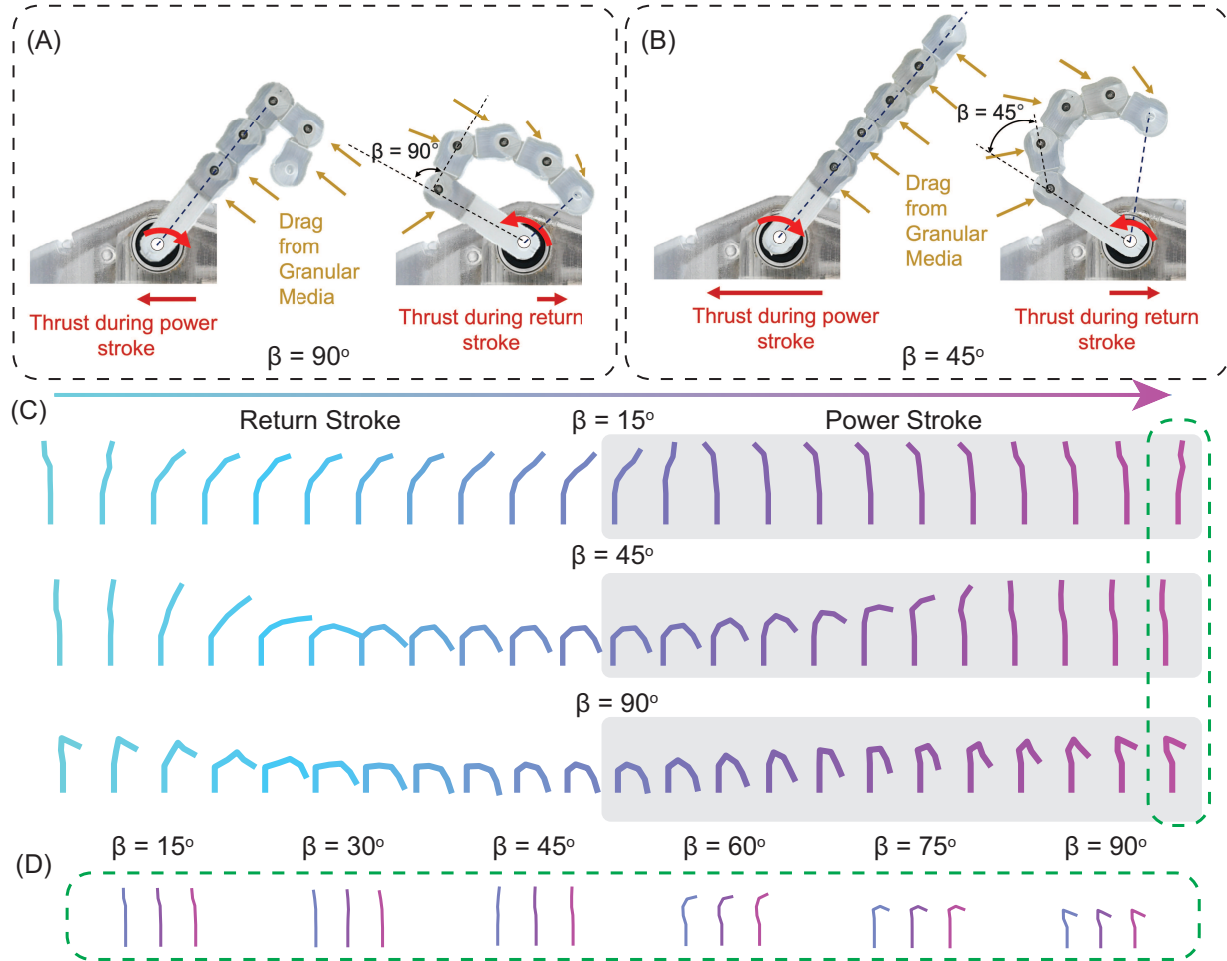
Figure 4.4: **Appendage curvature visualization.** (**A,B**) Schematics showing the effect of joint constraint angle $\beta = 90°$ and $\beta = 45°$ on the locomotion of the robot respectively. In the case of $\beta = 45°$, the appendage opened up to reach the maximum constraints during return stroke due to the drag of granular media; during the power stroke, the appendage pushed the grains to generate a net propulsive force for the robot to move forward. In the case of $\beta = 90°$, the appendage reaches maximum bent configuration in return stroke but during the power stroke, it was not able to fully straighten up which caused the links at the end to reach suboptimal configurations, reducing the net forward thrust. (**C**) Time-series images of the linkage configuration seen in its rotating frame, as measured from the LED markers used for optical tracking (mean of five trials) for one period of $\phi = 180°$ oscillation. (**D**) Tracked configurations of the linkage at the end of the power stroke for the last three cycles of oscillation for different constraint angles β, showing that once the linkage gets stuck in a bent configuration such as for $\beta = 90°$ it stays bent for multiple cycles.

measured the steady-state torque for the appendage in bent and straight configurations for different joint angles by rotating the appendage by two full rotations in both directions. It was observed that

for bent configuration (return stroke), torque decreased with the increase in the joint constraint angle β due to the decrease in drag (Fig. 4.8B).

Then we oscillated the appendage at a constant angular velocity, the reaction torque due to the drag of GM, τ, magnitude decreased during the power stroke because the links bent passively to stop at the upper joint constraint angle until the linkage became straight leading to maximum drag (Fig. 4.3C). The step decrease observed in the power stroke was likely due to each of the links reaching the upper constraint on the joint angle. During the return stroke, torque τ magnitude increased quickly because the linkage started to bend at the joint closest to the shaft followed by a slow increase to the maximum value when all the links had reached their upper constraint angles β. The torque τ in all these experiments was negative for power stroke and positive for the return stroke. We performed this experiment for β ranging from $15°$ to $90°$ in $15°$ intervals. The asymmetry in torque was measured as the net mean value of the torque τ in a cycle. This asymmetry is proportional to the net propulsive thrust required to move forward.

We observed that for low amplitudes of oscillation ($\phi = 60°$ and $120°$), the maximum torque of the power stroke (in the negative direction) didn't change much with the constraint angle β because all the links reached the straight maximum drag configuration (Fig. 4.8A). However, for a large amplitude of oscillation ($\phi = 180°$), we observed that this maximum torque decreased after the first cycle for $\beta > 45°$ (Fig. 4.3C). This behavior was unexpected since the steady-state torque during the return stroke decreased with the increase in constraint angle β. From the torque data, it was evident that there was an optimum joint angle β for maximum asymmetry in torque, at this large amplitude of oscillation. We measured the net mean torque in a cycle for different β values and found that there existed an optimum value of mean torque at $\beta = 45°$ for the amplitude of oscillation $\phi = 180°$. For the angle $\beta > 45°$, the mean torque started decreasing until reaching the lowest value at $\beta = 90°$ (Fig. 4.3D).

Suboptimal configurations leading to reduced performance

To understand the decrease in torque for $\beta > 45°$ at large amplitudes of oscillation, we calculated the joint positions at each time step from the tracking points using the data from the camera. We observed that for $\beta \leq 45°$ the linkage bent to reduce drag during the return stroke and reached the maximum drag configuration (straight) in the power stroke, as we anticipated (Fig. 4.4B). However, for $\beta > 45°$, the linkage didn't reach the maximum drag configuration in the power stroke and got stuck in that configuration (Fig. 4.4A). This behavior was prominent at higher joint angles (Fig. 4.4C). We observed that even if the linkage oscillated at an amplitude of $\phi = 360°$ the linkage remained stuck in the bent configuration because external drag forces acted on the links in a direction opposite to the direction of velocity forced the last links to remain stuck.

We calculated the shape of the linkage at the end of each power stroke for the last three cycles and observed that for $\beta \leq 45°$ the appendage was straight in the maximum drag configuration for all cycles (Fig. 4.4D). However, for $\beta > 45°$, the shape of the linkage at the end of the power stroke remained deformed in a bent configuration for all cycles. These results informed us that once the appendage is deformed in a suboptimal configuration such as for $\beta = 90°$, it will stay in that configuration for subsequent cycles too (Fig. 4.9). Thus, we concluded that we should choose an appendage with joint constraint angle $\beta = 45°$ as it was the optimum for large-amplitude sweeps.

4.2.3 Lift modulation

We tested the robot with the optimized appendages and found that the robot (designed with the wedge nose) surfaced slowly because of the high lift forces. To counteract this, we attached "terrafoils" (granular force control surfaces) to the side of the nose to control lift similar to how elevators in airplanes and diving planes in submarines are used to control pitch. The

goal of these surfaces was to counter the upward lift force acting on the body without increasing the resistive drag. We measured drag and lift forces acting on the terrafoils and optimized their geometry for minimum drag F_D and maximum downward lift force F_L (Fig. 4.5A, B). Firstly, we tested terrafoils at different aspect ratios at an angle $\theta = 15°$ from the horizontal but having the same frontal area of projection A. According to resistive force theory (RFT) for terradynamics, the drag F_D and lift F_D forces on an intruder is directly proportional to the projected frontal area of cross-section if the depth and the orientation remain the same [5]. However, we found that a unity aspect ratio experienced the least horizontal drag and maximum downward lift (Fig. 4.11).

Next, we tested the terrafoils at different angles θ to find the optimum terrafoil with the maximum negative F_L with the least F_D in GM. We observed that the horizontal drag (F_D) experienced by the body with terrafoils attached, first decreased and then increased with the angle θ as the projected area of cross-section increased (Fig. 4.5D). We believe that the drag force experienced by the body with terrafoils decreased because the terrafoils were added at the nose just in front of the widest cross-section of the body (where the gearbox fits; Fig. 4.2C) which may have caused the grains to flow before they interact with the body, reducing the net drag. This behavior cannot be predicted by RFT [5] but could be simulated using Discrete Element Method (DEM), which we leave for future work. Additionally, the net projected surface area of the terrafoils was much lesser than the area of the cross-section of the body, which may help explain why we didn't see much difference in the drag as compared to the body with no terrafoils. However, we noticed that the terrafoils changed the lift force significantly as we saw a clear trend where the lift forces F_L decreased with θ from 0° to 45°, and then increased with θ from 45° to 90°. The negative lift force in all these experiments indicated downward force acting on the robot. We also performed modeling for these trends using a modified version of a RFT (Modeling Methods) and found that the results matched very well with the experiments (Fig. 4.5C).

We demonstrated the application of terrafoils on the robot propelled by the asymmetric action of the appendages (Fig. 4.5E). We tracked the position of the robot using a tracker on a rod

sticking out of the GM. We observed that the robot had an upward y displacement of 3.41 mm

for 70 mm of horizontal displacement in 37 s (speed of 1.20 mm/s with fit with 95% confidence

bounds) (Fig. 4.5E). Then we added the 30° terrafoils on both sides of the robot and performed

the test again and found that the robot stayed oscillating around the 0 mm y displacement for

61.27 mm of x displacement in 37 s (speed of 1.03 mm/s with 95% confidence bounds). These

results showed how the granular lift force can be modulated by adding terrafoils to enable a robot

to swim horizontally in GM without surfacing.

Robot performance in the wild and lab

The robot was tested in the fluidized sand bed at a depth of 127 mm from the top. For

every test run the robot was placed horizontally using the fluidization and looking at the disk

marker attached to the carbon fiber tracking rod. We found that in lab experiments the robot

speed varied from 1.2 to 1.6 mm/s (Movie 1). These tests were performed both tethered for

maximum current and untethered on a fully charged battery and both showed similar performance

in a controlled granular bed.

We also tested the robot in a natural environment (at Scripps Beach, La Jolla, CA, US).

Since the robot was not designed to be able to self-burrow, we performed experiments by placing

the robot at a depth of 127 mm (observed through the carbon fiber marker) and distributing sand

over the top. We initiated the experiments with wireless control. We observed that the robot was

able to move forward in the natural sand for a distance of $\approx$ 30 mm at a speed of 0.57 mm/s. We

believe that the decrease in the speed of the robot relative to lab experiments in controlled glass

beads was due to several factors: 1) It has been shown previously that natural sand is harder to

dig in than dry glass beads [5], 2) the sand at the beach had a lot of seaweed (Movie 1) which

made the sand cohesive and may have reduced its ability to flow [113], and 3) the sand at the

beach had a higher moisture content than the glass bead used in the lab; after digging the hole for

the robot we observed that the sand at the depth of 127 mm was wet. Wet sand is harder to dig

in because of the lesser flow of grains requiring more motor torque and causing linkages to fail. We believe the performance of the robot can be improved by CNC machining the links for the appendage and the whole body out of aluminum.

4.3   Materials and Methods

4.3.1   Fluidized Granular Bed

In all the lab experiments we used an air fluidized bed of cross-section 43 by 43 cm which was filled with spherical glass beads of diameter $212 - 300 \ \mu$m (Potters Industries with density $\rho = 2.51$ g/cm^3) to a depth of 17.78 cm. The base of the testing platform was made of a porous plastic membrane with a pore size smaller than the grain diameter. The porous floor was supported by an aluminum honeycomb structure with an empty volume underneath to install the outflow of a commercial shop vacuum (6.5 Horse Power). The shop vacuum was connected to the ac power source through a proportional relay controlled by an analog output signal through a Data Acquisition Card (National Instruments). The flow rate for air going through the GM was controlled by varying the analog output voltage. The volume fraction ϕ was calculated by taking images of the bed height h and substituting other values in the equation $\phi = M/\rho A h$ where M, A, and h are the total mass of the grains, area of the bed, and height of the bed respectively [100]. Before every trial, airflow through the porous membrane fluidized the medium [14] and then we ramp down the flow rate slowly to get our desired packing fraction ϕ measured as 0.58 ± 0.03 which falls in the range of loosely packed sand found in natural environments [62].

4.3.2   Robot Design Materials

Considering the planetary gear motor's stall torque of approximately 1.13 Nm (116 rpm, Actobotics), a worm drive with a gear reduction of 15 : 1 was chosen, resulting in a net max

torque of 16.95 Nm which was more than enough to move the two appendages. The body and the gearbox were fabricated using a resin 3D printer (Objet 350 Connex 3, Stratasys Inc.; Material: Veroclear). This printer material was chosen for accuracy, strength, fast prototyping, being water and sand tight as well as easy removal of soluble support material. The drag experiments on the body informed the use of a tapered body. Inspired by previous studies of the sandfish lizard [17, 18], we designed the body with an asymmetrically tapering wedge-shaped nose, inclined at an angle of 30° to reduce the lift forces acting on the body.

The links for the robot appendages were also printed on the same 3D printer having the optimum joint constraint angle $\beta = 45°$. The untethered robot had a length of 25.6 cm, a width of 5.1 cm (widest part), and a height of 3.2 cm. To enclose the appendages from sand, we sewed a pouch using silicone-coated fabric (Ripstop Nylon, Seattle Fabrics) and a silicone adhesive (Silnet Seam Sealer, Gear Aid) was used to seal the seams. The optimum angular sweep of the robot appendages was selected to be $\approx 160°$ (90° + 70°) such that the appendages reach maximum angle while return stroke (parallel to the body) and can straighten near the farthest point of the body to generate maximum propulsive force.

4.3.3 Experimental Methods

Appendage characterization, experimental setup, and test appendage design

Controlled experiments were performed to investigate the phenomenon of the occurrence of sub-optimal bent configurations of a serial linkage during oscillatory motion in GM. In the experiment, we used a representative soft appendage, a serial linkage (made out of aluminum by using CNC machining) composed of five links and five revolute joints with variable joint constraint angles, which was actuated from one end through a shaft connected to a bipolar stepper motor (NEMA-23 with 15:1 gearbox) within a controlled fluidized granular bed (Fig. 4.10A). Each link was 30 mm long by 15 mm wide and 24 mm thick with variable joint constraint angles

to the precision of 15°. For all the experiments upper joint constraint angle was set to 0° such that the linkage cannot bend in the other direction and the lower joint constraint angle β (measured from the direction of the previous link) was varied. An optical encoder recorded the position and a reaction torque sensor(Futek) mounted between the motor shaft and the output shaft measured the reaction drag torque from the granular medium. The linkage was enclosed within a fabric cover (Ripstop Nylon, Seattle Fabrics) and five rigid wooden sticks were attached at each link.

A camera (Flir Point Grey) was rigidly mounted at the top to record the images of the linkage with 5 tracking points (LED lights on the wooden sticks) for each time step of the experiment. Post-processing of the images was done in MATLAB by binarizing each image and detecting the coordinates of LED lights in a plane parallel to the surface of the sand bed. Four periods of oscillations were performed at a constant angular velocity of 20 °/s at a constant depth of 5.08 cm for three peak to peak amplitudes ϕ of 60°, 120°, and 180° such that the angular position θ varies as $-\phi/2 \le \theta \le \phi/2$. The drag forces on the linkage were independent of speed, like other drag studies in the non-inertial regime [98, 99] (speed < 0.5 m/s).

For each experimental trial, airflow through the porous floor initially fluidized the medium, and then by slowly ramping down the airflow we got our desired packing fraction φ, which was determined through measurements of the total grain mass (M) and occupied volume (V) to be $\varphi = M/\rho V = 0.58 \pm 0.03$ which falls in the range of φ of loosely packed sand observed in desert sand dunes [62].

Terrafoil experimental setup

To investigate the effect of terrafoils, granular control surfaces, we performed systematic robophysical tests. In these tests, the fluidization bed was the same as the previous appendage characterization tests. The two terrafoils were attached to each side of the nose of a 3D printed body without the appendages. The body with attached to a 8 mm shaft which in turn was connected to a 6 axis force/torque sensor (Robotiq FT300-S) through a 3D printed mount. The

force sensor was rigidly attached to a stepper motor-driven linear stage with a lead screw. The Force sensor was set to record force and moments in six directions at a rate of 100 Hz. The linear stage was dragged through the sand at a constant velocity for a distance of 50.8 mm. We chose this distance because of the limitation of the bed size and we also found that the force values reach a steady-state in this distance. Five trials were done for each terrafoil shape and angle. We chose three different terrafoil geometries with the same surface area but different aspect ratio (L/w). The aspect ratio chosen were $3/4, 1$, and $4/3$. The respective lengths chosen were 15 mm, 17.32 mm, and 20 mm to be comparable to the size of the nose. For finding the optimum terrafoil angle, an aspect ratio of 1 was chosen. Before every trial, the sand bed was fluidized for 10 seconds to achieve a loose packing fraction for each trial. The linear stage, force sensor, and the fluidization bed were run through a Data Acquisition PCIe card (National Instruments) on a computer using Labview. All the tests were done at a depth of 50.8 mm, measured from the top surface of the robot body to the surface of the sand.

Body Design Experiments

Body design tests were done using the same experimental setup as the terrafoil tests. Each body for the test was 3D printed with a 2 mm thick shell and has the same projected cross-section area at the front. To compare how tapering and changing the length of the body at the back affects the drag force, we selected four different bodies in the sample space. The first body had the same cross-section throughout without any taper (shown in blue in Fig. 4.7), the second body is tapered (shown in green), the third body has the same taper as the second but has a length of $3/4$ times the length of the second body, and the fourth body has the same taper and same length as the second but has serrated edges. The serrated edges were made to test our hypothesis that anisotropic skin friction will significantly affect the drag results.

4.3.4 Modeling Methods

We used granular Resistive Force Theory, an empirical, reduced-order modeling approach to predict the intrusion forces on the robot moving horizontally in the sand with varying terrafoil angles (Fig. 4.12). Previous work by C. Li et al. [5] presented 2D-*Resistive Force Theory (RFT)*, an empirical approach that characterized the forces acting on a plate moving in granular media with variation in the direction of velocity and normal vectors. However, the empirical-modeling approach presented by C. Li et al., was only applicable for a plate whose velocity and normal vectors lie in the same vertical plane. Treers et al. further extended this empirical model to 3D scenarios based on penetrometery data presented for the 2D-Resistive Force Theory [114]. We used this adaptation of 2D-RFT for 3D scenarios to calculate the vertical and horizontal forces acting of the robot body intruding horizontally in the GM. We varied the terrafoil angles for the robot body between 0° to 90°, with a step of 15° and generate a triangulated mesh for each terrafoil angle of the robot body. The average length of the side for the triangles in the mesh was set to 5 mm (Fig. 4.12A). We used this mesh in a 3D-Resistive Force Theory formulation, implemented in Unity3D, to calculate the lift and drag forces acting on the robot body (Fig. 4.12B)(Equation 1-3). The horizontal and vertical forces acting on each triangle were calculated using the adaptation of 2D-RFT for 3D scenarios as presented by Treers et al. [114]. The forces acting on the robot body were the sum of all forces acting on every triangle in the mesh. The lift forces acting on a plate intruded horizontally in GM is negligible if (a) The normal of the plate is pointing vertically upwards or downwards (i.e., $\beta = 0°$); or (b) The normal of the plane is in the horizontal plane (i.e., $\beta = 90°$) (Fig. 4.12E). Hence, the terradynamic shape of the tip of the robot and the angle of the terrafoils majorly contributed to the downward lift generated by the robot as it intrudes horizontally in the GM (Fig. 4.12F).

$$F_x = |z|. \ A. \ \alpha_h(\beta, \gamma) \cdot \cos(\phi) \qquad (4.1)$$

$$F_y = |z|. \text{ A. } \alpha_v(\beta, \gamma) \tag{4.2}$$

$$F_y = |z|. \text{ A. } \alpha_h(\beta = 0, \gamma = 0) \tag{4.3}$$

4.4 Discussion

The objective of this study was to demonstrate the application of underactuated appendages with different bending curvatures, due to asymmetries from joint angle constrains, to generate thrust while interacting with the granular media. This underactuated appendage is controlled using a single motor connected to a worm drive which enables the design of the robot to be compact and lightweight as compared to previous approaches [15]. Previous work has demonstrated a compliant fin-based robot for locomotion in granular media, where the actuation parameters were optimized while the limb compliance was held constant [89]. The design strategy of generating asymmetric thrust presented in this work is very robust and versatile as compared to designing specifically for a particular granular material since the optimum joint angle constraints are independent of depth, the size and shape of the grains, and packing fraction of GM. This can also inform the understanding of how the geometry and compliance of animal appendages, such as turtles flippers [115, 111], generate a positive thrust in GM.

This work may offer insight into the design of other robots with underactuated linkages for locomotion in GM. For example, the locomotion of snake-like robots with passive elastic joints has been studied in viscous fluids [116]. However, in GM the nonzero yield stress presents the opportunity for robot links to become locked in sub-optimal configurations. Underactuation is likely an important design consideration for locomotion in GM since the torque requirements at joints can be very large. We found the optimum joint angle for the appendage considering a uniform curvature for simplicity i.e. all the links have the same joint constraint, however, it

is possible that the optimum constraint varies along the length of the appendage and each link has a different optimum. Future work could address these questions, taking a larger set of link geometry parameters using numerical methods such as the Discrete Element Method (DEM).

Our experimental results indicate that a smoothly tapered "terradynamic" body is better than having a body with a constant area of the cross-section with the same projected frontal area, which can be tested using numerical approaches (DEM) for future work. Although other research groups have shown the benefit of a tapered nose [117] and of adding a wedge shaped foil to reduce lift [90], our approach was to study the effect of the geometry of these modular control surfaces and to experimentally verify the reduction of lift forces without increasing horizontal drag by adding "terrafoils". According to Resistive force theory (RFT) [5], the terrafoils with a similar area and different aspect ratio should have the same drag and lift, which is different than what we found. These experimental results generate an understanding of how drag and lift forces can be changed by adding modular control surfaces for digging robots in the future. Future work can also explore making actuated terrafoils on the front and the back of the robot to control the pitch of the robot while swimming in the sand, similar to diving planes in submarines.

In general, our experimental study indicates that by measuring the differential grain resistance around a moving body, an obstacle above the body can be detected but not below the body. This result suggests how GM behaves completely different than fluids, where a symmetrical rigid rotating plate will have a symmetric flow of fluid above and below the plate. Future work could use the studies presented here to explore haptic identification and modeling of objects in granular media. To further show the benefit of having an appendage-based locomotion mechanism, we have shown how the appendages can be used to sense objects in the sand away from the body by sensing the granular flow, a strategy employed by many arthropods [107]. Future work can explore the detection of objects on either side of the robot by measuring the force difference between the two force sensors. Sensing can also be used to detect if the robot is trying to pitch upwards/rise towards the surface or pitch downwards/swim towards the bottom by measuring the

force from both the appendages as the drag force increases linearly with depth.

The experiments performed in this work led to the design of a two appendage-driven robot with symmetric actuation during the power and return strokes. This robot can be deployed in the wild because of its small form factor (can be easily held in a hand) and being fully untethered. This robot has the potential for steering by controlling the bend and locking angles on the appendages. The asymmetry in the forces between left and right appendages will cause the robot to steer. The terradynamic robot body made for this work was designed to be watertight and future work can explore testing in fully submerged granular media such as granular ocean surface, where the fully saturated grains behave similarly to dry granular media except with lesser particle-particle friction [6, 118]. We believe that we would see a similar performance for this robot in submerged sand as the slow movements of the appendages will likely not change the resistive forces from the GM. Further, along with swimming in grains, appendages can be used for swimming in the water by changing the robot body to have negative buoyancy elements so it does not sink and changing the actuation parameters for faster strokes. Future appendage-enabled robots can be designed to be deployed from the ocean surface to swim in the water, and transition from water to submerged sand to navigate the seabed.

Currently, there are some practical challenges to deploying the robot in the wild because it cannot perform self-burrowing from the surface. However, improvements can be made for self burrowing by either adding two more appendages such that there is each pair at the top and bottom of the body or by using actuated terrafoils to fluidize the sand in the front, or a combination of both to enable head-first transitions similar to wrasse fish [119] or belly-first transitions such as in sand vipers [120]. In the current body design, a single battery (450 mAh) charge can enable this robot to run for ≈ 5 minutes with a net distance traveled of ≈ 30 cm (assuming a speed of 1 mm/s at 127 mm depth). However, as our body shape experiments demonstrate there is only a small increase in body force as the robot body is elongated. Thus we envision future robots will have longer bodies for larger motors and batteries with multiple appendages.

Applications of this robot include deploying on extraterrestrial bodies with granular media such as the sandy surfaces of Mars [121, 122] and asteroids [123, 79]. This robot can be modified to deploy in submerged sand and can be used for sensing and monitoring the submerged sand bed in the ocean and for self-anchoring of ships. This robot also has applications in agriculture and soil studies where it can be used for contaminant monitoring of the soil. Another application for this robot can be measuring moisture content in grain silos as a moisture sensor can be easily integrated on the robot appendage and can also be used in search and rescue operations during grain entrapment in these silos.

Acknowledgment

Chapter 4, in part, is currently being prepared for submission for publication of the material. Chopra, Shivam; Drago Vasile; Jadhav, Saurabh; Tolley, Michael T.; Gravish, Nick. The dissertation author will be the primary investigator and author of this paper.
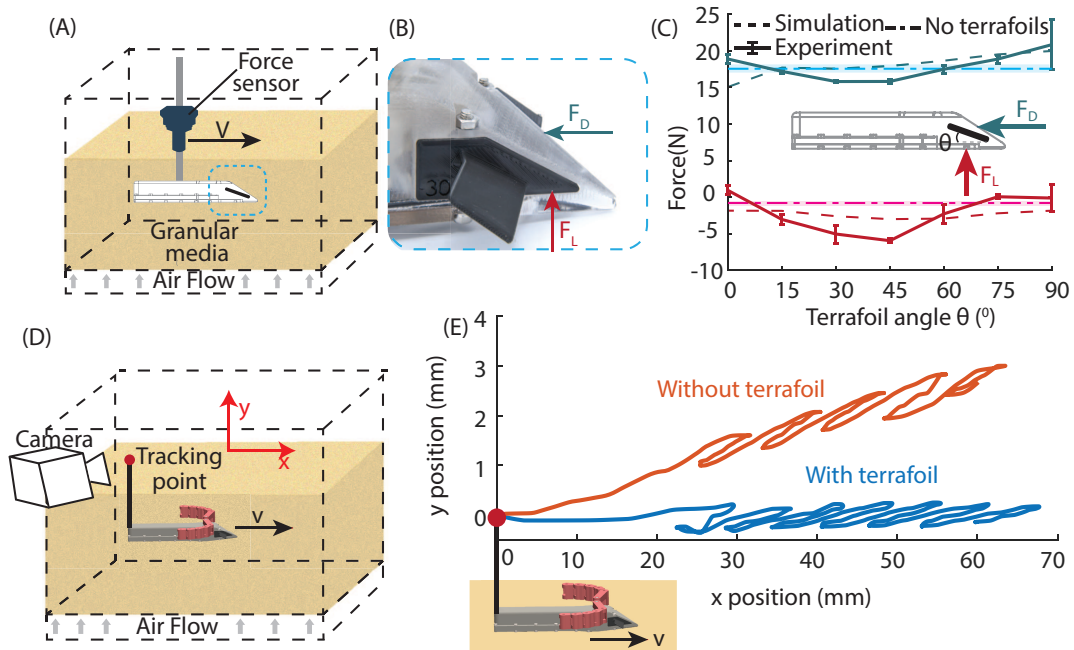
Figure 4.5: **Lift Modulation using terrafoils.** (**A**) Experimental setup for measuring drag and lift on the robot with terrafoils of different angles θ. (**B**) The nose of the robot with terrafoils attached to the side. (**C**) Experimental (solid lines) and simulation (dashed lines) results for drag and lift forces for terrafoils of different angles and aspect ratio = 1. The body drag and lift without terrafoils is shown in cyan and pink with the shaded region showing the error bar for the mean value of 5 different trials. The terrafoil with $\theta = 15°$ performed the best as it had the minimum drag and the maximum downward lift. (**D**) Schematic describing the free-swimming tests where the robot swims in the sand with a tracking marker with and without terrafoils (**E**) The trajectory of the robot measured by the position of the marker in x and y directions for the robot with and without terrafoils for $\theta = 30°$. y displacement stayed constant for the case when terrafoils were attached to the nose without much decrease in the speed in the x-direction. The first stroke is longer than others because we start the robot in power stroke with appendages fully extended (maximum drag)
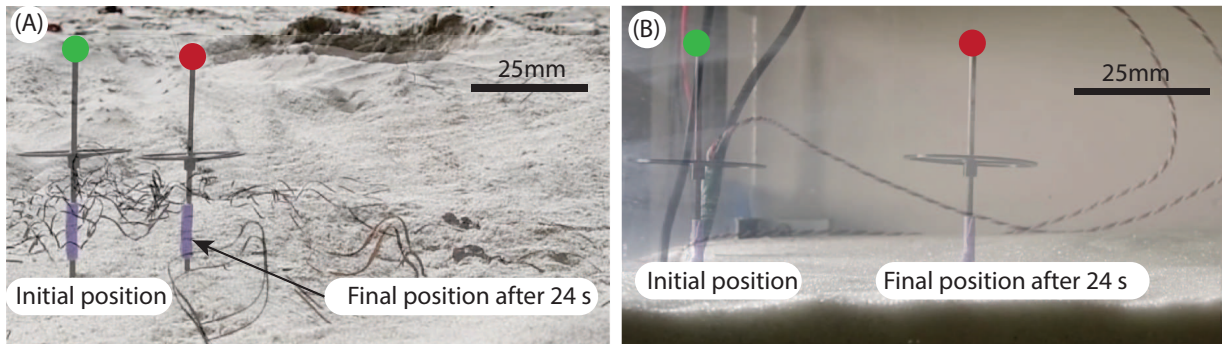
Figure 4.6: **Robot demonstration at the beach and the lab.** (**A**) Initial and final positions of the robot at the demonstration at the beach at a depth of 12.7 cm. The robot moved at a speed of 0.57 mm/s.(**B**) Initial and final positions of the robot moving in the controlled granular environment (glass beads) with a packing fraction of ≈ 0.58 (loosely packed) at the same depth with a speed of 1.2 mm/s
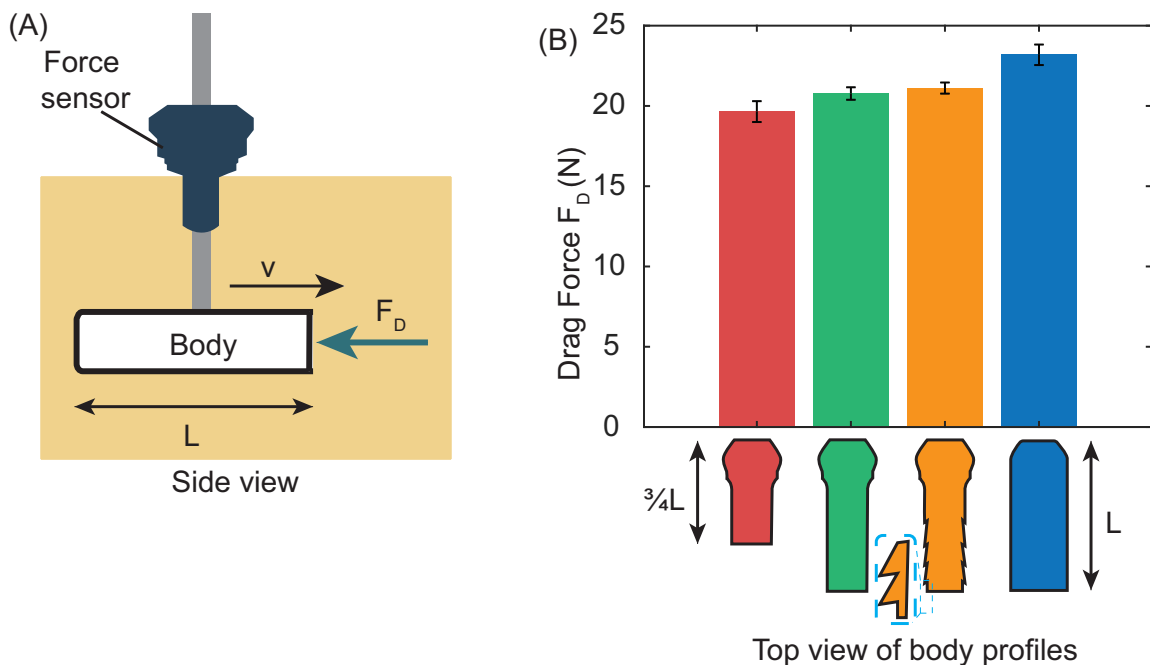
Figure 4.7: **Drag tests for selecting the most terradynamic body** (**A**) Schematic of the experimental setup used to measure drag on different body profiles. (**B**) Experimental results for drag force acting on the four different test bodies. The drag force depends on the length of the body and body profile
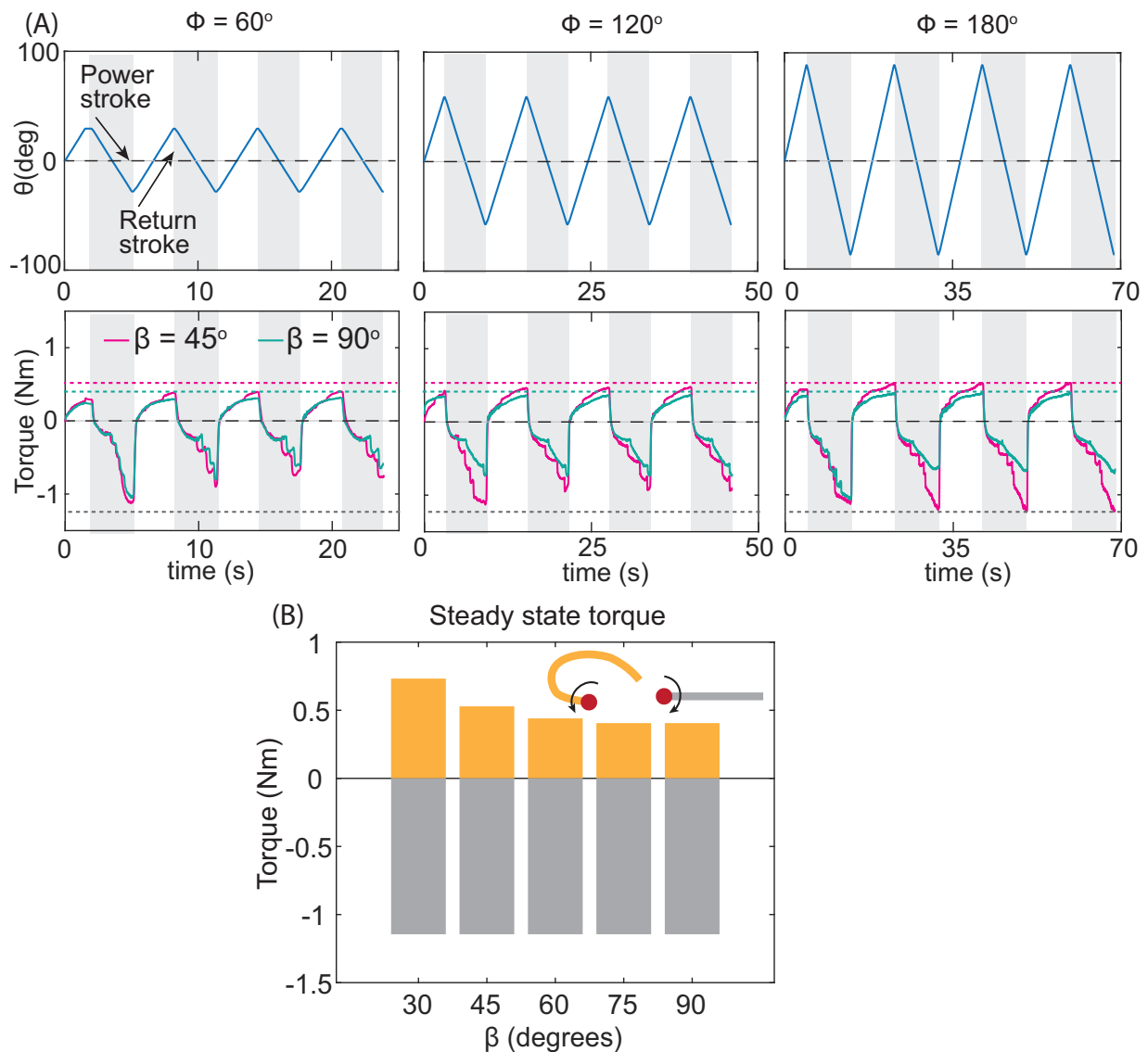
Figure 4.8: **Raw data for appendage characterization.** (**A**) Plot of position θ (input, top) and torque (output, bottom) vs time for three oscillation amplitudes $\phi = 60°$ (left), 120° (center), and 180° (right). The output torque was plotted for a lower joint angle of $\beta = 45°$ and 90° (mean of five trials). Asymmetry in torque was observed between power and return strokes because of the asymmetric joint constraints. (**B**) Bar plot showing that the steady-state torque (when the appendage was rotated for two full turns) in the return stroke (orange) decreased with an increase in β, and the steady-state torque in the power stroke (gray) was the same for all β for maximum drag configuration.
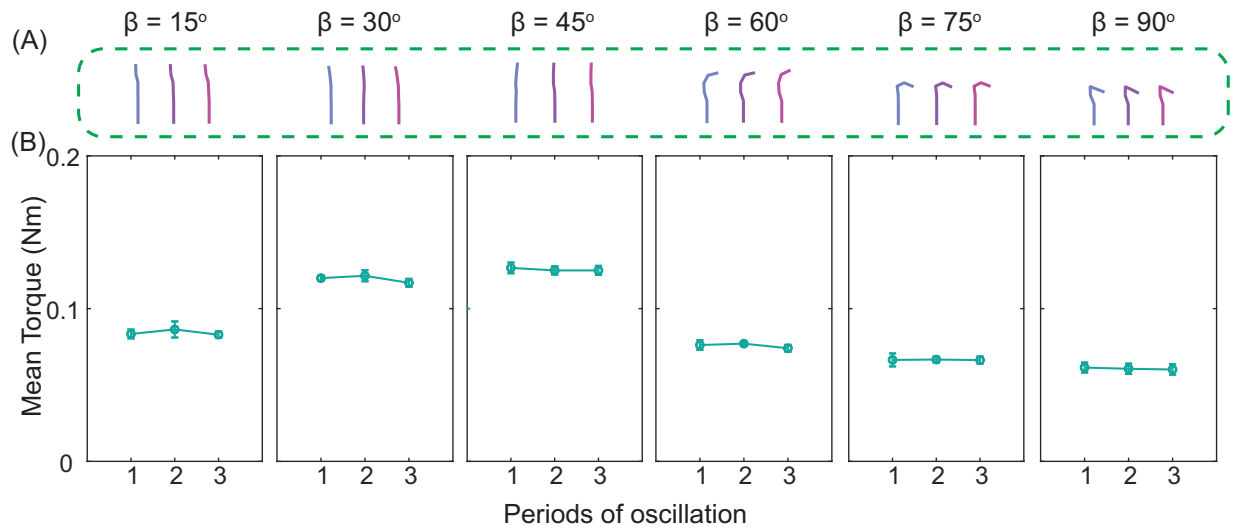
Figure 4.9: **Torque output for multiple trials for different β angles.** (**A**) Tracked configurations of the linkage at the end of the power stroke for the last three cycles of oscillation for different constraint angles β. (**B**) Net mean torque (mean of five trials, error bars show standard deviation) for the peak amplitude of $\phi = 180°$ for three cycles for different constraint angles.
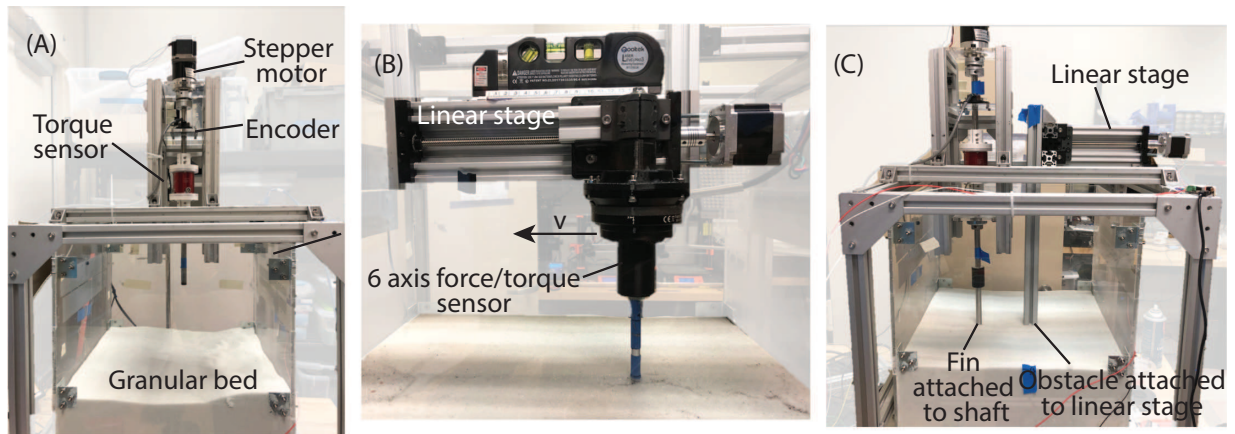
Figure 4.10: **Experimental setup pictures.** (**A,B** and **C** Photographs of the experimental setups for characterisation of the appendage, body and terrafoil drag tests, and sensing experiments respectively
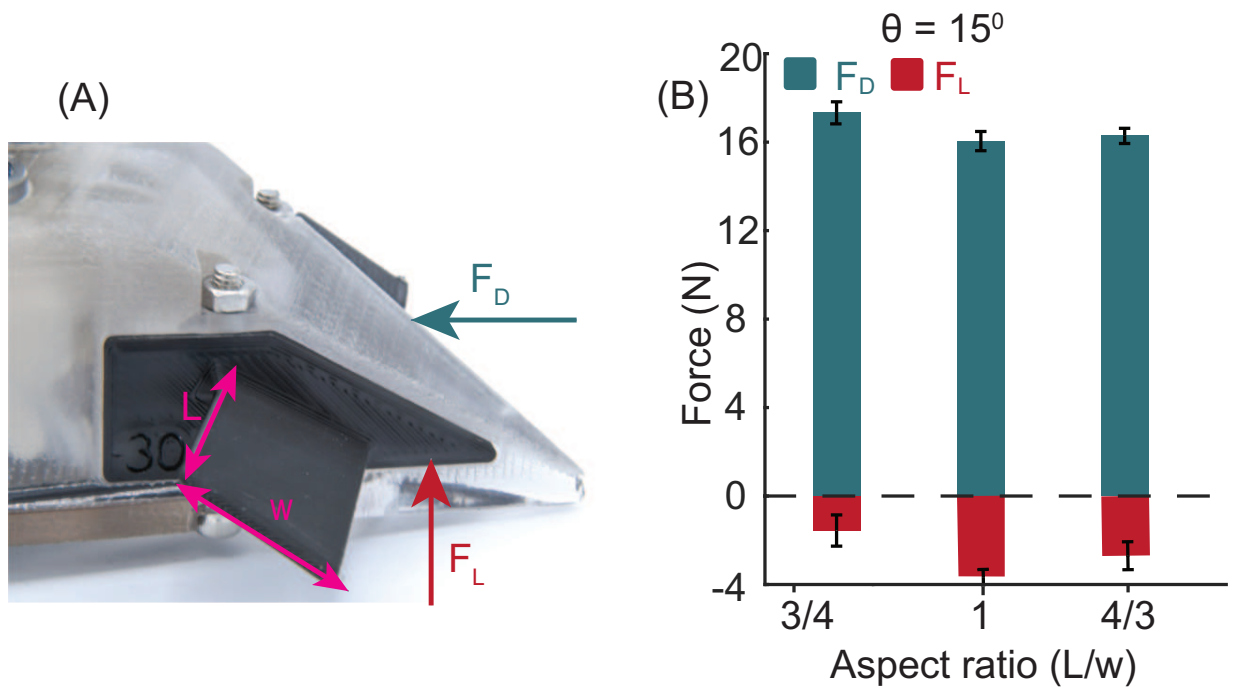
Figure 4.11: **Terrafoil aspect ratio results.** (**A**) Nose of the robot with terrafoils, (**B**) Drag F_D and lift F_L forces for terrafoils of three different aspect ratios and same projected area of cross-section. Terrafoil with the aspect ratio $= 1$ performed the best with minimum drag and maximum downward lift.
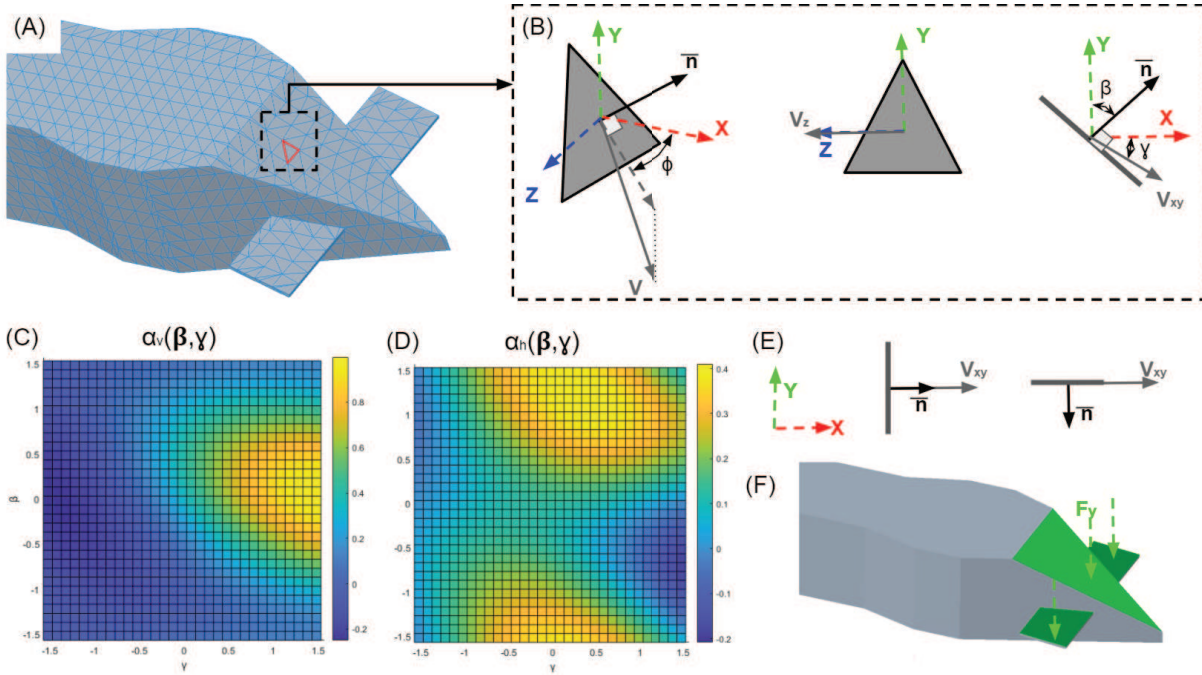
Figure 4.12: **Formulation of 3D-Resistive Force theory to calculate intrusion forces in granular media.** **(A)** A 3D mesh for the robot body with a mesh size of 5 mm is used to calculate the intrusion forces on the body. The intrusion forces on the body are equal to the sum of intrusion forces acting on each triangle in the mesh. **(B)** The intrusion forces acting on each triangle in the mesh is calculated by resolving the velocity vector for the triangle in orthogonal directions and using the empirical fit reported by Li et al. [5], to calculate the intrusion force in x,y, and z directions. **(C),(D)** report the empirical fits obtained for Li et al. [5] and adapted for 3D scenarios. (E) Scenarios where vertical forces acting on the plate are negligible. (F) The terradynamic shape of the tip of the robot and the angle of the terrafoils mainly contribute to the total lift generated by the robot

Chapter 5

Haptic detection of obstacles by measuring differential grain resistance in granular environments

Shivam Chopra, Drago Vasile, Saurabh Jadhav, Michael T. Tolley, Nick Gravish

Department of Mechanical and Aerospace Engineering, University of California San Diego, 9500 Gilman Dr., La Jolla, CA 92093

5.1   Introduction

One of the major problems for robot locomotion in granular media is the lack of sensing and navigation. Optical localization doesn't work in granular media (GM) as GM in nature comprises small, irregularly-shaped grains that have sides in many orientations that can reflect light in many directions. Therefore, the light that reflects off of the sides of sand grains does not travel in a single direction, and from different directions, no sensible image is produced. Some of the other materials within GM might absorb light too, further reducing the light passing

through. Acoustic localization has also not been successful in detecting small objects that are within the GM because of its damping characteristics [124] which can absorb the vibrations produced by an acoustic signal. Ground-penetrating radars (GNPs) have been successful in locating obstacles, particularly mines however the bulky machinery required hinders its success to be used on small-scale exploratory robots. Previous work has shown how tactile sensing can be used with machine learning to detect the shape of obstacles in grains by contact [125]. This method has produced promising results in rice grains but sensing using this method was challenging in the sand as it relied on contact with the obstacle with sand grains altering the detected shape. Further, as this strategy relies on contact with the obstacle, it is not efficient for robots to navigate around obstacles.

Locomotion through appendages presents a significant opportunity for sensing obstacles within the GM. Appendage locomotion may enable nearby obstacle sensing by detecting changes in the flow/force response of GM during locomotion. We propose that by measuring forces on appendages during locomotion we can detect nearby obstacles for navigation and avoidance. Our strategy was similar to haptic perception devices, using which we can recognize objects based on the force feedback, and similarly, we could measure the grain flow field around an obstacle to detect its presence. We hypothesized that we could detect obstacles in GM away from a moving body by measuring differential grain resistance by the appendages. Some aspects of this approach have been studied in previous work [126], showing how granular pressure fields vary around an obstacle surrounded by large plastic balls when the intruder (robot arm) touches the obstacle. However, the effect of obstacles in different orientations on the granular field around a rotating rigid plate has not been explored and systematic testing of real-time obstacle detection by a robot hasn't been performed.

In this work, we performed experiments to demonstrate the feasibility of sensing obstacles in granular media via measuring the differential force flow of the grains. We also perform these experiments for different orientations of the obstacle around a rotating fin to confirm the
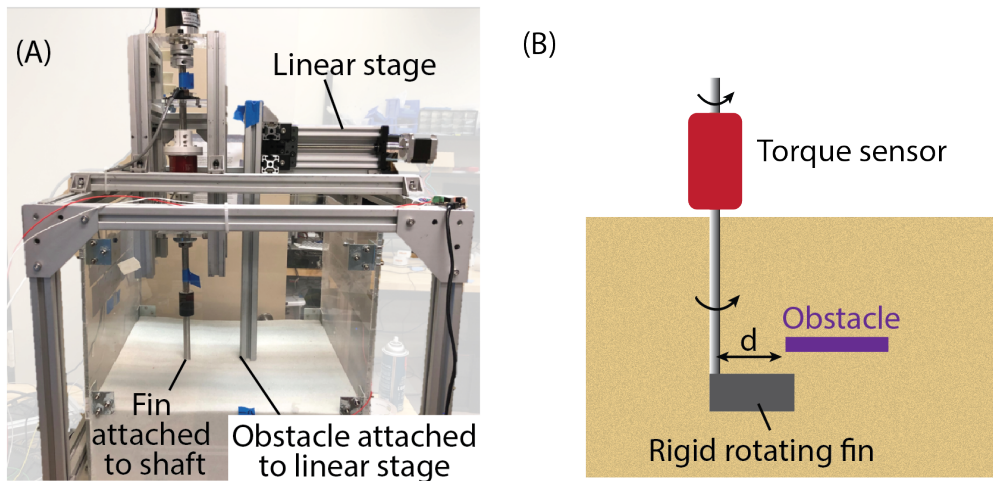
Figure 5.1: **Experimental setup to measure the differential grain resistance (A)** Picture of the experimental setup and **(B)** Schematic of the setup showing the fin and one of the orientations of the obstacle

applicability of this obstacle detection strategy for robot locomotion. To visualize the flow of grains around the obstacle, we performed particle image velocimetry (PIV). Finally, we demonstrate this obstacle detection strategy on a fully submerged robot from chapter 4.

5.2 Materials and Methods

In this section, I will describe the experiments we performed for understanding the effect on the granular field when a buried obstacle is present near a moving object.

5.2.1 Experiment for measuring differential granular flow around an obstacle

Firstly, we investigated the effect of this obstacle in different orientations on a moving rigid plate by setting up a benchtop experiment on a fluidized granular bed. The goal of these tests was to confirm how well we can detect obstacles by measuring differential grain flow. For

these experiments, we used the same fluidized granular bed and similar setup as the appendage characterization tests in Chapter 4 where a shaft was attached to a torque sensor through a high torque stepper motor. However, in this case, the appendage/fin used was made of 3D-printed ABS (76.2 mm long and 25.4 mm wide). We used an obstacle made of a 3.17 *mm* acrylic sheet (12.7 cm long and 10.2 cm wide) which was in turn attached through a rigid extrusion beam to a linear stage for moving it towards and away from the rotating fin. The fin was rotated for 270° and the obstacle was placed at 180° in global coordinates in all the experiments. We moved the obstacle using the linear stage away from the rotating fin in 0.5 cm increments from 0 *cm* to 14 cm from the axis of the rotating shaft to understand the range of sensitivity for this strategy.

We conducted five trials for the obstacle in five different orientations for each distance (Fig.5.3,5.2). We measured the torque output from the torque sensor for each oscillation of the shaft and automated the setup such that the granular bed fluidizes before each trial and the linear stage moves the obstacle by one increment away from the rotating fin.

5.2.2   Visualizing granular flow around an obstacle

GM is opaque and it's very challenging to visualize the flow of grains around an obstacle that is buried under the grains. We used particle image velocimetry (PIV) for granular materials as used in some previous work [100] to understand the flow of grains around different orientations of the obstacle when the fin is rotated near it. For these experiments, we attached the set up near the wall of the granular bed such that the oscillating fin just touches the wall of the granular bed. A digital single-lens reflex (DSLR) camera (Nikon D7500) was held on a tripod on the other side of the wall such that it can capture the fin along with any movement of the grains as shown in Fig.5.5A, B. We made sure that the camera was fixed at that location for all the trials and we attached obstacles at different orientations around the fin. We recorded videos of one oscillation for each orientation. Before each trial, the granular bed was fluidized to maintain the same packing fraction. To analyze the videos, we used an open-source function in Matlab

called *dftregistration* by *Manuel Guizar* which registers two images (2-D rigid translation) within a fraction of a pixel specified by the user. As this function works on the principle of image correlation, we made sure all the experiments were done so that the camera was rigidly fixed in one place. One trial was performed for each obstacle orientation in tight as well as loose state of granular media.

5.2.3   Obstacle detection using force sensor on robot appendage

For demonstrating that a robot can detect obstacles while moving in GM, we attached a cantilever load cell (Phidgets) to the last link of the appendage as shown in Fig. 5.6A. The load cell was attached to a force sensor amplifier (Futek IAA100) to filter the noise and amplify the signal. To confirm that the force sensor on the appendage can detect obstacles, we attached the appendage on the shaft such that it can oscillate in the granular bed similar to the previous setup. Using the same obstacle, we measured the force measured by the force sensor with and without the obstacle. The appendage oscillated for one full cycle under the obstacle as shown in fig.5.6D. The force data was recorded in Labview using a DAQ PCIe card on the computer and plotted in Matlab.

For robot demonstration in sensing, we attached a cantilever load cell to the last link of the right appendage which in turn was connected to an amplifier (Futek IAA100), and the signal was measured using a Labview through a DAQ card. The obstacle was kept the same as the robot was placed at a depth of 10.2 *cm* from the top and the obstacle was fixed such that the distance between the robot appendage and the obstacle is $\approx$ 15 mm. The robot was run tethered for this application to measure the forces.

5.3 Results

### 5.3.1 Detection dependent on obstacle orientation

We performed systematic benchtop experiments to understand how the presence of obstacles around an oscillating rigid plate affects the grain flow and thus the force exerted on a rigid rotating fin (we used a fin 3D printed out of Acrylonitrile Butadiene Styrene (ABS)). Firstly we moved the obstacle such that it's directly in front of the oscillating fin as shown in Fig.5.2. Interestingly we found that there was no torque difference when the obstacle is present in the front (Fig.5.2). Even when the obstacle had a larger surface area (wall), there was no effect on the torque. However, we observed that when the obstacle is placed such that it's above the rotating fin (Fig.5.3A) there was a peak in the torque (indicating the presence of obstacle) acting at the shaft attached to the fin. The peak reduced as we moved the obstacle away from the rotating fin and was very negligible at 6 cm away. An obstacle with a lesser cross-section area was also easily detected as shown in Fig.5.3C, but with lesser sensitivity. The obstacle below couldn't be detected using this method even when a flat plate was placed below the rotating fin Fig.5.3B.

We calculated the difference between the max torque when the obstacle was near and when it was far. We found that the torque difference value was remarkably high ($\approx 0.5Nm$) when the obstacle is a flat plate (Fig. 5.4) and very negligible when the obstacle was in the front or below the rotating fin.

5.3.2 Results from particle image velocimetry (PIV)

To understand why we couldn't detect any obstacles below the rotating fin we visualized the flow of grains. We took videos and analyzed them using image correlation. Since there was no effect of the wall on the rotating fin, we took these measurements near the transparent wall where we can see the flow of grains. We found that when no obstacle is placed around the rotating fin, the grains flow upwards when pushed by the fin which has also been shown in previous work
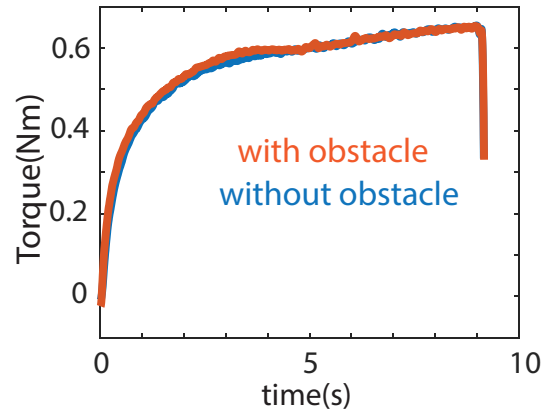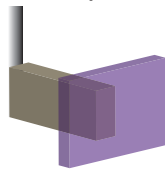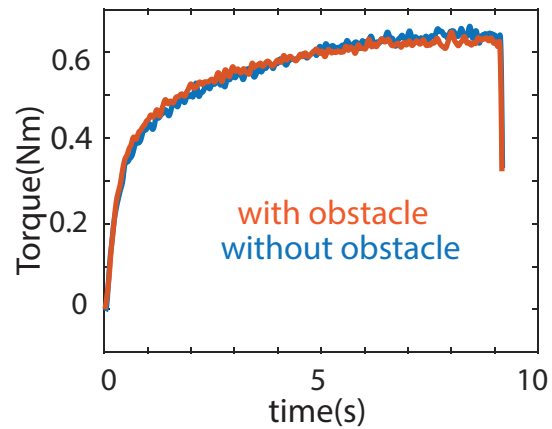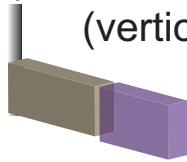
Figure 5.2: **Sensing results showing appendage cannot detect obstacles in front. (A) and (B)** Raw torque plots showing no effect of obstacle on the rotating fin when the obstacle is placed in front as shown in the schematics
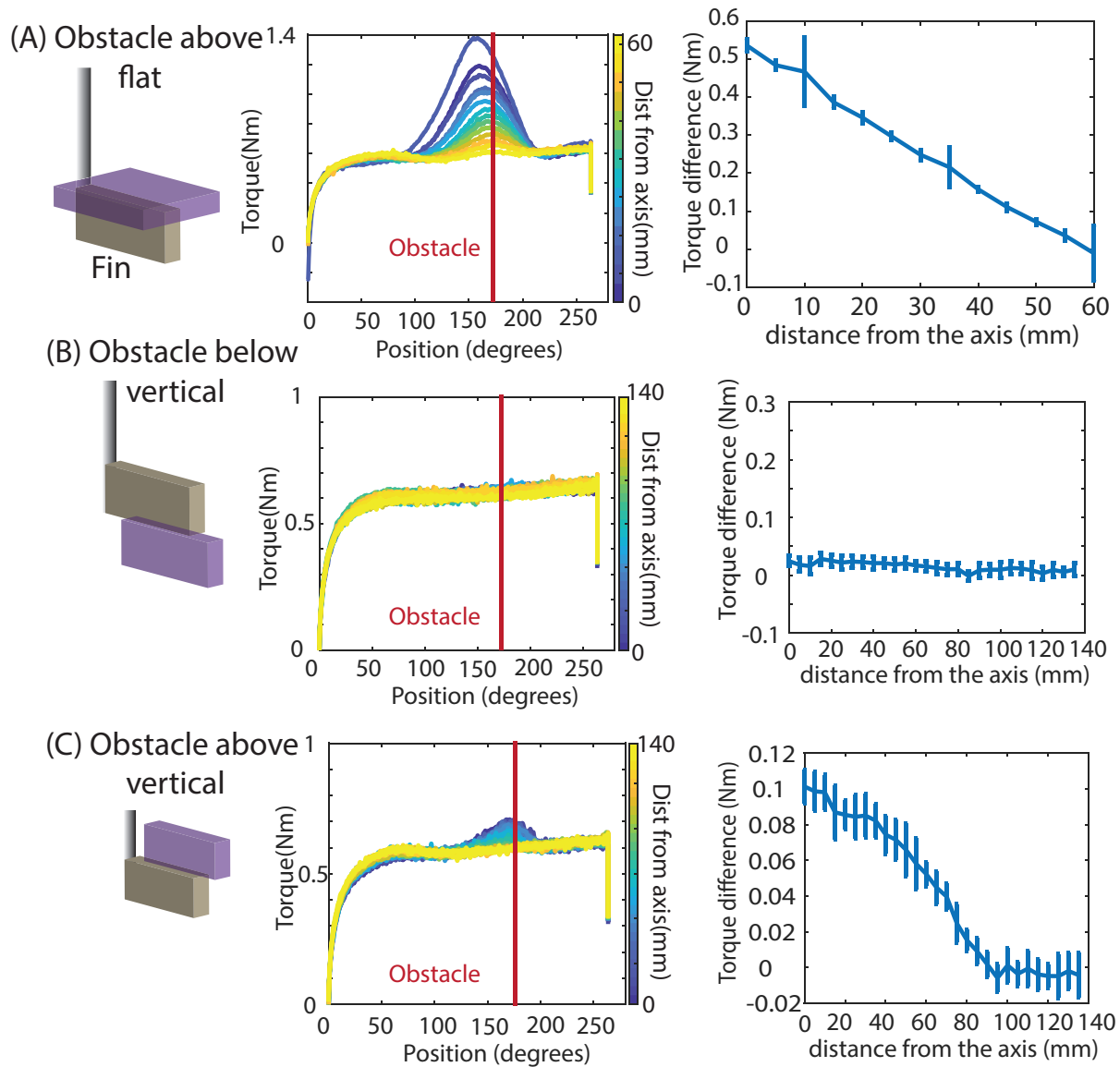
Figure 5.3: **Object detection with varying distance from the axis of rotation of the rigid fin.** **(A)**,**(B)**, and **(C)** (first column) The different orientations of the obstacle used for this test where a rigid fin was rotated from 0° to 270° with an obstacle at 180°. (second column) Raw data from 1 trial for 14 values of distance from the axis ranging from 0 mm to 60 mm. (third column) mean values of the max torque around the obstacle with the distance from the rotating plate. Error bars show the standard deviation for 10 trials.
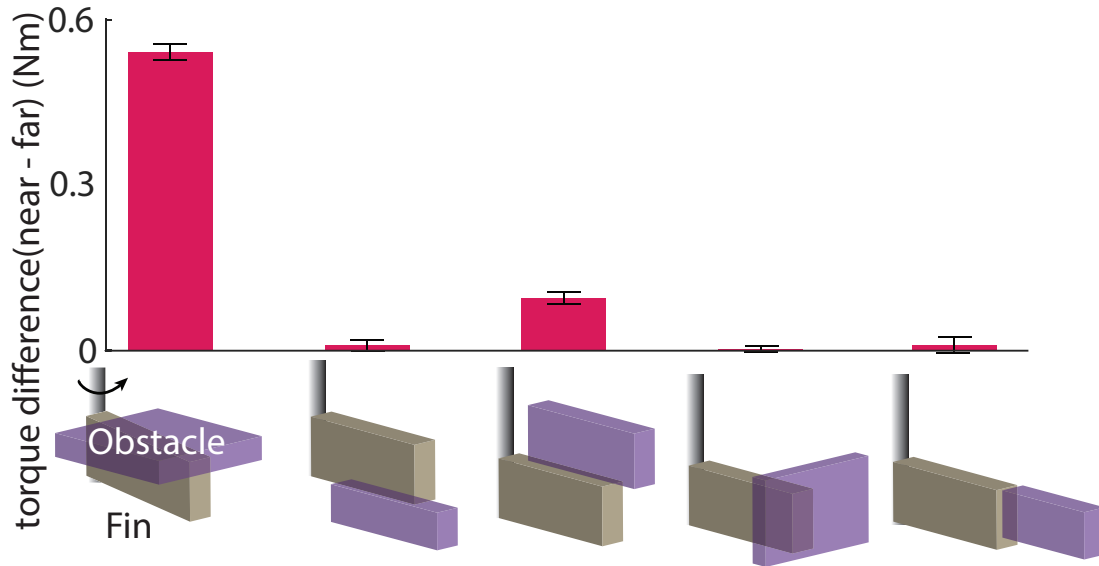
Figure 5.4: **Obstacle detection results for different orientations.** Difference of torque between the cases when the obstacle was far and when it was near for five different configurations. There is very less torque difference when the obstacle is below or in the front of the rotating fin and thus cannot be detected using this strategy. However, a significantly high torque difference was observed when the obstacle is above the rotating fin.

[20]. However, when an obstacle (flat plate) is placed over the rotating fin, we observed that the velocity vectors had a lesser magnitude going up (Fig.5.5C). They were hindered by the presence of the obstacle causing more torque at the base of the rotating fin as observed in our previous experiment. We could not measure any change in torque when an obstacle was below the rotating fin, as there was no change in the flow of grains as they tend to move up as shown in Fig.5.5C.

5.3.3 Confirmation of obstacle detection using an appendage

For a demonstration of sensing on the robot, we wanted to test this strategy using the appendages of the robot. By attaching a load cell on the last link of the appendage we were able to measure the force output for one oscillation when the appendage was rotated using the stepper motor Fig.5.6. We observed that the power stroke with an obstacle had a much higher output (Fig.5.6B). After calculating the mean for the whole cycle we found that the mean force with obstacle was significantly more than when no obstacle was present (Fig.5.6C).
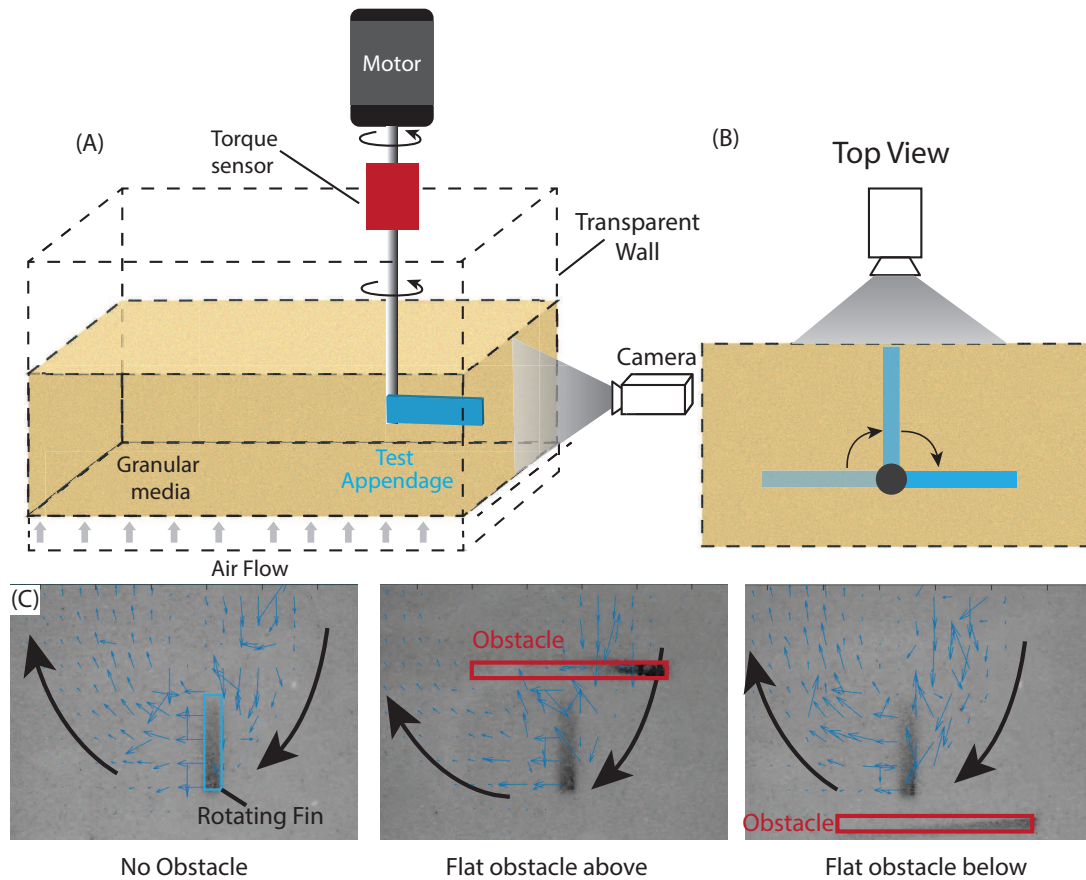
Figure 5.5: **Grain visualization using particle image velocimetry (PIV). (A)** Experimental setup to record videos for PIV. **(B)** Top view of the experimental setup showing half of the oscillation cycle with the test appendage just touching the transparent wall. **(C)** PIV snapshots were taken after analyzing the videos for no obstacle, flat obstacle above the fin, and obstacle below the fin. The blue arrows are the velocity vectors of each of the grid squares showing the flow of grains.
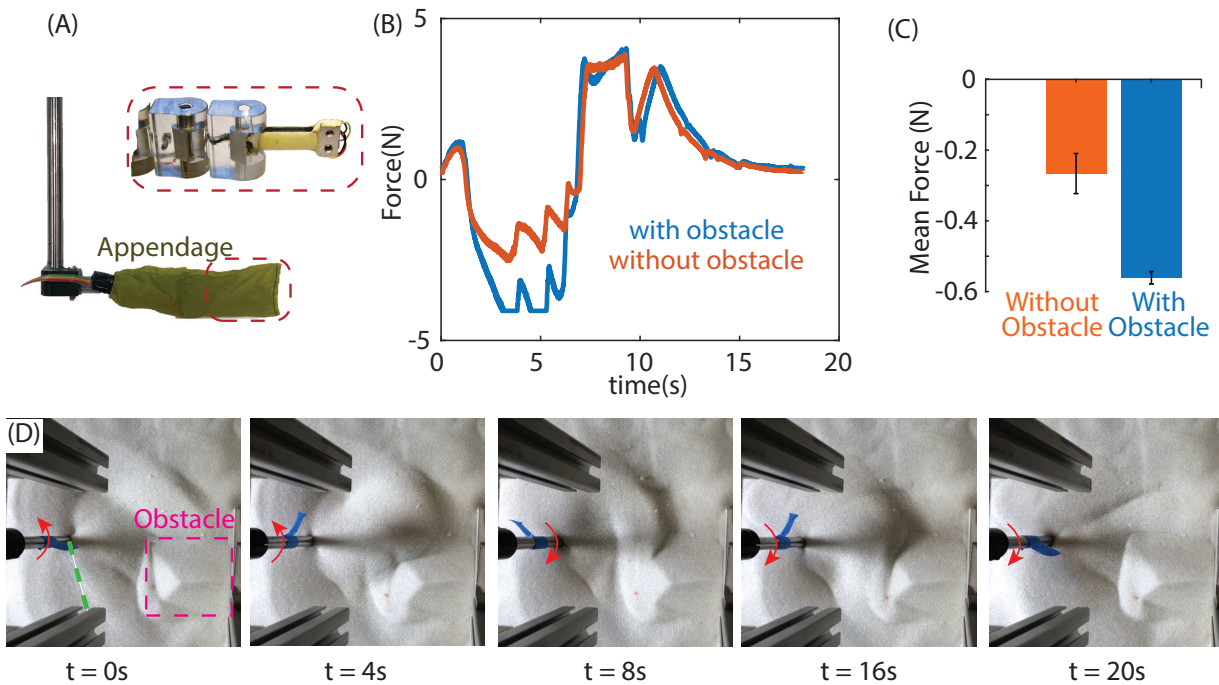
Figure 5.6: **Sensing experiments using the appendage** (**A**) Picture of the appendage attached to the shaft with the inset showing the force sensor attached as the last link. (**B**) Raw data output from the force sensor for one oscillation of the appendage without and with an obstacle ≈ 2 cm over it. (**C**) Mean force from 5 trials showing the force without obstacle is significantly lesser than when an obstacle was present. (**D**) Time series snapshots of the experiment showing full oscillation of the appendage under the obstacle

5.3.4   Obstacle detection using the robot

Our experiments indicated that a robot with oscillating appendages may be able to detect obstacles over it but not under it. It could also not detect obstacles parallel to the direction of motion (wall obstacle).

To demonstrate sensing on the robot we added a force sensor at the last link of one of the appendages (Fig. 5.7A). As the robot moved under the obstacle placed 10 mm above it (Fig. 5.7D), we measured the force sensor voltage through a data acquisition system (DAQ). We found that in one cycle of appendage motion, the force was positive during return stroke and some part of power stroke until the appendages opened up to exert force in the other direction (Fig. 5.7B). We found that the net mean force measured from the force sensor in the case of the robot moving under the obstacle was more than when there was no obstacle (Fig. 5.7C). This validated and demonstrated our results from systematic sensing experiments as we could detect the obstacle above the robot as it moved under it.

5.4   Discussion and Conclusion

Our experimental study indicates that by measuring the differential grain resistance around a moving body, an obstacle above the body can be detected but not below the body. We saw a considerable change in the torque when a vertical plate was above the fin. However, there was not an appreciable change in torque for the cases when the obstacle plate was in front of the fin and when the obstacle was below the fin. This result suggests how GM behaves completely different than fluids, where a symmetrical rigid rotating plate will have a symmetric flow of fluid above and below the plate. Future work could use the studies presented here to explore haptic identification and modeling of objects in granular media. To further show the benefit of having an appendage-based locomotion mechanism, we have shown how the appendages can be used to sense objects in the sand away from the body by sensing the granular flow, a strategy employed by
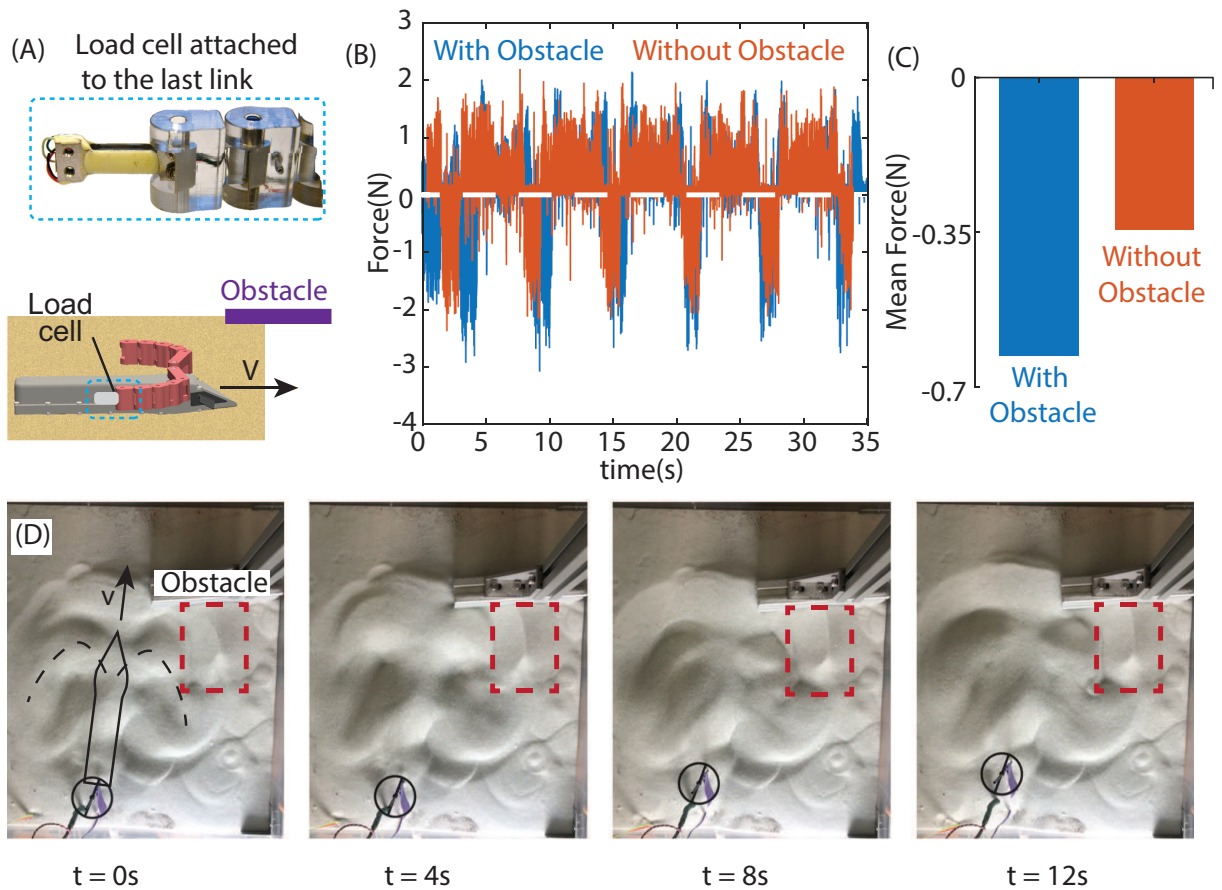
Figure 5.7: **Obstacle detection demonstration on the robot** (**A**) schematic of the robot moving under the obstacle with inset showing the location of the load cell. (**B**) Raw data from the force sensor for the two cases of with and without obstacle. (**C**) The mean of the force measured from the force sensor was more when the robot moved under an obstacle than when the robot moves without an obstacle. (**D**) Time series snapshots of the top view of the robot moving under the obstacle.

many arthropods [107]. We also demonstrated that by measuring the force difference between the two force sensors we can detect an obstacle on either side of the robot. Sensing can also be used to detect if the robot is trying to pitch upwards/rise towards the surface or pitch downwards/swim towards the bottom by measuring the force from both the appendages as the drag force increases linearly with depth.

Future work can explore the detection of objects below by fluidizing the sand below the appendage such that there is lesser resistance for the grains to flow. This method may improve the detection of objects that are below the rotating appendage. Even though a wall in the front didn't cause any torque difference in measurement, we hypothesize that a rotating fin with a different aspect ratio (wider and shorter) will lead to better detection. In all our experiments, the rotating fin had an aspect ratio such that the width is less than the length similar to the appendages in animals. These results highlight how animals might be using their appendages to detect which direction to go depending on the grain resistance.

Acknowledgment

the manuscript, M.T.T and N.G. advised on the designing the robot, conducting experiments, and writing the paper. **Competing interests** All authors declare that they have no competing interests.

Chapter 5, in part, is currently being prepared for submission for publication of the material. Chopra, Shivam; Drago Vasile; Jadhav, Saurabh; Tolley, Michael T.; Gravish, Nick. The dissertation author will be the primary investigator and author of this paper.

Chapter 6

Conclusion

In this work, I addressed the problems of robot locomotion and navigation in granular environments. I focused on the following major problems: a) granular media (GM) behaving as a solid and flowing as a liquid when an external force is applied more than its yield stress limit, causing robots moving on grains to sink and slip, placing high demands on foot placement and joint control, b) high depth-dependent resistive forces both in drag and lift along with non-zero yield stress that may cause unpredictable fluid/solid resistance when an intruder is moving within GM, causing robots to get stuck or/and move up to the surface after some time, and c) vision and acoustic localization methods for robot navigation are hindered by the granular material being opaque and extremely dampening, resulting in no obstacle detection for small scale exploratory robots.

In the second chapter, we proposed a foot design that can passively change shape and actively change stiffness for improved locomotion on granular media. It was shown that the foot in the soft (unjammed) state damped the vertical impact forces (least peak acceleration) and flattened up for an increased contact area and when jamming was initiated the foot turned rigid to become more capable of transmitting horizontal propulsion forces. We have shown that using the foot design with pleats such that it is soft before the drop and then rigid during shear led to reduced

foot deacceleration at the joints, lower pullout force, lower depth of penetration, and greater drag coefficient at a certain displacement of the foot. This improvement in locomotion parameters has shown how this designed foot will perform better than most of the rigid off-the-shelf robot feet. This design strategy can also be used to design shoes for locomotion on deformable grounds such as desert sand or snow. Future directions of this work can be miniaturizing the foot and attaching it to the legs of an off-the-shelf robotic platform for testing in a more natural environment like a desert. This project is an excellent example of taking inspiration from highly evolved animals to solve challenging problems.

Starting from the third chapter, I have focused on subterranean locomotion, and in this chapter, I took inspiration from appendage enabled digging in animals to investigate the use of soft appendages for generating asymmetric thrust. From these experiments, we learned that it is very challenging to have a single stiffness associated with an appendage as the resistive forces increase linearly with the depth. These experiments gave us an idea that although a very soft appendage might bend more it generates lesser asymmetric thrust which led us towards designing appendages based on joint constraints rather than stiffness which has been described in chapter 4. In the fourth chapter, we propose a novel method of locomotion in GM using underactuated appendages. The objective of this study was to demonstrate the application of underactuated appendages with different bending curvatures, due to asymmetries from joint angle constrains, to generate thrust while interacting with the granular media. This led to the development of an untethered appendage-enabled robot that was actuated by a single motor which is, by my knowledge, the first untethered digging robot to be tested in a natural environment. The design strategy of generating asymmetric thrust presented in this work is very robust and versatile as compared to designing specifically for a particular granular material since the optimum joint angle constraints are independent of depth, the size and shape of the grains, and packing fraction of GM. This study can also inform the understanding of how the geometry and compliance of animal appendages, such as turtle flippers [115, 111], generate a positive thrust in GM. This work

may offer insight into the design of other robots with underactuated linkages for locomotion in GM. For example, the locomotion of snake-like robots with passive elastic joints has been studied in viscous fluids [116]. Future work can be done in refining the design of appendages to generate more asymmetric thrust. This robot has applications in performing small-scale exploratory tasks in submerged or dry sand and even in extraterrestrial environments. Applications can also include moisture content monitoring in soil and grain bins, and search and rescue operations. This robot will also lead to new robot designs for appendage-enabled locomotion in granular media as this type of locomotion hasn't been researched well in these environments.

In the fifth chapter, we developed a new strategy for detecting obstacles in granular media by measuring the differential flow of grains around an obstacle. This strategy can be easily employed in small-scale exploratory robots with feedback control to detect obstacles and navigate around them. To my knowledge, this is the first sensing strategy that can be used for navigation in robots. We couldn't detect obstacles below the moving appendage with this strategy but adding fluidization under the moving appendage to force the grains to flow below the fin can lead to detection. Machine learning with more experimental data can be used to create a model for the localization of objects in a three-dimensional space.

Overall this thesis sheds light on how underactuation and passive compliance from bioinspired mechanisms can be used to improve and develop robotic systems for locomotion on and within granular environments. GM is abundantly found on Earth as well as many extraterrestrial planets but is a very challenging medium for robots to move within and sense obstacles. GM such as sand is a very heterogeneous medium with varying properties which requires controlled experiments for systematic tests such as the ones used in this work. A fluidized sand bed and robust setups were required for the experiments. Mechanical components get jammed even when a few grains get into the robot assembly requiring design considerations to effectively seal robots navigating granular environments. Underactuation is likely an important design consideration for locomotion in GM since the torque requirements at joints can be very

large. I also conclude that achieving "softness" using rigid materials is better than using soft materials such as silicone for experiments with sand, as in many initial experiments the soft sleeve failed after a few trials as demonstrated in Chapter 3. In conclusion, this thesis informs the readers about the design considerations they should have for testing and developing robots for navigating granular environments.

Appendix A

Granular simulation tank

Loosely packed sand responds very differently to shear than closely packed sand [61]. Thus, controlling the mechanical state of the GM is a top priority to have consistency between experimental trials and relate to the various Gm present in the natural environment. We simulated the granular natural environment that is composed primarily of fine particles with little cohesion [62]. Our tank consisted of a clear acrylic tank of a cross section of 43 by 43 cm . The top portion of the tank contained granular material. Spherical glass beads of diameter $212 - 300$ μm (Potters Industries with density $\rho = 2.51$ g/cm) were chosen as the model granular material as have been used by many granular physicists [5, 20, 127] and filled to a depth of ≈ 20 cm. A flow distributor, which is a porous, semi-permeable membrane with micro-sized holes to distribute air evenly, was sandwiched between the top and bottom chamber. Porous plastic plates (Porex Corporation, Fairburn, GA, USA) was used as the flow distributor in these experiments. The bottom chamber was airtight with connections for the compressed air blowers (shopvac 6.5 Horse Power, such that this air is distributed homogeneously by the porous membrane into the top chamber containing granular material and it exhausted out to the atmosphere from the top. The volume fraction of the granular medium was controlled by the fluidized bed in the following steps: 1) The compressed air flow opposite to the direction of gravity exerts buoyant forces on

the granular material. 2) As the air flow rate reaches a critical value, the grains become fluidized and start disrupted because of energy transport with the fluid and collisions between granular particles.3) Turning off the air flow slowly leads to the particles settling in a loosely packed state (volume fraction $\phi = 0.58 \pm 0.04$). 4) Using vibrations from the vibration motors attached, we were able to adjust the packing fraction. By varying the voltage of the proportional relay we were able to control the air flow through the granular material. The volume fraction ϕ of the granular media was determined from image-based measurements of the bed height by the equation $\phi = M/\rho A h$, where M, A and h are the the the the total mass of the grains, area of the bed, and height of the bed respectively [20].

Bibliography

[1] A. Martinez, J. Dejong, I. Akin, A. Aleali, C. Arson, J. Atkinson, P. Bandini, T. Baser, R. Borela, R. Boulanger, M. Burrall, Y. Chen, C. Collins, D. Cortes, S. Dai, T. Dejong, E. Del Dottore, K. Dorgan, R. Fragaszy, J. D. Frost, R. Full, M. Ghayoomi, D. I. Goldman, N. Gravish, I. L. Guzman, J. Hambleton, E. Hawkes, M. Helms, D. Hu, L. Huang, S. Huang, C. Hunt, D. Irschick, H. T. Lin, B. Lingwall, A. Marr, B. Mazzolai, B. Mcinroe, T. Murthy, K. O'hara, M. Porter, S. Sadek, M. Sanchez, C. Santamarina, L. Shao, J. Sharp, H. Stuart, H. H. Stutz, A. Summers, J. Tao, M. Tolley, L. Treers, K. Turnbull, R. Valdes, L. van PAassen, G. Viggiani, D. Wilson, W. Wu, X. Yu, and J. Zheng, "Bio-inspired geotechnical engineering: principles, current work, opportunities and challenges," *Géotechnique*, pp. 1–19, 2021.

[2] H. M. Jaeger and S. R. Nagel, "Physics of the granular state," *Science*, vol. 255, no. 5051, pp. 1523–1531, 1992.

[3] H. Katsuragi and D. J. Durian, "Unified force law for granular impact cratering," *Nature physics*, vol. 3, no. 6, pp. 420–423, 2007.

[4] Y. Takehara, S. Fujimoto, and K. Okumura, "High-velocity drag friction in dense granular media," *EPL (Europhysics Letters)*, vol. 92, no. 4, p. 44003, 2010.

[5] C. Li, T. Zhang, and D. I. Goldman, "A terradynamics of legged locomotion on granular media," *Science*, vol. 339, no. 6126, pp. 1408–1412, 2013.

[6] N. Mitarai and F. Nori, "Wet granular materials," *Advances in Physics*, vol. 55, pp. 1–45, jan 2006.

[7] G. McDowell and A. Humphreys, "Yielding of granular materials," *Granular Matter*, vol. 4, no. 1, pp. 1–8, 2002.

[8] J. Duran, *Sands, powders, and grains: an introduction to the physics of granular materials*. Springer Science & Business Media, 2012.

[9] R. M. Nedderman, *Statics and kinematics of granular materials*. Cambridge University Press, 2005.

[10] I. Albert, P. Tegzes, B. Kahng, R. Albert, J. G. Sample, M. Pfeifer, A.-L. Barabási, T. Vicsek, and P. Schiffer, "Jamming and Fluctuations in Granular Drag," *Physical Review Letters*, vol. 84, pp. 5122–5125, may 2000.

[11] F. Radjaï and F. Dubois, *Discrete-element modeling of granular materials*. Wiley-Iste, 2011.

[12] E. McKyes and O. Ali, "The cutting of soil by narrow blades," *Journal of Terramechanics*, vol. 14, no. 2, pp. 43–58, 1977.

[13] N. Guo and J. Zhao, "A coupled fem/dem approach for hierarchical multiscale modelling of granular media," *International Journal for Numerical Methods in Engineering*, vol. 99, no. 11, pp. 789–818, 2014.

[14] C. Li, P. B. Umbanhowar, H. Komsuoglu, D. E. Koditschek, and D. I. Goldman, "From the Cover: Sensitive dependence of the motion of a legged robot on granular media.," *Proceedings of the National Academy of Sciences of the United States of America*, vol. 106, pp. 3029–34, mar 2009.

[15] R. D. Maladen, Y. Ding, P. B. Umbanhowar, and D. I. Goldman, "Undulatory swimming in sand: experimental and simulation studies of a robotic sandfish," *The International Journal of Robotics Research*, vol. 30, no. 7, pp. 793–805.

[16] H. Marvi, C. Gong, N. Gravish, H. Astley, M. Travers, R. L. Hatton, J. R. Mendelson, H. Choset, D. L. Hu, and D. I. Goldman, "Sidewinding with minimal slip: snake and robot ascent of sandy slopes.," *Science (New York, N.Y.)*, vol. 346, pp. 224–9, oct 2014.

[17] R. D. Maladen, Y. Ding, P. B. Umbanhowar, A. Kamor, and D. I. Goldman, "Mechanical models of sandfish locomotion reveal principles of high performance subsurface sand-swimming," *J. R. Soc. Interface*, vol. 8, pp. 1332–1345, sep 2011.

[18] R. D. Maladen, Y. Ding, C. Li, and D. I. Goldman, "Undulatory swimming in sand: subsurface locomotion of the sandfish lizard.," *Science (New York, N.Y.)*, vol. 325, pp. 314–8, jul 2009.

[19] C. Li, P. B. Umbanhowar, H. Komsuoglu, and D. I. Goldman, "The effect of limb kinematics on the speed of a legged robot on granular media," in *Proceedings of the Society for Experimental Mechanics, Inc.*, vol. 67, pp. 1383–1393, Springer, apr 2010.

[20] N. Gravish, P. B. Umbanhowar, and D. I. Goldman, "Force and Flow Transition in Plowed Granular Media," *Physical Review Letters*, vol. 105, p. 128301, sep 2010.

[21] R. R. Murphy, S. Tadokoro, and A. Kleiner, "Disaster robotics," in *Springer Handbook of Robotics*, pp. 1577–1604, Springer, 2016.

[22] H. Omori, T. Nakamura, T. Yada, T. Murakami, H. Nagai, and T. Kubota, "Excavation mechanism for a planetary underground explorer robot," in *ISR 2010 (41st International Symposium on Robotics) and ROBOTIK 2010 (6th German Conference on Robotics)*, pp. 1–7, VDE, 2010.

[23] M. S. Verma, A. Ainla, D. Yang, D. Harburg, and G. M. Whitesides, "A soft tube-climbing robot," *Soft robotics*, vol. 5, no. 2, pp. 133–137, 2018.

[24] C. Christianson, C. Bayag, G. Li, S. Jadhav, A. Giri, C. Agba, T. Li, and M. T. Tolley, "Jellyfish-Inspired Soft Robot Driven by Fluid Electrode Dielectric Organic Robotic Actuators," *Frontiers in Robotics and AI*, vol. 6, nov 2019.

[25] C. Li, S. T. Hsieh, and D. I. Goldman, "Multi-functional foot use during running in the zebra-tailed lizard (Callisaurus draconoides).," *The Journal of experimental biology*, vol. 215, pp. 3293–308, sep 2012.

[26] N. M. Graf, A. M. Behr, and K. A. Daltorio, "Crab-Like Hexapod Feet for Amphibious Walking in Sand and Waves," in *Lecture Notes in Computer Science (including subseries Lecture Notes in Artificial Intelligence and Lecture Notes in Bioinformatics)*, vol. 11556 LNAI, pp. 158–170, Springer Verlag, jul 2019.

[27] A. G. Winter, V, R. L. H. Deits, D. S. Dorsch, A. H. Slocum, and A. E. Hosoi, "Razor clam to RoboClam: burrowing drag reduction mechanisms and their robotic adaptation," *Bioinspiration & Biomimetics*, vol. 9, p. 036009, apr 2014.

[28] M. Isava and A. G. Winter, "An experimental investigation of digging via localized fluidization, tested with Roboclam: A robot inspired by Atlantic razor clams," *Journal of Mechanical Design, Transactions of the ASME*, vol. 138, dec 2016.

[29] A. A. Calderon, J. C. Ugalde, J. C. Zagal, and N. O. Perez-Arancibia, "Design, fabrication and control of a multi-material-multi-actuator soft robot inspired by burrowing worms," in *2016 IEEE International Conference on Robotics and Biomimetics (ROBIO)*, pp. 31–38, IEEE, dec 2016.

[30] T. Nakamura, T. Kato, T. Iwanaga, and Y. Muranaka, "Development of a Peristaltic Crawling Robot Based on Earthworm Locomotion," *Journal of Robotics and Mechatronics*, vol. 18, pp. 299–304, jun 2006.

[31] D. Ortiz, N. Gravish, and M. T. Tolley, "Soft Robot Actuation Strategies for Locomotion in Granular Substrates," *IEEE Robotics and Automation Letters*, vol. 4, pp. 2630–2636, jul 2019.

[32] A. D. Horchler, A. Kandhari, K. A. Daltorio, K. C. Moses, J. C. Ryan, K. A. Stultz, E. N. Kanu, K. B. Andersen, J. A. Kershaw, R. J. Bachmann, H. J. Chiel, and R. D. Quinn, "Peristaltic locomotion of a modular mesh-based worm robot: precision, compliance, and friction," *Soft Robotics*, vol. 2, no. 4, pp. 135–145, 2015.

[33] B. Liu, Y. Ozkan-Aydin, D. I. Goldman, and F. L. Hammond, "Kirigami Skin Improves Soft Earthworm Robot Anchoring and Locomotion Under Cohesive Soil," in *2019 2nd IEEE International Conference on Soft Robotics (RoboSoft)*, pp. 828–833, IEEE, apr 2019.

[34] C. Laschi, B. Mazzolai, and M. Cianchetti, "Soft robotics: Technologies and systems pushing the boundaries of robot abilities," *Science robotics*, vol. 1, no. 1, p. eaah3690, 2016.

[35] C. Lee, M. Kim, Y. J. Kim, N. Hong, S. Ryu, H. J. Kim, and S. Kim, "Soft robot review," *International Journal of Control, Automation and Systems*, vol. 15, no. 1, pp. 3–15, 2017.

[36] M. Calisti, M. Giorelli, G. Levy, B. Mazzolai, B. Hochner, C. Laschi, and P. Dario, "An octopus-bioinspired solution to movement and manipulation for soft robots," *Bioinspiration & biomimetics*, vol. 6, no. 3, p. 036002, 2011.

[37] N. G. Cheng, M. B. Lobovsky, S. J. Keating, A. M. Setapen, K. I. Gero, A. E. Hosoi, and K. D. Iagnemma, "Design and analysis of a robust, low-cost, highly articulated manipulator enabled by jamming of granular media," in *2012 IEEE international conference on robotics and automation*, pp. 4328–4333, IEEE, 2012.

[38] M. Jiang, Z. Zhou, and N. Gravish, "Flexoskeleton Printing Enables Versatile Fabrication of Hybrid Soft and Rigid Robots," *Soft Robotics*, vol. 7, pp. 770–778, dec 2020.

[39] E. Brown, N. Rodenberg, J. Amend, A. Mozeika, E. Steltz, M. R. Zakin, H. Lipson, and H. M. Jaeger, "Universal robotic gripper based on the jamming of granular material," *Proceedings of the National Academy of Sciences*, vol. 107, pp. 18809–18814, nov 2010.

[40] Q. Yu, M. Jiang, and N. Gravish, "Flexoskeleton fingers: 3d printed reconfigurable ridges enabling multi-functional and low-cost underactuated grasping," *IEEE Robotics and Automation Letters*, vol. 6, no. 2, pp. 3971–3978, 2021.

[41] S. Seok, A. Wang, Meng Yee Chuah, D. Otten, J. Lang, and S. Kim, "Design principles for highly efficient quadrupeds and implementation on the MIT Cheetah robot," in *2013 IEEE International Conference on Robotics and Automation*, pp. 3307–3312, IEEE, may 2013.

[42] U. Saranli, M. Buehler, and D. E. Koditschek, "RHex: A Simple and Highly Mobile Hexapod Robot," *The International Journal of Robotics Research*, vol. 20, pp. 616–631, jul 2001.

[43] R. Schroer, M. Boggess, R. Bachmann, R. Quinn, and R. Ritzmann, "Comparing cockroach and Whegs robot body motions," in *IEEE International Conference on Robotics and Automation, 2004. Proceedings. ICRA '04. 2004*, pp. 3288–3293 Vol.4, IEEE, 2004.

[44] J. M. Anderson and N. K. Chhabra, "Maneuvering and Stability Performance of a Robotic Tuna," *Integrative and Comparative Biology*, vol. 42, pp. 118–126, feb 2002.

[45] C. Stefanini, S. Orofino, L. Manfredi, S. Mintchev, S. Marrazza, T. Assaf, L. Capantini, E. Sinibaldi, S. Grillner, P. Wallén, and P. Dario, "A novel autonomous, bioinspired swimming robot developed by neuroscientists and bioengineers," *Bioinspiration & Biomimetics*, vol. 7, p. 025001, jun 2012.

[46] K. Y. Ma, P. Chirarattananon, S. B. Fuller, and R. J. Wood, "Controlled flight of a biologically inspired, insect-scale robot.," *Science (New York, N.Y.)*, vol. 340, pp. 603–7, may 2013.

[47] G. Loianno, G. Cross, C. Qu, Y. Mulgaonkar, J. A. Hesch, and V. Kumar, "Flying Smartphones: Automated Flight Enabled by Consumer Electronics," *IEEE Robotics & Automation Magazine*, vol. 22, pp. 24–32, jun 2015.

[48] J. Kumagai, "Sand trap," *IEEE Spectrum*, vol. 41, pp. 44–50, jun 2004.

[49] T. Zhang, F. Qian, C. Li, P. Masarati, A. M. Hoover, P. Birkmeyer, A. Pullin, R. S. Fearing, and D. I. Goldman, "Ground fluidization promotes rapid running of a lightweight robot," *The International Journal of Robotics Research*, vol. 32, pp. 859–869, jun 2013.

[50] F. Qian, T. Zhang, W. Korff, P. B. Umbanhowar, R. J. Full, and D. I. Goldman, "Principles of appendage design in robots and animals determining terradynamic performance on flowable ground," *Bioinspir. Biomim.*, vol. 10, p. 056014, Oct. 2015.

[51] C. Li, S. T. Hsieh, and D. I. Goldman, "Multi-functional foot use during running in the zebra-tailed lizard (callisaurus draconoides)," *J. Exp. Biol.*, vol. 215, pp. 3293–3308, Sept. 2012.

[52] G. D. Canio, S. Stoyanov, J. C. Larsen, J. Hallam, A. Kovalev, T. Kleinteich, S. N. Gorb, and P. Manoonpong, "A robot leg with compliant tarsus and its neural control for efficient and adaptive locomotion on complex terrains," *Artificial Life and Robotics*, vol. 21, pp. 274–281, sep 2016.

[53] Hyun-jin Kang, K. Hashimoto, H. Kondo, K. Hattori, K. Nishikawa, Y. Hama, Hun-ok Lim, A. Takanishi, K. Suga, and K. Kato, "Realization of biped walking on uneven terrain by new foot mechanism capable of detecting ground surface," in *2010 IEEE International Conference on Robotics and Automation*, pp. 5167–5172, IEEE, may 2010.

[54] C. Piazza, C. Della Santina, G. M. Gasparri, M. G. Catalano, G. Grioli, M. Garabini, and A. Bicchi, "Toward an adaptive foot for natural walking," in *2016 IEEE-RAS 16th International Conference on Humanoid Robots (Humanoids)*, pp. 1204–1210, IEEE, nov 2016.

[55] D. Mura, C. D. Santina, C. Piazza, I. Frizza, C. Morandi, M. Garabini, G. Grioli, and M. G. Catalano, "Exploiting Adaptability in Soft Feet for Sensing Contact Forces," *IEEE Robotics and Automation Letters*, vol. 5, pp. 391–398, apr 2020.

[56] G. E. Weissengruber, G. F. Egger, J. R. Hutchinson, H. B. Groenewald, L. Elsässer, D. Famini, and G. Forstenpointner, "The structure of the cushions in the feet of African elephants (Loxodonta africana).," *Journal of anatomy*, vol. 209, pp. 781–92, dec 2006.

[57] S. Hauser, P. Eckert, A. Tuleu, and A. Ijspeert, "Friction and damping of a compliant foot based on granular jamming for legged robots," in *2016 6th IEEE International Conference on Biomedical Robotics and Biomechatronics (BioRob)*, pp. 1160–1165, IEEE, jun 2016.

[58] S. Hauser, M. Mutlu, F. Freundler, and A. Ijspeert, "Stiffness Variability in Jamming of Compliant Granules and a Case Study Application in Climbing Vertical Shafts," in *2018 IEEE International Conference on Robotics and Automation (ICRA)*, pp. 1559–1566, IEEE, may 2018.

[59] S. Hauser, M. Mutlu, P. Banzet, and A. Ijspeert, "Compliant universal grippers as adaptive feet in legged robots," *Advanced Robotics*, vol. 32, pp. 825–836, aug 2018.

[60] D. I. Goldman and P. Umbanhowar, "Scaling and dynamics of sphere and disk impact into granular media," *Physical Review E*, vol. 77, p. 021308, feb 2008.

[61] P. Umbanhowar and D. I. Goldman, "Granular impact and the critical packing state," *Physical Review E*, vol. 82, p. 010301, jul 2010.

[62] W. W. Dickinson and J. D. Ward, "Low depositional porosity in eolian sands and sandstones, Namib Desert," *Journal of Sedimentary Research A: Sedimentary Petrology & Processes*, vol. 64 A, no. 2, pp. 226–232, 1994.

[63] E. R. Trueman, "THE MECHANISM OF BURROWING OF THE MOLE CRAB, EMERITA," Tech. Rep. S3, 1970.

[64] T. Hesselberg and J. F. V. Vincent, "A comparative study of the functional morphology of parapodia and setae in nereids (Polychaeta: Nereididae)," Tech. Rep. 1, 2006.

[65] T. Hesselberg and J. F. Vincent, "The function of parapodial setae in a nereidid polychaete moving on two different substrata," *Journal of Experimental Marine Biology and Ecology*, vol. 335, pp. 235–244, aug 2006.

[66] K. M. Dorgan, C. J. Law, and G. W. Rouse, "Meandering worms: Mechanics of undulatory burrowing in muds," *Proceedings of the Royal Society B: Biological Sciences*, vol. 280, no. 1757, 2013.

[67] K. M. Dorgan, P. A. Jumars, B. Johnson, B. P. Boudreau, and E. Landis, "Burrow extension by crack propagation," *Nature*, vol. 433, p. 475, feb 2005.

[68] J. Gray, "STUDIES IN ANIMAL LOCOMOTION VIII. THE KINETICS OF LOCOMOTION OF NEREIS DIVERSICOLOR," tech. rep.

[69] J. M. ANDERSON, K. STREITLIEN, D. S. BARRETT, and M. S. TRIANTAFYLLOU, "Oscillating foils of high propulsive efficiency," *Journal of Fluid Mechanics*, vol. 360, pp. 41–72, apr 1998.

[70] J. Katz and D. Weihs, "Hydrodynamic propulsion by large amplitude oscillation of an airfoil with chordwise flexibility," *Journal of Fluid Mechanics*, vol. 88, pp. 485–497, oct 1978.

[71] K. N. Lucas, N. Johnson, W. T. Beaulieu, E. Cathcart, G. Tirrell, S. P. Colin, B. J. Gemmell, J. O. Dabiri, and J. H. Costello, "Bending rules for animal propulsion," *Nature Communications*, vol. 5, p. 3293, may 2014.

[72] M. N. J. Moore, "Torsional spring is the optimal flexibility arrangement for thrust production of a flapping wing," *Physics of Fluids*, vol. 27, p. 091701, sep 2015.

[73] N. Mazouchova, P. B. Umbanhowar, and D. I. Goldman, "Flipper-driven terrestrial locomotion of a sea turtle-inspired robot," *BIOINSPIRATION BIOMIMETICS Bioinspir. Biomim*, vol. 8, pp. 26007–26021, 2013.

[74] B. Kwak and J. Bae, "Design of hair-like appendages and comparative analysis on their coordination toward steady and efficient swimming," *Bioinspiration & Biomimetics*, vol. 12, p. 036014, may 2017.

[75] X. Jia, Z. Chen, A. Riedel, T. Si, W. R. Hamel, and M. Zhang, "Energy-Efficient Surface Propulsion Inspired by Whirligig Beetles," *IEEE Transactions on Robotics*, vol. 31, pp. 1432–1443, dec 2015.

[76] Z. Peng, Y. Ding, K. Pietrzyk, G. J. Elfring, and O. S. Pak, "Propulsion via flexible flapping in granular media," *Physical Review E*, vol. 96, p. 012907, jul 2017.

[77] Z. Peng, G. J. Elfring, and O. S. Pak, "Maximizing propulsive thrust of a driven filament at low Reynolds number via variable flexibility," *Soft matter*, vol. 13, pp. 2339–2347, mar 2017.

[78] M. K. Thompson and J. M. Thompson, *ANSYS mechanical APDL for finite element analysis*. Butterworth-Heinemann, 2017.

[79] H. Miyamoto, H. Yano, D. J. Scheeres, S. Abe, O. Barnouin-Jha, A. F. Cheng, H. Demura, R. W. Gaskell, N. Hirata, M. Ishiguro, T. Michikami, A. M. Nakamura, R. Nakamura, J. Saito, and S. Sasaki, "Regolith Migration and Sorting on Asteroid Itokawa," *Science*, vol. 316, pp. 1011–1014, may 2007.

[80] K. Isaka, K. Tsumura, T. Watanabe, W. Toyama, M. Sugesawa, Y. Yamada, H. Yoshida, and T. Nakamura, "Development of Underwater Drilling Robot Based on Earthworm Locomotion," *IEEE Access*, vol. 7, pp. 103127–103141, jul 2019.

[81] B. Liu, Y. Ozkan-Aydin, D. I. Goldman, and F. L. Hammond, "Kirigami Skin Improves Soft Earthworm Robot Anchoring and Locomotion Under Cohesive Soil," in *2019 2nd IEEE International Conference on Soft Robotics (RoboSoft)*, pp. 828–833, IEEE, apr 2019.

[82] A. G. V Winter, R. L. Deits, D. S. Dorsch, A. H. Slocum, and A. E. Hosoi, "Razor clam to RoboClam: Burrowing drag reduction mechanisms and their robotic adaptation," *Bioinspiration and Biomimetics*, vol. 9, no. 3, 2014.

[83] K. N. Nordstrom, D. S. Dorsch, W. Losert, and A. G. Winter, "A Microstructural View of Burrowing with RoboClam," tech. rep.

[84] A. Koller-Hodac, D. P. Germann, A. Gilgen, K. Dietrich, M. Hadorn, W. Schatz, and P. Eggenberger Hotz, "Actuated bivalve robot study of the burrowing locomotion in sediment," in *Proceedings - IEEE International Conference on Robotics and Automation*, pp. 1209–1214, 2010.

[85] A. Sadeghi, A. Tonazzini, L. Popova, and B. Mazzolai, "Robotic mechanism for soil penetration inspired by plant root," in *2013 IEEE International Conference on Robotics and Automation*, pp. 3457–3462, IEEE, may 2013.

[86] N. D. Naclerio, C. M. Hubicki, Y. O. Aydin, D. I. Goldman, and E. W. Hawkes, "Soft Robotic Burrowing Device with Tip-Extension and Granular Fluidization," in *IEEE International Conference on Intelligent Robots and Systems*, pp. 5918–5923, Institute of Electrical and Electronics Engineers Inc., dec 2018.

[87] A. Sadeghi, A. Mondini, and B. Mazzolai, "Toward Self-Growing Soft Robots Inspired by Plant Roots and Based on Additive Manufacturing Technologies," *Soft Robotics*, vol. 4, pp. 211–223, sep 2017.

[88] A. Thoesen, T. McBryan, and H. Marvi, "Helically-driven granular mobility and gravity-variant scaling relations," *RSC Advances*, vol. 9, no. 22, pp. 12572–12579, 2019.

[89] D. Li, S. Huang, Y. Tang, H. Marvi, J. Tao, and D. M. Aukes, "Compliant Fins for Locomotion in Granular Media," *IEEE Robotics and Automation Letters*, vol. 6, no. 3, pp. 5984–5991, 2021.

[90] N. D. Naclerio, A. Karsai, M. Murray-Cooper, Y. Ozkan-Aydin, E. Aydin, D. I. Goldman, and E. W. Hawkes, "Controlling subterranean forces enables a fast, steerable, burrowing soft robot," *Sci. Robot*, vol. 6, p. 2922, 2021.

[91] J. Tao, "Burrowing soft robots break new ground," *Science Robotics*, vol. 6, no. 55, pp. 1–3, 2021.

[92] N. T. Jafferis, E. F. Helbling, M. Karpelson, and R. J. Wood, "Untethered flight of an insect-sized flapping-wing microscale aerial vehicle," *Nature*, vol. 570, pp. 491–495, jun 2019.

[93] S. Kuindersma, R. Deits, M. Fallon, A. Valenzuela, H. Dai, F. Permenter, T. Koolen, P. Marion, and R. Tedrake, "Optimization-based locomotion planning, estimation, and control design for the atlas humanoid robot," *Autonomous Robots*, vol. 40, no. 3, pp. 429–455, 2016.

[94] G. Bledt, M. J. Powell, B. Katz, J. Di Carlo, P. M. Wensing, and S. Kim, "MIT Cheetah 3: Design and Control of a Robust, Dynamic Quadruped Robot," *IEEE International Conference on Intelligent Robots and Systems*, pp. 2245–2252, 2018.

[95] Y. Chen, H. Wang, E. F. Helbling, N. T. Jafferis, R. Zufferey, A. Ong, K. Ma, N. Gravish, P. Chirarattananon, M. Kovac, and R. J. Wood, "A biologically inspired, flapping-wing, hybrid aerial-aquatic microrobot," *Science Robotics*, vol. 2, p. eaao5619, oct 2017.

[96] R. A. Russell, "CRABOT: A Biomimetic Burrowing Robot Designed for Underground Chemical Source Location," *Advanced Robotics*, vol. 25, pp. 119–134, jan 2011.

[97] S. Chopra, S. Jadhav, M. Tolley, and N. Gravish, "Parapodia inspired soft appendages enable robot propulsion in granular media," *Bulletin of the American Physical Society*, 2021.

[98] D. Chehata, R. Zenit, and C. R. Wassgren, "Dense granular flow around an immersed cylinder," *Physics of Fluids*, vol. 15, pp. 1622–1631, may 2003.

[99] K. Wieghardt, "Experiments in Granular Flow," *Annual Review of Fluid Mechanics*, vol. 7, pp. 89–114, jan 1975.

[100] N. Gravish, P. B. Umbanhowar, and D. I. Goldman, "Force and flow at the onset of drag in plowed granular media," *Phys. Rev. E Stat. Nonlin. Soft Matter Phys.*, vol. 89, p. 42202, apr 2014.

[101] H. M. Jaeger, S. R. Nagel, and R. P. Behringer, "Granular solids, liquids, and gases," *Reviews of Modern Physics*, vol. 68, pp. 1259–1273, oct 1996.

[102] Y. Zhang, J. Cao, Q. Wang, P. Wang, Y. Zhu, and J. Zhang, "Motion Characteristics of the Appendages of Mole Crickets during Burrowing," *Journal of Bionic Engineering*, vol. 16, pp. 319–327, mar 2019.

[103] K. M. Dorgan, "The biomechanics of burrowing and boring," *J. Exp. Biol.*, vol. 218, pp. 176–183, jan 2015.

[104] A. Hosoi and D. I. Goldman, "Beneath Our Feet: Strategies for Locomotion in Granular Media," *Annual Review of Fluid Mechanics*, vol. 47, pp. 431–453, jan 2015.

[105] M. W. Hamrick, *Brian K. Hall (ed), Fins into Limbs: Evolution, Development, and Transformation*, vol. 14. 2007.

[106] G. Kuchling, "Nesting of Pseudemydura umbrina (Testudines : Chelidae): The Other Way Round," *Herpetologica*, vol. 49, no. 4, pp. 479–487, 1993.

[107] J. Jérˆ, J. Casas, and O. Dangles, "Physical Ecology of Fluid Flow Sensing in Arthropods," 2009.

[108] D. N. Espinoza and J. C. Santamarina, "Ant tunneling-A granular media perspective," *Granular Matter*, vol. 12, no. 6, pp. 607–616, 2010.

[109] R. Baines, S. Freeman, F. Fish, and R. Kramer-Bottiglio, "Variable stiffness morphing limb for amphibious legged robots inspired by chelonian environmental adaptations," *Bioinspiration and Biomimetics*, vol. 15, no. 2, 2020.

[110] M. J. Christianen, P. M. Herman, T. J. Bouma, L. P. Lamers, M. M. Van Katwijk, T. Van Der Heide, P. J. Mumby, B. R. Silliman, S. L. Engelhard, M. Van De Kerk, W. Kiswara, and J. Van De Koppel, "Habitat collapse due to overgrazing threatens turtle conservation in marine protected areas," *Proceedings of the Royal Society B: Biological Sciences*, vol. 281, no. 1777, 2014.

[111] J. A. Fujii, D. McLeish, A. J. Brooks, J. Gaskell, and K. S. Van Houtan, "Limb-use by foraging marine turtles, an evolutionary perspective," *PeerJ*, vol. 2018, no. 3, pp. 1–11, 2018.

[112] M. U. Rusli, D. T. Booth, and J. Joseph, "Synchronous activity lowers the energetic cost of nest escape for sea turtle hatchlings.," *The Journal of experimental biology*, vol. 219, pp. 1505–13, may 2016.

[113] J. Sigren, J. Figlus, and A. R. Armitage, "Coastal sand dunes and dune vegetation: Restoration, erosion, and storm protection Low-frequency wave dynamics in the nearshore during hurricane attack View project Coastal Ridge-Runnel Migration View project," *Shore Beach*, vol. 82, no. 4, pp. 5–12, 2014.

[114] L. K. Treers, C. Cao, and H. S. Stuart, "Granular resistive force theory implementation for three-dimensional trajectories," *IEEE Robotics and Automation Letters*, vol. 6, no. 2, pp. 1887–1894, 2021.

[115] N. Mazouchova, P. B. Umbanhowar, and D. I. Goldman, "Flipper-driven terrestrial locomotion of a sea turtle-inspired robot," *BIOINSPIRATION BIOMIMETICS Bioinspir. Biomim*, vol. 8, pp. 26007–26021, 2013.

[116] S. Ramasamy and R. L. Hatton, "Optimal gaits for drag-dominated swimmers with passive elastic joints," *Phys Rev E*, vol. 103, p. 032605, Mar. 2021.

[117] R. D. Maladen, P. B. Umbanhowar, Y. Ding, A. Masse, and D. I. Goldman, "Granular lift forces predict vertical motion of a sand-swimming robot," in *Proceedings - IEEE International Conference on Robotics and Automation*, pp. 1398–1403, 2011.

[118] Juha Koivisto, Marko Korhonen, Mikko Alava, C. P. Ortiz, D. J. Durian, and Antti Puisto, "Friction controls even submerged granular flows," *Soft Matter*, vol. 13, pp. 7657–7664, oct 2017.

[119] T.-A. M. Tatom-Naecker and M. W. Westneat, "Burrowing fishes: Kinematics, morphology and phylogeny of sand-diving wrasses (Labridae)," *Journal of Fish Biology*, vol. 93, pp. 860–873, nov 2018.

[120] B. A. Young and M. Morain, "Vertical burrowing in the saharan sand vipers (cerastes)," *Copeia*, vol. 2003, no. 1, pp. 131–137, 2003.

[121] T. Shinbrot, N.-H. Duong, L. Kwan, and M. M. Alvarez, "Dry granular flows can generate surface features resembling those seen in Martian gullies.," *Proceedings of the National Academy of Sciences of the United States of America*, vol. 101, pp. 8542–6, jun 2004.

[122] M. P. Almeida, E. J. R. Parteli, J. S. Andrade, and H. J. Herrmann, "Giant saltation on Mars.," *Proceedings of the National Academy of Sciences of the United States of America*, vol. 105, pp. 6222–6, apr 2008.

[123] E. Asphaug, "PLANETARY SCIENCE: The Shifting Sands of Asteroids," *Science*, vol. 316, pp. 993–994, may 2007.

[124] F. Pacheco-Vázquez and S. Dorbolo, "Rebound of a confined granular material: combination of a bouncing ball and a granular damper," *Scientific reports*, vol. 3, no. 1, pp. 1–7, 2013.

[125] R. Patel, R. Ouyang, B. Romero, and E. Adelson, "Digger Finger: GelSight Tactile Sensor for Object Identification Inside Granular Media," *Springer Proceedings in Advanced Robotics*, vol. 19, no. Figure 1, pp. 105–115, 2021.

[126] S. Jia and V. J. Santos, "Multimodal haptic perception within granular media via recurrent neural networks," in *Proceedings of the RSS Workshop Tactile Sensing for Manipulation: Hardware, Modeling, and Learning, Boston, MA, USA*, vol. 15, 2017.

[127] Y. Ding, N. Gravish, and D. I. Goldman, "Drag induced lift in granular media," *Phys. Rev. Lett.*, vol. 106, p. 28001, jan 2011.